AIR FORCE ACADEMY

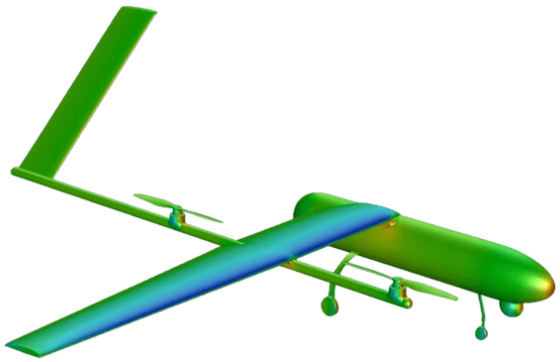

Aerodynamic Detailed Design of an Unmanned Aerial Vehicle with VTOL Capabilities

Vasco Luís Martins Ferreira Coelho

ALF/ENGAER 139424-L

Thesis to obtain the Master of Science Degree in

Military and Aeronautical Sciences - Aeronautical Engineering

Examination Committee

Chairperson:	BGEN/EngEl 119923-E Rui Fernando da Costa Ferreira
Supervisor:	MAJ/EngAer 131603-G Joao Vítor Aguiar Vieira Caetano
	Dr. Frederico José Prata Rente Reis Afonso
Member of the Committee:	Prof. Dr. Afzal Suleman

Sintra, December 2021

”Research is what I’m doing when I don’t know what I’m doing”

Wernher von Braun

Acknowledgments

First of all, I have to express my sincere gratitude to Dr. Frederico Afonso for joining this project and for all the technical guidance, patience, and readiness shown, and to MAJ João Caetano for the critical and constructive spirit transmitted which made me overcome the adversities encountered throughout the period it took me to complete this dissertation.

I would like to recognize the remaining coordinators of the project, Dr. André Marta and MAJ Luís Félix for the contributions and inputs given at the early design stages which guided the project in the right direction. In this area, I also thank MAJ Tiago Oliveira and SAJ Paulo Mendes for the help given when required.

To my comrades and friends Bernardo Alves, Pedro Silva and Paulo Sá, six years ago we started this journey together and we now end it together. The course and this final project could not be done without the friendship, mutual help and cooperation shown by all of you. The effort and dedication put into the conceptual phase of this project greatly eased my work in this dissertation, and for that, I can not thank you enough. Furthermore, I have to mention my second family - Distintos - for the fabulous experiences we have had during the past years.

Finally, I would like to dedicate this work to my parents, brother and Marta. Their understanding and support during my academic journey helped me to complete this milestone of my life.

Resumo

Esta tese está integrada num projeto de desenvolvimento de um veículo aéreo não tripulado capaz de efetuar descolagem e aterragem vertical, e tendo hidrogénio como principal fonte de energia utilizando para tal uma célula de combustível. A dissertação foca-se nas fases de desenvolvimento preliminar e detalhada no que diz respeito a estudos aerodinâmicos e desempenho em voo.

A fase preliminar abrange a conceção da asa e da cauda, recorrendo ao software XFLR5, em conjunto com uma estimativa da resistência aerodinâmica total da aeronave, recorrendo a expressões semi-empíricas.

Para a análise detalhada, foi utilizado o software de mecânica de fluidos computacional Fluent. A escolha do modelo de turbulência SST, em conjunto com o modelo de transição $\gamma - Re_\theta$, é validada pelas simulação 2D do perfil SG6042, apresentando resultados consistentes com os dados experimentais. A polar aerodinâmica da asa é obtida através da simulações 3D da mesma para vários ângulos de ataque. Por forma a melhorar as propriedades aerodinâmicas da asa, foi aplicada torção à ponta da asa, movendo a região inicial da perda da ponta da asa para a raiz. O impacto do sistema de propulsão vertical na resistência aerodinâmica em voo cruzeiro é avaliado através da realização de testes em túnel de vento e simulações em Fluent. Simulações de toda a aeronave concluem que, dependendo do alinhamento dos rotores, a resistência aerodinâmica da aeronave varia entre 16.32 e 19.22 N para voo cruzeiro, resultando num tempo total de voo entre 3H05 e 3H25.

Palavras-chave: Aerodinâmica, Célula de Combustível, Descolagem e Aterragem Vertical, Hidrogénio, Mecânica de Fluidos Computacional, Veículo Aéreo Não Tripulado.

Abstract

This thesis is part of a project to design an unmanned aerial vehicle capable of performing vertical take-off and landing, and having hydrogen as its main energy source by using a fuel cell. The present dissertation is focused on the preliminary and detailed design phases regarding aerodynamics and flight performance studies.

The preliminary phase encompasses the wing and tail design, with the aid of XFLR5, together with an estimate of the total aircraft drag by resorting to semi-empirical expressions. A longitudinal static stability analysis is conducted, and the unmanned aerial vehicle characteristics are presented after the preliminary phase of the project.

For the detailed analysis, Fluent was chosen as the computational fluid dynamics software to be used. 2D simulation over the SG6042 wing airfoil validated the choice of the SST turbulence model, coupled with the $\gamma - Re_\theta$ transition model, as the results were consistent with experimental data. The drag polar of the wing is obtained by simulating the 3D wing at various angles of attack. To enhance the wing aerodynamic properties, twist was given to the wingtip, moving the stall region from the wingtip to the root. The impact of the vertical propulsion system on the drag at cruise is assessed by performing wind tunnel tests and simulations on Fluent. Simulations of the entire aircraft conclude that, depending on the stopping position of the rotors, the drag of the aircraft varies between 16.32 and 19.22 N for cruise, which results in a total flight time between 3H05 and 3H25.

Keywords: Aerodynamics, Computational Fluid Dynamics, Fuel Cell, Hydrogen, Unmanned Aerial Vehicle, Vertical Take-Off and Landing.

Contents

List of Tables

List of Figures

Abbreviations

AFA	Academia da Força Aérea
AoA	Angle of Attack
BL	Boundary Layer
CAD	Computer Aided Design
CAE	Computational Aided Engineering
CFD	Computational Fluid Dynamics
CG	Center of Gravity
CIAFA	Centro de Investigação da Academia da Força Aérea
DNS	Direct Numerical Simulation
ESC	Electronic Speed Controller
FAP	Força Aérea Portuguesa
FDM	Finite Difference Method
FEM	Finite Element Method
FVM	Finite Volume Method
ICE	Internal Combustion Engine
LES	Large Eddy Simulator
LLT	Lifting Line Theory
LRN	Low Reynolds Numbers
LSB	Laminar Separation Bubble
MTOM	Maximum Take-Off Mass
PITVANT	Projeto de Investigação e Tecnologia em Veículos Aéreos Não-Tripulados
RANS	Reynolds Average Navier-Stokes

RoC	Rate of Climb
RPM	Rotations per Minute
SA	Spalart-Allmaras
SIMPLE	Semi-Implicit Method for Pressure Linked Equations
SST	Shear-Stress Transport
TE	Trailing Edge
UAV	Unmanned Aerial Vehicle
UIUC	University of Illinois at Urbana-Champaign
VLM	Vortex Lattice Method
VTOL	Vertical Take-Off and Landing

Nomenclature

Greek symbols

α	Angle of Attack.
$\beta_{0.7r}$	Rotor Incidence Angle (at 70% radius).
δ	Maximum Boundary Layer Thickness.
δ^*	Boundary Layer Displacement Thickness.
ϵ	Dissipation Rate of Turbulent Kinetic Energy.
η	Efficiency.
Γ	Dihedral Angle.
γ	Intermittency.
λ	Taper Ratio.
μ	Molecular Viscosity Coefficient.
μ_t	Eddy Viscosity.
ν_t	Kinematic Eddy Viscosity.
ω	Specific Dissipation Rate of Turbulent Energy.
ϕ	Rotor Stopping Position.
ρ	Density.
τ_w	Wall Shear Stress.
$\varphi_{0.25c}$	Sweep Angle (at 25% Chord).

Roman symbols

AR	Aspect Ratio.
C	Volume Coefficient.
c	Chord.

D Drag Force.

e Oswald Efficiency Factor.

E^*_{H2} Hydrogen Specific Energy Density.

e^N Amplification ratio.

e_f Finite Wing Efficiency Factor.

FF Form Factor.

K Induced Drag Factor.

k Turbulence Kinetic Energy

L Lift Force.

l Characteristic Length.

l/d Fineness Ratio.

$m_{H2\ cr}/m_{H2\ tot}$ Hydrogen Mass Percentage Available for Cruise.

$m_{H2\ tot}$ Total Hydrogen Mass.

Ma Mach Number.

N_e Number of Engines over the Wing.

P Power.

p Pressure.

P_{PPS} Power Required by the Payload and Primary Systems.

Q Interference Factor.

q Dynamic Pressure.

R Ideal Gas Air Constant.

Re Reynolds Number.

Re_θ Momentum-Thickness Reynolds Number.

S Surface Area.

S_μ Sutherland Temperature Constant.

S_{wet} Wet Area.

T Temperature.

t Time.

t/c Airfoil Thickness-to-Chord Ratio.

U Longitudinal Velocity.

u_τ Wall Friction Velocity.

W Weight.

y_B Boom Spanwise Position.

C_D 3D Drag Coefficient.

C_d 2D Drag Coefficient.

C_f Skin-Friction Coefficient.

C_L 3D Lift Coefficient.

C_l 2D Lift Coefficient.

C_p Pressure Coefficient.

C_{D_0} Parasite Drag Component.

C_{D_i} Induced Drag Component.

C_{l_i} Airfoil Ideal Lift Coefficient.

C_{M_α} Pitching Moment Derivative with Respect to Angle of Attack.

Subscripts

∞ Free-stream Condition.

i, j, k Computational Indexes.

x, y, z Cartesian Components.

cr Cruise Conditions.

HT Relative to the Horizontal Tail.

max Maximum Conditions.

pr Relative to the Propeller.

ref Reference Condition.

T Relative to the Tail.

VT Relative to the Vertical Tail.

Superscripts

' Fluctuating Component.

+ Dimensionless Unit.

Chapter 1

Introduction

1.1 Topic Overview

The idea of flying has pursued mankind since ancient times with the famous tale of Icarus from the Greek ancient civilization. Although most known primordial flight projects and pioneers (e.g., Leonardo da Vinci 1452-1519 and Montgolfier 1783) are related to manned piloted devices, unmanned vehicles have had a parallel yet more discrete and delayed evolution over the years. Unpiloted aerial systems are known by many nomenclatures and acronyms, like Unmanned Aerial System, Remotely Piloted Aircraft, and Unmanned Aerial Vehicle (UAV), among others (Prisacariu, 2017). The latter will be the preferred term throughout the presented thesis.

Early contributions to autonomous mechanics go back to the IV century BC with Archytas of Tarantas creating a mechanical bird and China documenting the idea of vertical flight. However, only during the XIX century, the first vertical flight machines were created using boilers and steam to provide power to small embryonic propellers, with the credits attributed to Phillips in 1840 and d'Amécurt in 1860. The first report of the usage of unmanned combat air vehicles dates to 1849, when the Austrians attacked Venice with unmanned balloons loaded with timed bombs (Prisacariu, 2017). Ever since that time, UAV development has increased and accelerated during military necessity events such as World War I and II and the Cold War, with most superpowers now possessing a wide range of UAVs at their disposal to conduct various missions such as surveillance, communication relay links, ship decoys, and detection of biological, chemical, or nuclear materials (Mueller & DeLaurier, 2003). Nowadays, some missions are being assigned solely to unmanned aerial platforms, formerly performed by combat piloted aircraft. One example is the "drone strike" performed by the United States in Afghanistan on August 28th, 2021, which successfully completed its assigned mission without putting the lives of any US military personnel at risk (BBC, 2021).

Similar to piloted aircraft, the demand for new and improved capabilities reached the UAV platforms, including the ability to perform Vertical Take-Off and Landing (VTOL), a characteristic historically attributed to pure rotary-wing aircraft. The ability to take-off vertically without a runway increases the flexibility of the platform, and being able to hover and perform slow lateral and longitudinal movement

is preferred and sometimes a must for emergency response or precise transport missions, for example. Airspeed constraints, especially in forward flight conditions, are known limitations of rotary-wing aircraft, therefore hybrid platforms that include both rotary and fixed-wing aspects have been developed and are desired. The fuel efficiency and propulsion system efficiency are the main weaknesses of these hybrid platforms, not being quite as good as their traditional fixed or rotary-wing counterparts (Mrusek, 2021).

While there are several possible configurations for hybrid platforms, they can be divided into two categories: the first one uses the same propulsion system in both vertical and horizontal flight by either tilting the propulsion system – Tiltrotor (Figure. 1.1a), rotation of the wing – Tiltwing (Figure. 1.1b), or even by rotating the entire aircraft – Tailsitter (Figure. 1.1c). The second category encompasses the designs which have the vertical flight propulsion system segregated from the horizontal flight, commonly named Lift+Cruise configurations or transitional aircraft (Figure. 1.1d). This latter configuration tackles some of the drawbacks presented before since each propulsion system can be optimized for a single flight condition and does not require complex tilt mechanisms, however, both propulsion systems add up to an increase of the total aircraft weight (Serrano, 2018).

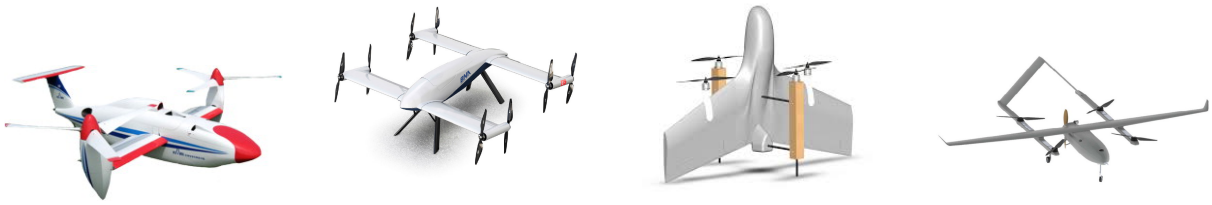

(a) Tiltrotor (Park et al., 2013) (b) Tiltwing (Defense Turkey, 2017) (c) Tailsitter (Li et al., 2018) (d) Lift + Cruise (UAVision, 2020)

Figure 1.1: Market study of possible hybrid UAV configurations.

An UAV with a similar configuration to the one depicted in Figure. 1.1d is the Top Engineering Falcon 5 UAV. It has the traditional gasoline Internal Combustion Engine (ICE) to provide power to the propeller and has a maximum flight time of five hours. An interesting fact about this UAV is that the ICE can be replaced by an electric motor and the aircraft becomes fully electric, requiring batteries instead of a fuel tank. This modification increases the UAV weight and reduces the endurance to two hours, a reduction in the total flight time of 60% (Group, 2014). Additionally, a fuel cell, fed by liquid hydrogen, can replace the ICE on the same UAV, making it a greener alternative to fossil fuels. Nevertheless, this modification also comes with a reduction in the total endurance to three hours in total (Group, 2014).

The use of hydrogen in aviation dates back to the golden age of space exploration and is now cited as one of the contenders to replace fossil fuels in the aviation industry (Airbus, 2020b). One way of using hydrogen as an energy source is with a fuel cell which converts oxygen and hydrogen into water and electric energy. The energy in 1 kg of hydrogen gas at 350 bar (the usual pressure of the UAV's on-board cylinders) is the same as the energy in 2.8 kg of gasoline, making a fuel cell coupled with an electric motor two to times more efficient than a gasoline ICE (Intelligent Energy, 2021; U.S. Department of Energy, 2021). Moreover, fuel cells tend to be more efficient power sources when compared to conventional batteries for steady flight conditions (Gadalla & Zafar, 2016). However, two main drawbacks are pointed out to this new technology: there are no fuel cells with a specific power high enough for its

usage on larger scale projects (Ng & Datta, 2019), with studies from 2018 reporting a maximum power density of 1.6 kW/kg, but with suppliers predicting this value to grow by a factor of five in the near future (Intelligent Energy, 2021; Kadyk, Winnefeld, Hanke-Rauschenbach, & Krewer, 2018); the weight of the fuel storage unit is substantial as it must safely contain high-pressure gases or liquids. For instance, the storage tank of the Ion Tiger UAV – Figure. 1.2a – composes one-third of the total aircraft weight, and if combined with the fuel cell system and the fuel itself, it adds up to 46% of the UAV weight (Figure. 1.2b) (US Naval Research Laboratory, 2018).

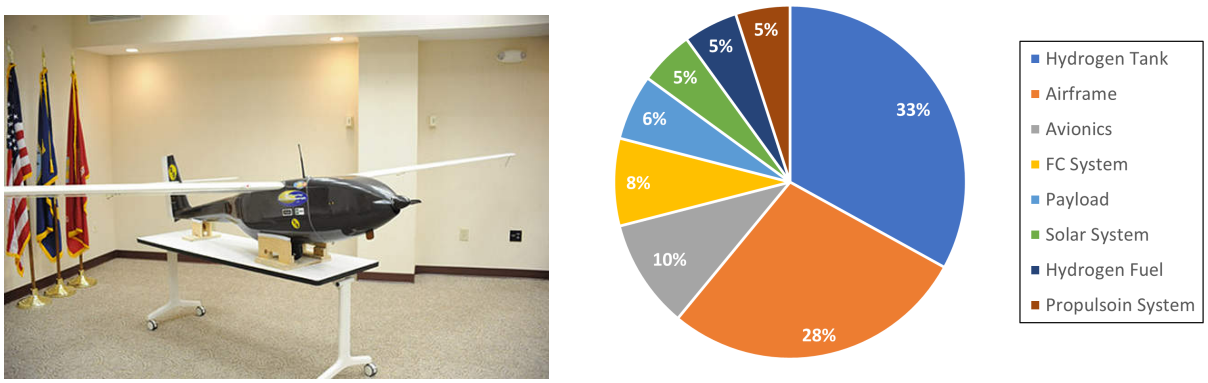

(a) Ion Tiger prototype (US Naval Research Laboratory, 2018)

(b) Mass breakdown of Ion Tiger. Adapted from US Naval Research Laboratory (2018)

Figure 1.2: Ion Tiger UAV.

While two examples were put forward in this chapter, their characteristics should not be blindly extrapolated as general conclusions; each aircraft has its own properties and requirements, and extensive studies into each specific case should be performed to understand which is the best solution.

1.2 Motivation

The Portuguese Air Force (FAP) is an organization focused on its mission of cooperating towards the military defense of the Portuguese Republic and its airspace, including missions of public interest to satisfy the population's needs. To accomplish these objectives, one of its cornerstones is related to sustainability and efficiency, and the innovation, research, and development of new technologies (Força Aérea, 2021). The strategic vision of FAP regarding unmanned aerial vehicles is presented in MFA 500-12, published under the title of "Strategic Vision for Autonomous Unmanned Aircraft Systems", defining the development and operation of UAVs as a complement to accomplish its mission (Morgado, Santos, & Caetano, 2017).

The Air Force Academy Research Center (CIAFA) is the primary source of innovation in aeronautics within the organization, conducting aeronautical research and development while also operating small UAVs on missions. Its activities began in 2006, and in 2009 it was approved for a major project called PITVANT (Projeto de Investigação e Tecnologia em Veículos Aéreos Não-Tripulados), with the goal of implementing a research, development, and innovation methodology centered on the development of UAVs within the FAP for maritime surveillance and search and rescue missions. Between other projects

with external partners and financing, such as PERSEUS and SEAGULL, by 2017, CIAFA had accumulated over 750 flight hours on Class I UAVs (less than 150 kg (Joint Air Power Competence Centre - NATO, 2010)) and managed to implement a successful collaboration between academic research (small scale projects and scientific dissertations) and the operation of the developed technology (Morgado et al., 2017).

With this innovation scope in mind and paired with the development of emerging energy sources on the aeronautical market, their implementation needs to be studied and analyzed. While ICE-powered UAVs are preferred for long-duration missions, fossil fuels pose a serious environmental and economic problem because they are the primary cause of the increase in CO2 presence in the atmosphere (Boukoberine, Zhou, & Benbouzid, 2019). Global warming awareness has grown and zero-emission policies including various sectors of society are being applied to tackle this problem. In the aviation sector, full decarbonization is expected to occur within the second half of the XXI century, in agreement with the goals defined in the Paris Agreement (United Nations Climate Change, 2018).

Battery-powered UAVs may pose as an alternative to ICE-based ones. They have several advantages, including lower noise and thermal signatures, and no pollutant emissions, however, their low energy density and long charging time prevent them from being used on large-scale projects (Airbus, 2020a). Another runner-up for replacing fossil fuel usage in UAVs is by using hydrogen as its fuel source. While hydrogen is traditionally obtained by using electricity from fossil fuels in the electrolysis process to separate the hydrogen from the oxygen, thus giving origin to the term ”grey hydrogen”, ”green hydrogen” production, which uses electricity from renewable sources, will tend to increase over the coming years, making hydrogen a fully zero-emission fuel source (Airbus, 2020b).

Fomented by this constant innovation pursued by the Air Force and the emerging use of hydrogen in the aeronautical field, a design proposal for a small Class-I UAV has been made, which led to the present project and dissertation.

1.3 Initial Design Requirements

The design proposal presents some general characteristics required for the UAV, including the ability to perform Vertical Take-Off and Landing and having a fuel cell as its primary source of energy. Some of the main performance and operational requirements are listed in Table 1.1.

1.3.1 Objectives & Deliverables

This thesis is part of an embryonic project proposed by CIAFA to develop an UAV powered by a fuel cell that uses hydrogen as its fuel source. Additionally, it should carry surveillance and photography equipment as payload and be able to perform VTOL to increase its flexibility.

Although a design project encompasses various areas like aerodynamics, propulsion, structures, control, optimization, among others, the objective of the current dissertation is to obtain the aerodynamic and flight performance characteristics of the aircraft, both in the preliminary and detail stages

Table 1.1: Design proposal presented by CIAFA.

Requirement	Value	Description
MTOM	$<$ 25 kg	–
Payload	2 kg	Includes a daylight camera
Endurance	$>$ 2 h	Preferable over 3 hours
Cruise Speed	35-45 kts	–
Stall Speed	$<$ 25 kts	Without flaps
Maximum Speed	70 kts	Level flight
Ceiling	15 000 ft	–
Takeoff & Landing	-	VTOL, fully autonomous
Maximum Takeoff Altitude	10 000 ft	Above mean sea level
Engine Type	-	Electric

of the design process. After an initial phase in which the design team came up with an initial concept for the UAV and some baseline characteristics were determined, the author focus his studies on the aerodynamic domain.

To perform the objective proposed for the current dissertation, the author makes a division into the following sections:

- Theoretical background:

  Review of some fundamental concepts regarding general aerodynamic definitions, design features for the lifting surfaces and computational methods to be applied in the detailed design phase.

- Conceptual design:

  While the conceptual design is part of a common project of four MSc proponents, initial performance considerations proposed by the author at this phase are presented.

- Preliminary design:

  Definition of the wing and tail geometry, together with predictions concerning the flight performance of the aircraft and longitudinal static stability.

- Detailed design:

  Application of the Computational Fluid Dynamics (CFD) methodology prescribed to validate the models to be used; verification of the aerodynamic properties of the UAV using high-fidelity software tools.

1.3.2 Project Outline

Based on design proposal, an initial concept was developed by the four MSc proponents which culminated in a baseline solution. The considerations and methodology followed in the conceptual design step, along with the characteristics of the UAV at the end of this design phase are available in a paired revised conference article through reference (Alves et al., 2021). With the conceptual stage concluded,

Alves started working on optimizing the initial concept (Alves, 2021) and Silva, Sá and the author extended the initial design into its preliminary and detail design phase in the propulsion, structural and aerodynamic areas, respectively (P. Silva, 2021; Sá, 2021).

It is important to note that after the conceptual design phase, the baseline solution is said to be 'locked' meaning that changes proposed by each member of the design team during the preliminary and detailed design are not considered for the remaining dissertations. During the course of the preliminary and design phase, the author mentions the remaining areas whenever some minor inputs are required for his work.

1.4 Thesis Outline

This thesis is divided into eight main chapters. Chapter 1 provides an introduction for this thesis, together with the motivation and the design requirements of the project.

Chapter 2 gathers information over some aerodynamic concepts and design properties of wings and tails, along with theoretical background on the software to be used further into the thesis and the computational methods to be employed.

In chapter 3, insight on some aerodynamic and performance considerations done on the conceptual design phase is given, which were fundamental on the process to obtain the baseline solution.

Chapter 4 encompasses the preliminary design phase where the wing and tail geometry is defined and quick, low-fidelity software tools are employed to obtain aerodynamic data. The work done by all the project members in the preliminary design step is put together and the characteristics and performance of the UAV are updated.

The methodology to perform CFD simulations is tested and validated in chapter 5, providing important feedback to be considered in later simulations.

In chapter 6, the CFD methodology is applied to a 3D model of the wing and the whole aircraft. Improvements on the baseline solution are discussed, together with the impact of the VTOL propulsion system during cruise. The aerodynamic properties of the UAV, obtained using high-fidelity software, are presented at the end of the chapter

The dissertation is completed with a general overview of the project in conjunction with conclusions taken from the various stages of the design process. Recommendations for future work and development of the project are made in order to bring the designed UAV closer to production.

Chapter 2

Literature and Technology Review

To fulfill the objectives of the present dissertation, the influence of the airframe configurations and wing geometry parameters on the performance of the aircraft is revised. As a result, simple aerodynamics considerations like force decomposition, types of drag, boundary layer, are considered known by the reader and thus are briefly mentioned by the author at the beginning of this chapter. The computational software used throughout the dissertation is mentioned, along with the theoretical background, methodology, and models they apply.

2.1 Aerodynamic Considerations

The aerodynamic force acting on a plane is the sum of all the forces on the airframe caused by the moving airstream, which creates a pressure and a shear stress distribution over the body surface (Anderson, 2010). These forces can be split into a lift component, perpendicular to the free stream direction, and a drag component aligned with the free stream (Lowry, 1999). For a steady level powered flight, lift is equal to the aircraft's weight and drag is equal to the thrust produced (Roskam & Lan, 2016).

2.1.1 Drag

Drag is a force caused by the disruption of the airflow by the airframe (Federal Aviation Administration, 2016). Drag force is usually divided into two components: the parasite drag, which is non-dependent on the lift production, and the induced part, defined as the component ”induced” by the lift production, as the name suggests (Roskam & Lan, 2016).

Parasite drag can be further detailed into form, skin friction, and interference drag. Form drag, or pressure drag, occurs when airflow deviates from its original path around the aircraft's shape (Federal Aviation Administration, 2016); if flow separation occurs, this drag component contributes significantly to parasite drag (Anderson, 2012). Skin-friction drag is related to the shear forces acting in the boundary layer normal to the surface due to the viscosity of the flow (Gundlach, 2012). According to Gundlach (2012), interference drag is caused by the interference of two or more aerodynamic bodies that are not necessarily in direct contact (the tail being in the wake of the wing, for example).

Induced drag occurs due to the downwash produced by the wingtip vortices. Anderson (2010) presents an in-depth explanation for the induced drag origin and phenomena. When considering only the wings, Equation (2.1) illustrates the relation between the induced drag coefficient C_{D_i} and the lift coefficient C_L, where AR is the aspect ratio of the wing and e_f represents the span efficiency factor of a finite wing which varies between 0.9 and 1.0, being closer to the unit the closer the wing is to an elliptical one (Anderson, 2010).

$$C_{D_{i\ wing}} = \frac{C_L^2}{\pi A R e_f} \tag{2.1}$$

Wave drag is an additional component that influences both parasite and induced drag and occurs at flight speeds higher than the critical Mach number due to the presence of compressibility effects such as shock waves (Raymer, 1992). For low subsonic speeds, compressibility effects are negligible and thus, not relevant to the scope of the current thesis.

Equation (2.2), also known as the aircraft drag polar represents the total aircraft drag coefficient as the sum of the aircraft parasite drag coefficient at zero lift – C_{D_0} and the drag coefficient due to lift, with the latter being given by the same expression as Equation (2.1), however, when considering the entire aircraft, e is denominated the Oswald efficiency factor and its value typically ranges from 0.7 to 0.85 depending on the aircraft design (Anderson, 2010). The parameters which multiply the square of the lift coefficient are commonly grouped using the K notation and represent the induced drag factor (Sadrey, 2013).

$$C_D = C_{D_0} + KC_L^2 = C_{D_0} + \frac{C_L^2}{\pi A R e} \tag{2.2}$$

2.1.2 Boundary Layer

The boundary layer (BL) is the thin region of flow in contact with a surface, where the flow is retarded due to the influence of shearing forces on the surface, originating a velocity profile from zero at the surface due to the no-slip condition, to the freestream velocity where the influence of the shear forces does not impact the flow (Anderson, 2010). The no-slip condition occurs between a solid surface and a fluid, and depends on the viscosity of the latter, as such, a dimensionless parameter denominated Reynolds number – Re is used to define the relative influence of viscosity when compared to the inertial forces of the fluid – Equation (2.3).

$$Re = \frac{\rho U l}{\mu} \tag{2.3}$$

Reynolds number accounts for the density of the air – ρ, the freestream velocity – U, a characteristic length – l, and the dynamic viscosity of the fluid – μ. For wings, the mean aerodynamic chord is chosen as the characteristic length. Small UAVs have lower Reynolds numbers than commercial aircraft because of their lower flight speeds and smaller size, typically less than 5×10^5, defined as the Low Reynolds Number (LRN) regime, according to Gundlach (2012).

The BL can be divided into three regions: an initial laminar region characterized by a highly ordered motion of the flow; a transition region where the boundary layer becomes unstable and the presence of Tollmien-Schlichting waves induces the transition to turbulent flow, originating a third region marked by a chaotic and irregular nature of the flow, governed by chaotic fluctuations over an average flow field (Brederode, 2018; Schlichting, 1979).

Under LRN, laminar flow occurs over the airfoil even after the minimum pressure point. Due to the adverse pressure gradient downstream of this location, the flow separates from the surface, forming a shear layer. At Reynolds numbers over 5×10^4 transition occurs and, if the adverse pressure gradient is not too large, the flow can recover sufficient energy through entertainment to reattach to the airfoil surface and redevelop a turbulent BL. The region between the separation and the reattachment, visible in Figure 2.1 between points S and R, is denominated as the Laminar Separation Bubble (LSB) or transitional separation bubble since it induces flow transition (Mueller & DeLaurier, 2003).

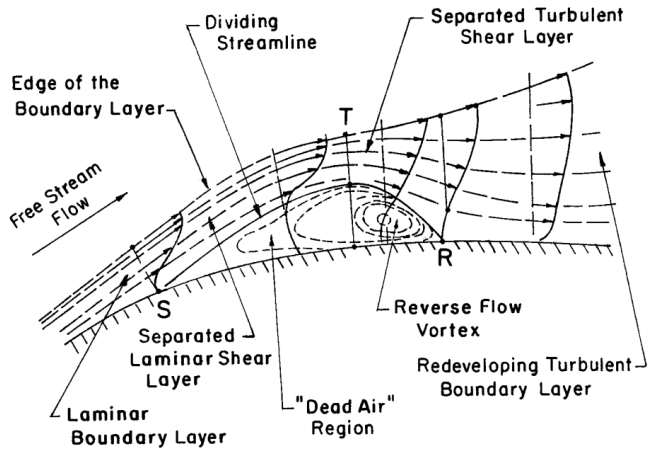

Figure 2.1: Laminar separation bubble. Retrieved from Mueller and DeLaurier (2003).

Focusing the study on Reynolds above 7×10^4 which excludes most of the Micro UAVs, the LSB is present and occupies a significant portion of the airfoil. As the angle of attack increases, the reattachment point gets closer to the trailing edge, increasing the size of the bubble. When the necessary pressure for the reattachment is not present, the bubble bursts, causing the airfoil to stall. For higher Reynolds number (over 2×10^5), still within the LRN scope, the LSB is shorter and fully induces transition to turbulent flow; a short bubble reduces pressure drag while turbulent flow increases skin-friction drag when compared to laminar flow (Mueller & DeLaurier, 2003).

2.2 Design Features

2.2.1 Airframe Configuration

Airframe configurations for UAVs are vast and even more when compared with crewed aircraft since the commercial risk in trying innovative solutions is less for unmanned aircraft and there is no need to accommodate space for the flight crew. Furthermore, UAV airframes are usually much smaller than

human-piloted aircraft (Austin, 2010).

Having the conceptual design in mind, the author chose to narrow the airframe configurations study to the ones which can be applied into a Lift+Cruise configuration, not focusing on traditional VTOL configurations such as single rotors, the common quad-copter or any other hybrid configurations (e.g. tilt-rotor, tilt-wing, tail sitter) since these configurations were analyzed in the initial design phase with the concept generation and they are described in detail on reference (Alves et al., 2021).

One decision that should be made is to select the number of wings. While biplane and triplane configurations were common in the early days of aviation, one wing configurations became the standard in aviation (Sadrey, 2013). However, when considering the location and the presence of control surfaces, aircraft configurations can be categorized into 'tailplane aft', 'tailplane forward', 'three surfaces' or 'tailless' (Austin, 2010) A summary of the main characteristics of each configuration is presented, retrieved from references (Austin, 2010; Gundlach, 2012; Raymer, 1992; Sadrey, 2013).

- Tailplane aft:
  - The center of gravity (CG) of the aircraft is located ahead of the wing center of lift;
  - The tail is located after the wing and has the elevator and rudder (or a combination of both);
  - Allows for a single-boom or twin-boom tail design;
  - The tail produces a negative lift contribution to trim the aircraft.
- Tailplane forward (canards):
  - Canards are ahead of the wing;
  - The CG is located ahead of the wing, therefore, canards create positive lift to trim the aircraft;
  - The wake of the canards interfere with the freestream of the wing, compromising the lift generation of the latter.
- Three surfaces:
  - Is a combination of the previous configurations, by having a tail and canards;
  - Has a higher margin for the CG location;
  - Extra surfaces increase the parasite drag, aircraft weight and complexity.
- Tailless:
  - Does not possess neither a tail, nor canards;
  - The ailerons at the wing are responsible for both the lateral and longitudinal control;
  - The longitudinal control is compromised due to the ailerons short arm;
  - May require a vertical fin for aid in yaw control.

The main wing can be categorized as high, mid, or low, depending on its vertical placement. Each configuration has its advantages and disadvantages, as such, some remarks concerning its application

in UAVs are considered. High wings allow the placement of the fuselage closer to the ground, although this limits the integration of external payload at the bottom of the fuselage, like cameras, for instance. If the wing is positioned over the fuselage, the wing spar can be a continuous beam, structurally favorable at the cost of an increase in the frontal area and, consequently, the overall drag. A low wing layout has increased maneuverability yet lower ground clearance. To increase lateral stability, low wings commonly have dihedral associated to them. A mid-wing is a compromise between the previous configurations and it presents the lowest interference drag. Nevertheless, the wing spar has to be cut in two sections if payload is to be carried on the fuselage at the wing location and the wing root intersection with the fuselage has to be reinforced, increasing the structure weight (Sadrey, 2013).

2.2.2 Wing Geometry

The wing geometry has an impact on how much drag this structure produces in flight. As seen in Equation (2.2), the aspect ratio of the wing has a significant impact on the induced drag. For the same wing area, the higher the AR, the higher the wingspan is, reducing the strength of wingtip vortices and thus decreasing the induced drag (Raymer, 1992). However, high AR wings are heavier since the structure needs to be stiffened as the wing weight bending moments gets larger, increasing the root bending moment, therefore, requiring a stronger wing root. From a control perspective, on a high AR wing, the ailerons have a longer arm providing more lateral control, however, the mass moment of inertia around the longitudinal axis is higher, decreasing the maneuverability of the aircraft in roll (Sadrey, 2013).

The general planform of the wing impacts its lift distribution. The minimum induced drag occurs when the lift distribution is elliptical, which can be achieved with an elliptical wing planform. While this geometry is desirable, its difficulty in construction prevents its general application in the aviation industry (Raymer, 1992).

A rectangular wing has the simplest geometry. While it is easy to manufacture and has reasonably good performance, it is aerodynamically inefficient by producing induced drag due to the excessive chord length towards the wingtip, as such stall occurs primarily over the root and extends towards the tip, giving room for control at stall conditions due to the location of the ailerons being near the tip.

Taper ratio of a wing is defined as the fraction between the root chord and the tip chord. When taper is applied to rectangular wings, it reduces the tip chord and approximates the lift distribution to the desired elliptical one. Raymer (1992) states: ”A taper ratio of 0.45 (...) produces a lift distribution very close to the elliptical ideal. This results in drag due to lift less than 1 % higher than the ideal, elliptical wing.”. From a structural point of view, applying taper to a wing is also beneficial as the aerodynamic loads on the tip are diminished when compared to an untapered case, resulting in a lower root bending moment. However, with the reduction of the tip chord, these wing sections tend to stall first, which is critical from a control perspective. As a result, taper ratio can be restricted due to the requirement for an adequate chord at the tip for roll control with the ailerons (Howe, 2000). The delta wing is a special case in which taper ratio is equal to 0. This shape is mainly used in high-subsonic or supersonic aircraft, and

its advantages at these flight speeds are coupled with the introduction of sweep (Sadrey, 2013).

The considerations stated above are applied and used for general aviation, and the principles behind them are valid to small UAVs. However, when conducting a market study on similar UAV designs to the one projected, three main planforms have risen: the basic rectangular wing, an elliptical leading edge with a straight trailing edge, and a multi-panel tapered wing. It is relevant to note that for the latter, the tapered sections present higher values (less taper) than the one presented as the ideal to prevent the chord at the tip from being too small.

Sweep angle, more specifically, the leading edge sweep, is the angle between the wing leading edge and the span-wise axis of the aircraft. The main reason to introduce sweep on the wing leading edge is to increase performance at speeds higher than transonic to delay compressibility effects. For the Mach number (Ma) considered, these effects do not occur, and Sadrey suggests that for Ma below 0.3, there should be no leading-edge sweep since sweep increases the effective chord length, reducing the effective thickness-to-chord ratio which, for low speeds, is not ideal (Sadrey, 2013). Sweep angle also influences the performance of the wing control surfaces and the general aesthetics of the plane.

To reduce the tip stall effects from tapered wings and to approximate the lift distribution to the desired elliptical one, one solution is to introduce twist on the wing. This twist can be geometric in nature, in which the tip has a lower incidence than the root, or aerodynamic when there is a difference in the airfoil shape along the wingspan (Sadrey, 2013). When geometric twist is applied, the leading edge of the tip has a lower incidence by around 2° to 6° than the root and the twist evolution along the wingspan is usually linear. One drawback of applying geometric twist is the difficulty in the manufacturing process: the main spar may also need to be twisted, which is problematic if composite materials are used in its construction, since composite fibers' strength is very sensitive to fiber alignment. Aerodynamic twist does not have this problem, as the twist arises from the difference in the stall angle of each of the airfoils chosen for the root and the tip – the tip airfoil has a higher 2D stall angle and is usually thinner (Gudmundsson, 2014).

Dihedral is the angle the wing makes relative to the ground plane when viewing the airplane from the front. Dihedral can be positive if the tip is higher than the root or negative (anhedral) if the opposite is true (Gudmundsson, 2014). Dihedral is applied to improve the lateral stability of the aircraft (the tendency of the aircraft to return to an equilibrium position after a disturbance occurs which makes the aircraft roll) at the cost of a small reduction on the wing effective area which impacts the lift generation (Howe, 2000). Most low-wing configurations have dihedral to guarantee ground clearance for any nacelles or propellers mounted on the wing (Sadrey, 2013).

2.2.3 Tail Configuration

Looking further into the conventional airframe configuration, two main groups of tail configurations arise: single-boom and twin-boom tails, as stated in sub-section 2.2.1. Each group has numerous layouts, however, the author will focus on the twin-boom arrangements. Although they are typically heavier, twin-boom tails are vastly used in conjunction with pusher configurations as they reduce the

overall length of the aircraft (Raymer, 1992).

As referred in Gundlach (2012), there are four main tail configurations for twin-boom design, as seen in the Figure 2.2: Conventional, H-tail, U-tail and Inverted V-tail.

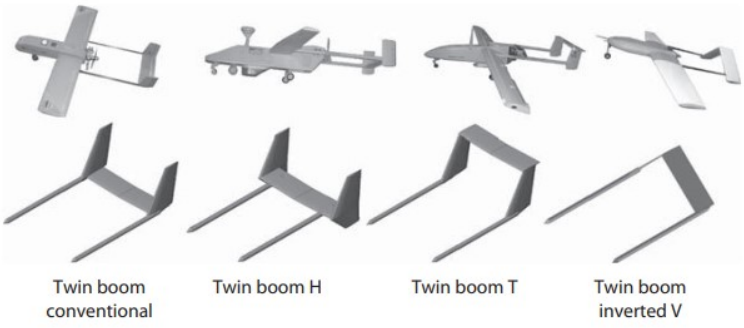

Figure 2.2: Tail configurations for Double Boom Displacement. Adapted from Gundlach (2012).

A twin-boom conventional tail has the horizontal stabilizer on the same plane as the booms and two vertical fins, each one on top of one boom. The vertical fins act as endplates, increasing the effectiveness of the horizontal stabilizer (Gudmundsson, 2014). On an H tail, the vertical stabilizers extend below the horizontal stabilizer plan, making the overall aesthetics more appealing at the cost of lower ground clearance for take-off.

The horizontal stabilizer is in the wake of the propeller in both of the previous designs, increasing the drag produced by it (Gudmundsson, 2014). One solution is to allocate the horizontal stabilizer on top of the fins on the conventional tail, originating the twin-boom T arrangement. While this removes the influence of the propeller wake and the wing downwash on the tail, due to the position of the horizontal tail, the bending moments created by it must be transferred through the main spar of the fins, causing the tail to be structurally more robust and heavier. Moreover, this configuration is subjected to deep stall, a critical condition that occurs when the tail is in the wing wake at stall or post-stall conditions, reducing the capability of the elevators (Sadrey, 2013).

The inverted V-tail, also known as A-tail, has the same advantage as the T-tail by preventing the wake of the propeller and the downwash from the wing to interfere with the tail, providing less drag. This layout also delivers the lowest interference drag when compared with any other tail (Raymer, 1992; Stettmaier, 1999), provides good stability in crosswind conditions (for this scenario, the tail will provide a pitch-up movement). Furthermore, the cost of construction is lower since the parts are symmetric and it uses fewer materials, making it lighter (Fathi, 2019). Nevertheless, this configuration implies a more complex control actuation process since the rudder and elevator control inputs are combined. These new control surfaces are named ”ruddervators” (Raymer, 1992).

2.3 Low-fidelity Software

During the design process, numerical methods and computational simulations can be used at the preliminary phase to corroborate the results from the semi-empirical and historical trends given in the

literature and provide further information. The tools used at this still early phase of the design should be simple and have acceptable reliability while not being time-consuming and computationally heavy.

XFLR5 is an open-source analysis tool for Low-Reynolds-Number airfoils, wings, and planes that is widely used in academia. XFLR5 uses XFOIL for 2D direct and inverse analysis, and for 3D wing simulations, several methods from Lifting Line Theory (LLT), 3D Panel Method, or Vortex Lattice Method (VLM) can be applied at the choice of the user (Deperrois, 2009).

OpenVSP, created in 2012 by NASA, is an open-source parametric aircraft geometry software with an integrated and simplified design tool for wings and fuselages, allowing the user to create a 3D model of an aircraft with ease. It incorporates a parasitic drag tool, in which the user can choose the empirical formulations to use from a wide database, and also a solver for 3D analysis, similar to XFLR5, resorting to VLM or 3D Panels Method (NASA Open Source Agreement, 2021).

While both tools are capable of conducting preliminary aerodynamic analysis, XFLR5 will be used at the early stages of the design process to obtain data regarding the lifting surfaces (wing and tail). The parasite drag tool of OpenVSP is favored when conducting the drag build-up at the preliminary phase since it incorporates models to predict the drag of the remaining aircraft components.

2.3.1 XFOIL

XFOIL is an interactive program for the design and analysis of subsonic, isolated airfoils capable of performing inviscid or viscous analysis while accounting for eventual transition and/or separation of the boundary layer and outputting pressure distribution and drag polars for the required Reynolds and Mach numbers set as user inputs (Drela & Youngren, 2001).

XFOIL inviscid formulation uses a simple linear-vorticity model in which a freestream flow, a vortex sheet on the airfoil surface, and a source sheet on the airfoil surface and wake are superimposed. The airfoil contour and its wake are discretized into flat panels (number of panels being user-specified), with each one having a distribution of the properties stated before. The trailing edge (TE) of the airfoil is closed with a vertical panel and the Kutta condition is applied at the TE to close the system of linear equations. The freestream angle influences the inviscid vortex strengths, providing an inviscid solution for each angle of attack (Drela, 1989; Peerlings, 2018).

Viscosity is introduced by employing von Kármán's momentum integral equation and kinetic energy shape parameter equation and discretizing them over the same panels using two-point central differences (Drela, 1989). These equations incorporate BL properties like the kinetic energy shape parameter, density shape parameter, and skin friction coefficient which have different approximations depending on the flow regime on the BL. For laminar flow, approximations of Falkner-Skan are used, while for turbulent flow, various models presented in reference (Swafford, 1983) are applied.

The transition from laminar flow to turbulent is predicted according to e^N criteria. This method has been used since 1956 and models the growth of Tollmien-Schlichting waves in the boundary layer which are the precursor of the transition. These unstable waves are perturbations of various frequencies, with the most unstable one being characterized by an amplification factor related to its growth rate, the N-

factor. When the amplitudes of the 2D Tollmien-Schlichting waves surpass a certain threshold, transition occurs. The critical amplification factor (at the transition point) N_{crit} typically has a value between 6 and 12 depending on disturbance levels (Wu et al., 2019) and, for airfoils, a value of 9 for N_{crit} is considered the standard (Drela & Youngren, 2001).

The viscous/inviscid coupling is achieved via the surface respiration model, which replaces the source strength presented in the inviscid formulation with the local gradient of mass deflected, related to the boundary layer thickness (Drela, 1989). This approach to the coupling reduces the number of equations to be solved by a Newton non-linear system method and allows a reduction of the computational time to one-third when compared to the full system (Drela, 1989). The low computational effort, together with the capability to accurately account for separation, transition, and bubble losses, makes XFOIL the chosen tool for initial 2D aerodynamic analysis.

2.3.2 Vortex Lattice Method

From the three types of 3D solver methods XFLR5 has to offer, for a wing + tail analysis, only VLM is available, therefore this method is the focus of the literature review. VLM background is based on the theoretical model of a system of vortices that have the same impact as the wing on the flow and sustain a force equivalent to the wing lift (Houghton, Carpenter, Collicott, & Valentine, 2013). According to the Kutta-Joukowski theorem, a bound vortex filament can replace a finite wing and translate its lift force. Moreover, due to the Helmholtz theorem, two free vortices trailing downstream from the wingtips should also be considered. This vortex system is called a horseshoe vortex due to its shape (Anderson, 2010).

In the VLM formulation, the wing surface is split into quadrilateral panels and a horseshoe vortex is placed at one-quarter chord of each panel. Applying the Biot-Savart law and considering the flow tangency condition at control points at 75% of each panel chord, a system of linear equations is set up with the horseshoe vortex strength of each panel as the unknown, which, after solved, can be used to compute lift and induced drag (Peerlings, 2018). The VLM incorporates viscosity by interpolating the lift coefficient from the airfoil 2D analysis done by XFOIL, therefore, results near the stall condition should not be considered (Dantsker & Vahora, 2018).

XFLR5 allows the user to choose between ring vortices instead of the classic horseshoe ones on the VLM formulation. Ring vortices form a close loop with an additional vortex line after the end of each panel and only the panels located after the trailing edge extend downwards to infinity (horseshoe vortices). Figure 2.3 illustrates the difference between the two formulations. Deperrois (2009) states that considering ring vortices is simpler from the programming point of view, nonetheless, both formulations present almost identical results.

Although VLM does not consider thickness in its analysis, it provides results for wings with sweep and dihedral (Peerlings, 2018). For a configuration with multiple surfaces, it takes into consideration the interaction of the wake produced by a forehand surface onto another one downstream of it. Moreover, VLM is capable of estimating stability and control derivatives (Gundlach, 2012), useful for an initial stability analysis done in the preliminary design phase.

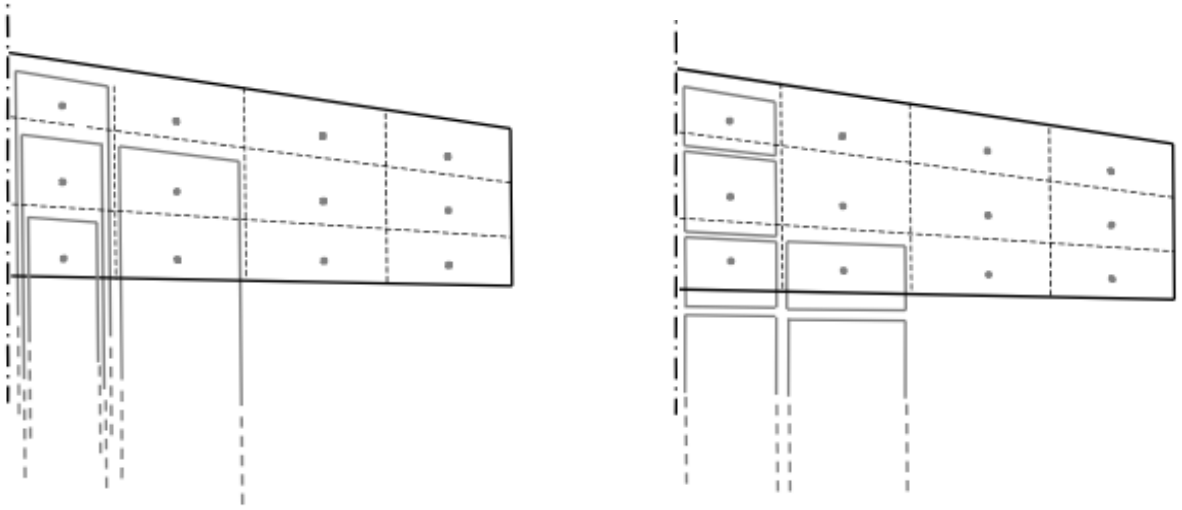

(a) Horseshoe Vortices (b) Ring Vortices

Figure 2.3: Vortex lattice method implementations. Retrieved from Peerlings (2018).

2.4 Computational Fluid Dynamics

Computational Fluid Dynamics is the standard simulation tool in the Computational Aided Engineering (CAE) domain for design, analysis, performance determination, and investigation of engineering systems involving fluid flows. Initially used by the aeronautics and aerospace industry, it has grown in applications and become an essential tool for other design-intensive industries such as the automotive, power generation, chemical, nuclear, and marine industries (Moukalled et al., 2015). Due to the complexity of the fluid governing equations which need to be solved, the development and evolution of CFD software is linked with the technological advances of the past three decades, namely the increase in memory capacity and more affordable computer speed, leading to a steady reduction in the cost of simulations when compared to traditional experimental testing (Hirsch, 2009). In the aeronautical design process, at the preliminary and detailed phases, CFD tools are employed to determine the entire flow field around the aircraft at any conditions specified by the user, unlike wind tunnel testing, which is usually done at a lower scale and some similarity analysis has to be employed to simulate the real-world flight conditions (Raymer, 1992).

To develop a CFD simulation, Hirsch (2009) and Moukalled et al. (2015) present a systematic step-by-step process that is coherent with the schematic presented by the CFD software of choice. Figure 2.4 represents a diagram with the methodology defined by these two authors, which serves as the basis for the current chapter.

After the identification of the real-world problem to be simulated, the first step is to define the domain of interest and develop a Computer Aided Design (CAD) model of it. For bounded flows or internal aerodynamic problems, the region of interest is easily identified; for external aerodynamic flow analysis, the domain needs to be carefully thought out: the distance between the geometry to be modeled and the far-field should be large enough to prevent the boundary conditions applied at the outer bounds of the domain from interfering with the flow next to it and affecting the quality of the obtained results (Ideal

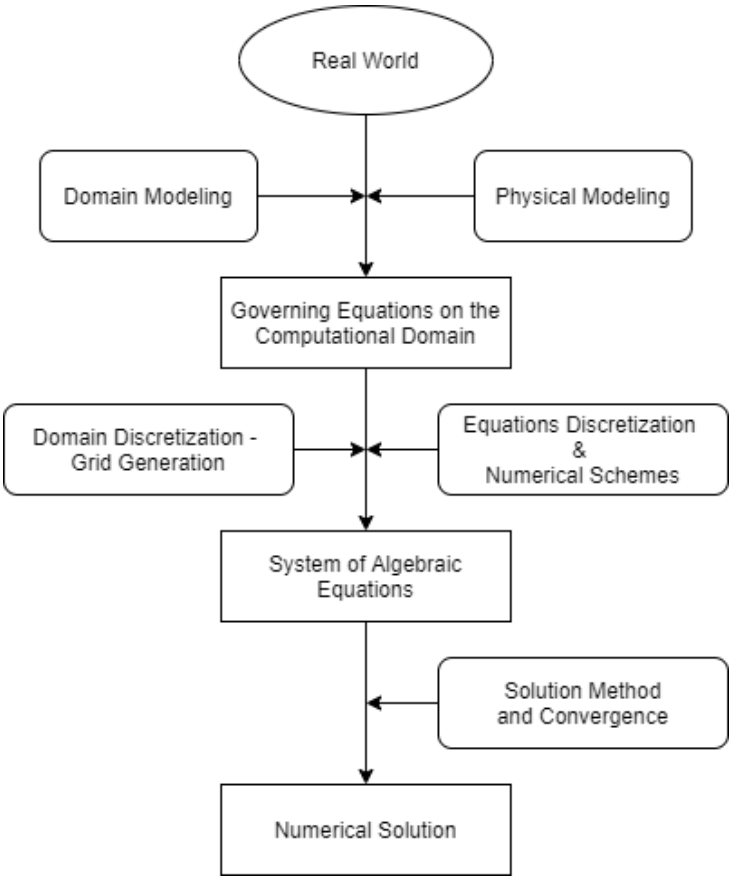

Figure 2.4: Structure of a CFD simulation system. Adapted from Hirsch (2009); Moukalled et al. (2015).

Simulations, 2020). In parallel with the domain modeling, the physical phenomenon is mathematically postulated, and some approximations must be made in some cases (Moukalled et al., 2015). Section 2.4.1 presents some insight into the physical modeling process.

With the governing equations and the computational domain set, the geometrical and mathematical models which are continuous are translated into discrete and numerical counterparts, through the discretization process. The geometry is discretized into a set of points representing the real space, forming a grid or a mesh (Hirsch, 2009). Similarly, the governing equations are discretized into a set of algebraic equations and applied to each element of the mesh created (Moukalled et al., 2015). Both the domain and equations' discretization processes are further detailed in sections 2.4.2 and 2.4.3, respectively.

The system of algebraic equations from the previous step must be solved to obtain the discrete values of the variables to be calculated. Direct or iterative methods may be used. The former is based on inverting the matrix of coefficients of the system of algebraic equations, which requires large computational and storage requirements for problems with hundreds of thousands of cells, this being rarely used for complex CFD simulations. Iterative methods rely on an initial value and a guess-and-correct procedure to obtain more accurate solutions, repeatedly solving the set of equations. This iterative process continues until a stopping criterion is met, related to the difference between the ongoing solution and the previous iteration. Whenever this difference decreases with the number of iterations, the process is said to be converging, which is a must to guarantee that the solution is acceptable (Moukalled et al., 2015).

Software Solutions

To perform CFD simulations, both commercial and open source software packages are available for use.

Star-CCM+ is a commercial software from Siemens which has an integrated environment including all phases of the CFD process, from developing the CAD model to creating the mesh and modeling the physics. Its post-processing capabilities are remarkable and it is recognized as a reference for aeronautical applications (Siemens, 2021).

The Ansys package contains a wide variety of analysis systems in the engineering domain, from material and structural analysis to fluid simulations, easing the coupling of these two domains if required. Fluent and CFX are the Ansys reference analysis systems for fluid simulations, both having an integrated environment similar to Star-CCM+, each one with its applications in the aeronautical field. (Ansys Inc., 2021). Due to its accurate results, versatility and the option to use a free student version to familiarize and solve simple problems and test cases, Ansys has become a staple tool in the CAE domain.

OpenFOAM has been the leading free open source CFD software since 2004, largely used for industrial applications and in academia. It is capable of dealing with an array of problems, from heat transfer and turbulence to acoustics and chemical reactions. It also has meshing, pre-processing, and post-processing tools embedded with the CFD package (OpenCFD Ltd, 2021).

Since the Air Force Academy (AFA) possesses the academic license for the Ansys 2019 package, without restrictions on the meshing number of elements/nodes, it is the software of choice for the presented thesis regarding high-fidelity CFD simulations. Between Fluent and CFX, Fluent is chosen due to its advanced physics modeling in aeronautical applications to freestream flows and user-friendly interface, while the latter is recommended for turbomachinery applications (Ansys Inc., 2021).

2.4.1 Physical Modeling

The governing equations in fluid dynamics are known as the Navier-Stokes equations, expressing the conservation of mass, momentum and energy through a system of five fully coupled time-dependent partial differential and nonlinear equations. For an incompressible flow, the energy equation becomes decoupled from the remaining Navier-Stokes equations whenever viscosity is assumed to be independent of the temperature, a simplification valid for low-speed cases where the fluid is considered isothermal. While laminar flows are well solved using computational methods without any additional information, turbulent flows are chaotic and involve 3D vorticity fluctuations (Hirsch, 2009).

One way to model turbulence is to assume the presence of eddies of different sizes in which the energy they carry is dependent on their dimensions. Larger eddies break up and transfer their energy into smaller ones until the smallest eddy size is reached and their molecular viscosity dissipates the turbulent kinetic energy as heat. This turbulence modeling approach is applied in Direct Numerical Simulation (DNS), however, it requires a very small time step and a mesh fine enough to capture these tiny eddies, resulting in a computational cost that is extremely high and still not viable to solve industrial problems with the current computational power and memory (Moukalled et al., 2015). To reduce the

large computational cost associated with a direct solution of the Navier-Stokes equations, Large Eddy Simulation (LES) is an approach similar to DNS which models the larger-scale eddies to directly simulate the turbulent fluctuations (Hirsch, 2009).

The most widely used approach is the Reynolds Averaged Navier-Stokes (RANS). In this model, a statistical averaging, presented in Equation (2.4), is applied to approximate random fluctuations, decomposing the flow variables into a time-mean value component – $\overline{\xi}$ and fluctuating one – ξ', substituting in the original Navier-Stokes equations, and time-averaging the obtained equations (Moukalled et al., 2015).

$$\xi(x_i, t) = \overline{\xi}(x_i) + \xi'(x_i, t) \tag{2.4}$$

The RANS equations for continuity (2.5a) and momentum (2.5b) are written in tensor notation, with p denoting the pressure term. Averaging the Navier Stokes introduces additional unknowns to the momentum equation with the term $\rho\overline{u_i' u_j'}$, known as the Reynolds stress tensor. As such, RANS equations are not a closed system of equations and require additional equations in an attempt to derive the Reynolds stress tensor in terms of the mean quantities, denoted as turbulence modeling (Moukalled et al., 2015).

$$\frac{\partial(\rho\overline{u}_i)}{\partial x_i} = 0\,, \tag{2.5a}$$

$$\frac{\partial(\rho\overline{u}_i)}{\partial t} + \frac{\partial}{\partial x_j}\left(\rho\overline{u}_i\overline{u}_j + \rho\overline{u_i' u_j'}\right) = -\frac{\partial\overline{p}}{\partial x_i} + \frac{\partial}{\partial x_j}\left[\mu\left(\frac{\partial\overline{u}_i}{\partial x_j} + \frac{\partial\overline{u}_j}{\partial x_i}\right)\right] \tag{2.5b}$$

The turbulence models can be grouped according to the number of equations they add to the RANS system. Three turbulence models, widely used in commercial CFD software, are presented together with their applications and limitations. Additionally, to accommodate the transition from laminar to turbulent flow, transition models are also applied and two of them, available in Fluent, are mentioned.

Spalart-Allmaras Model

Created by P. R. Spalart and S. R. Allmaras in 1992, the Spalart-Allmaras (SA) one-equation model resorts to a transport equation model for the kinematic eddy viscosity. This model was developed to improve the existing algebraic (zero-equation models) and one-equation models since they treat the BL as a single module, presenting discrepancies when separation occurs or multiple shear layers are present (Spalart & Allmaras, 1992). Being a one-equation model, it is simpler and requires less computational effort than the two-equation models.

The SA model was designed initially for aerospace applications for wall-bounded flows like airfoils, nonetheless, its usage has extended to other fields like turbomachinery applications. This model was validated for the RAE 2822 airfoil, presenting a lift force coefficient consistent with experimental results, giving good results for boundary layers subjected to adverse pressure gradients. Despite the authors' improvements, the presence of massive separations or free vortices appears to be limitations of the SA model (Spalart & Allmaras, 1992).

$k-\epsilon$ Model

The turbulence kinetic energy k and turbulent energy dissipation rate ϵ are computed in this two-equation turbulence model. Developed by B.E. Launder and D.B. Spalding in 1974, its applications are varied, being capable of modeling with acceptable accuracy free shear layer flows, heat transfer problems, and flows in pipes, among others, presented in reference (Launder & Spalding, 1974).

Because the $k-\epsilon$ model is based on the assumption that the flow is fully turbulent and that the effects of molecular viscosity are negligible, it is not recommended for use in LRN applications where the laminar portion of the flow and transition have a significant impact, as such, it is not widely used in external aerodynamics simulations (Ansys Inc., 2013).

SST $k-\omega$ Model

The Standard $k-\omega$ model, first proposed by Kolmogorov in 1942, is a two-equations model which considers the specific dissipation rate ω. Wilcox elaborated on the formulation, simplifying it by considering ω as a ratio of ϵ to k. Wilcox's formulation presents valid results for flows close to walls in the boundary layer, particularly under adverse pressure gradients (Wilcox, 2006).

A modification to the turbulent viscosity formulation to account for the transport effects of the principal turbulent shear stress gave origin to the Shear-Stress Transport (SST) which uses the $k-\omega$ turbulence model in the inner regions of the boundary layer and the standard $k-\epsilon$ model in the outer regions and in free-shear flows (Ansys Inc., 2013).

The SST $k-\omega$ transport equations are presented below,

$$\frac{D\rho k}{Dt} = \tau_{ij}\frac{\partial u_i}{\partial x_j} - \beta^*\rho\omega k + \frac{\partial}{\partial x_j}\left[(\mu + \sigma_k\mu_t)\frac{\partial k}{\partial x_j}\right] \tag{2.6a}$$

$$\frac{D\rho\omega}{Dt} = \frac{\gamma_k}{\nu_t}\tau_{ij}\frac{\partial u_i}{\partial x_j} - \beta\rho\omega^2 + \frac{\partial}{\partial x_j}\left[(\mu + \sigma_\omega\mu_t)\frac{\partial \omega}{\partial x_j}\right] + 2\rho(1-F_1)\sigma_{\omega 2}\frac{1}{\omega}\frac{\partial k}{\partial x_j}\frac{\partial \omega}{\partial x_j} \tag{2.6b}$$

in which τ_{ij} represents the wall shear stress tensor, β, β^*, γ_k, σ_k, σ_ω and $\sigma_{\omega 2}$ are constants, μ_t is the eddy viscosity, ν_t is the kinematic eddy viscosity and F_1 is a blending function that goes from zero away from the surface to one close to the surface. The reference values for the constants are presented in references (Ansys Inc., 2013; Menter, 1994).

By coupling the two-equation turbulence models presented, SST presents good results in either free shear layer flows and in adverse pressure gradient flows on boundary layers, as such this model is widely used in aeronautical applications and has become a reference in this field of CFD (Menter, 1994).

Transition $k-kl-\omega$

In a complement to the $k-\omega$ turbulence model, in 2008, D. Walters and D. Cokljat introduced a third equation to predict the magnitude of low-frequency velocity fluctuations in the pre-transitional boundary layer that have been identified as the precursors to transition. This model improved on the $k-\omega$ model for laminar-turbulent flows, providing accurate data for some test cases like turbulent channel flows, flat plate with pressure gradient, and airfoils, being able to predict the transition location within approximately 10–20% for most of the cases (Walters & Cokljat, 2008).

$\gamma - Re_\theta$ Transition Model

Traditional transition predictions are not able to reliably capture the influence of pressure gradients and separation among other phenomena, as such, in 2006, F. R. Menter and R. B. Langtry proposed a new transition method based on local variables to be compatible with the existing turbulence models. This model postulates two transport equations: one for intermittency γ and one for the transition onset criteria related to the momentum-thickness Reynolds number Re_θ (Menter et al., 2006).

The transport equation for intermittency (2.7a) is used to trigger transition locally, and coupled with the SST $k-\omega$ base model, is capable of accurately accounting for transition caused by the LSB, as described in section 2.1.2. The second equation (2.7b), related to Re_θ, captures the non-local effects of freestream turbulence intensity and pressure gradient at the boundary layer edge. References (Menter et al., 2006) and (Langtry et al., 2006) present further information about the model formulation and validation through test cases. For the reasons stated above, this model is also named SST Transition and encompasses the two equations of the SST turbulence model and the two transport equations related to the transition (Ansys Inc., 2013).

$$\frac{\partial(\rho\gamma)}{\partial t} + \frac{\partial(\rho\overline{u_j}\gamma)}{\partial x_j} = P_{\gamma 1} - E_{\gamma 1} + P_{\gamma 2} - E_{\gamma 2} + \frac{\partial}{\partial x_j}\left[\left(\mu + \frac{\mu_t}{\sigma_\gamma}\right)\frac{\partial \gamma}{\partial x_j}\right] \tag{2.7a}$$

$$\frac{\partial(\rho\tilde{R}e_{\theta t})}{\partial t} + \frac{\partial(\rho\overline{u_j}\tilde{R}e_{\theta t})}{\partial x_j} = P_{\theta t} + \frac{\partial}{\partial x_j}\left[\sigma_{\theta t}\left(\mu + \mu_t\right)\frac{\partial \tilde{R}e_{\theta t}}{\partial x_j}\right] \tag{2.7b}$$

In Equation (2.7a), $P_{\gamma 1}$ and $E_{\gamma 1}$ are transition sources, and $P_{\gamma 2}$ and $E_{\gamma 2}$ are destruction sources. These parameters depend on the length of the transition region and the vorticity magnitude, respectively. $P_{\theta t}$ is a source term in Equation (2.7b) that forces the transported scalar $\tilde{R}e_{\theta t}$ to match the local value of $Re_{\theta t}$, obtained from an empirical correlation outside the boundary layer, and $\sigma_{\theta t}$ and σ_γ are constants. The formulation of these parameters is fully described in (Menter et al., 2006), together with the constants.

2.4.2 Domain Discretization

The computational domain discretization into grid cells to properly define the physical domain is denominated as meshing or grid generation. The mesh influences the accuracy, convergence, and speed of the simulation, therefore, an adequate mesh is essential to provide adequate resolution for the CFD simulation to be run (Moukalled et al., 2015). The grids can have various types and shapes, each with its generation method. The nomenclature for the types of grids varies between the references consulted, as such Hirsch (Hirsch, 2009) will be the base reference to be followed, classifying grids as being structured or unstructured, with various sub-types in each category based on their topology.

A structured grid has its grid points at the intersection of co-ordinates lines, with each interior grid point having a fixed number of neighboring grid points (Versteeg & Malalasekera, 1995). Structured grids possess only quadrilateral (4 faces) elements in 2D meshes and hexagons (6 faces) in 3D, making it possible to attribute a set of indices (i, j, k) to each computational cell, and each neighbor has its own

indices differing by plus or minus one (Moukalled et al., 2015). While structured grids are more efficient in terms of accuracy, processor and memory requirements, they are harder to implement on complex geometries.

Cartesian grids present the gridlines aligned with the Cartesian coordinate system and are the ideal topology from an accuracy point of view. Whenever a local refinement is required, the mesh spacing is reduced locally, forming a denser cell region, resulting in a non-uniform Cartesian grid; or the grid can be sub-divided into smaller cells to adapt to the geometry, forming a quadtree/octree grid (Figure 2.5a). To deal with curvilinear geometries, body-fitted structured grids are employed, with their configuration being related to the letter they resemble the most (H-type, C-type Figure 2.5b, O-type, for example). To increase the flexibility of structured grid generation, a combination of techniques can be applied to various domain zones, forming multi-block grids or even overlapping independent grids in a technique called ”chimera” (Figure 2.5c), the latter being a powerful tool since no extra care is needed for the mesh mating of the different grid topologies, though the overlapping grid zone must be accurately interpolated (Hirsch, 2009).

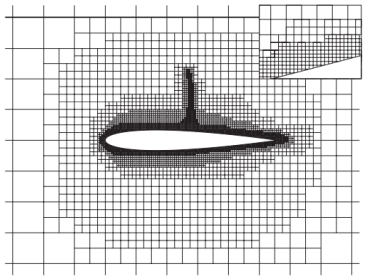

(a) Quadtree Grid (Versteeg & Malalasekera, 1995)

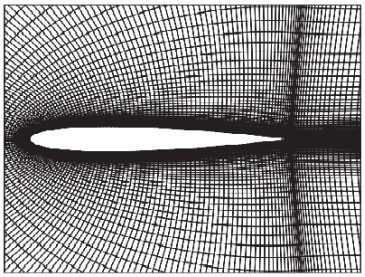

(b) Body-fitted C-type Grid (Versteeg & Malalasekera, 1995)

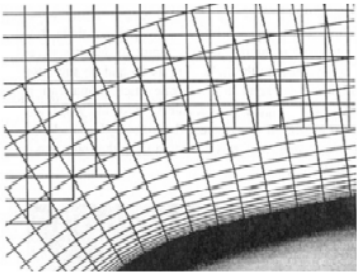

(c) Chimera Grid (Hirsch, 2009)

Figure 2.5: Different topologies for structured grids.

For arbitrary geometries and when using automatic mesh generation software, structured grids are nearly impossible to be generated, therefore, unstructured grids and flow solvers for this mesh type have gained wide acceptance. Unstructured grids offer more flexibility and local refinements are easier to implement without affecting the surroundings (Hirsch, 2009). The elements can be triangular/tetrahedral or quadrilateral/hexahedral for a 2D/3D space domain, respectively, and their enumeration is done sequentially and no indication of the local connectivity or position can be obtained based on their indices (Moukalled et al., 2015; Versteeg & Malalasekera, 1995). Various methods for generating an unstructured grid can be applied, however, grid generation techniques are beyond the scope of the presented thesis.

Fully triangular/tetrahedral grids (Figure 2.6a), while not ideal for calculating boundary layer velocity profiles, are easily generated by automatic meshers. At these locations, quadrilaterals for 2D and prisms for 3D with proper aspect ratios are more indicated, forming a hybrid unstructured mesh (Figure 2.6b) (Hirsch, 2009). Although hexahedral cells require less memory and have increased accuracy, their generation might be harder in regions with high curvature and sharp angles, generating cells with poor orthogonal quality (Moukalled et al., 2015).

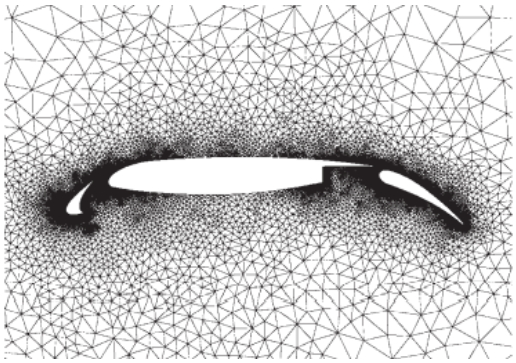

(a) Triangular Cells Grid (Versteeg & Malalasekera, 1995)

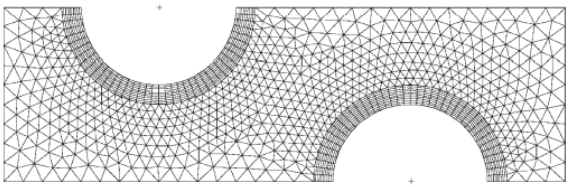

(b) Hybrid Grid (Versteeg & Malalasekera, 1995)

Figure 2.6: Different topologies for unstructured grids.

Near-Wall Treatment

The no-slip condition at the wall affects the velocity profile in its vicinity in addition to the turbulence. Close to the wall, turbulent fluctuations are reduced and viscous forces become dominant. Experimental results demonstrated that the near-wall region can be subdivided into sub-layers according to the prevalence of these phenomena (Ansys Inc., 2013). These layers exibit different dimensionless velocity profiles U^+ along its dimensionless height y^+, and this evolution is commonly displayed on a logarithmic scale (Figure 2.7). The dimensionless variables are obtained considering the velocity of the flow and the wall friction velocity u_τ, which is related to the velocity gradient near the wall, expressed in terms of the wall shear stress τ_w (Brederode, 2018).

$$U^+ = \frac{U_\infty}{u_\tau} \quad , \quad u_\tau = \sqrt{\frac{\tau_w}{\rho}} \tag{2.8a}$$

$$y^+ = \frac{u_\tau y}{\nu} \tag{2.8b}$$

Closer to the wall on the linear sub-layer, the flow is practically laminar, and viscosity effects predominate, with an exponential evolution of the velocity profile until $y^+ = 5$. The buffer layer occurs at $5 < y+ < 30 - 50$, where viscous and turbulent stresses have similar magnitudes, and then, turbulence overshadows viscosity effects in the log-law region or wall layer. At around 15% of the boundary layer displacement thickness – δ^*, at the end of the inner layer, a deviation from the low-law velocity profile occurs, with the velocity tending to its freestream value U_∞ at the end of the boundary layer (Brederode, 2018).

Due to these physical phenomena and variations in the inner boundary layer, some turbulence models are not valid in this region ($k - \epsilon$ for instance), as a result, semi-empirical wall-functions are used to resolve this boundary layer portion. Using wall functions reduces the need for a very fine refinement at the boundary layer since only one layer with $y^+ \approx 0.15\delta^*$ is required to capture the whole inner layer, thus saving computational resources (Figure 2.8). Flows characterized by high Reynolds numbers are well solved using wall functions, and the y^+ target value to be chosen for the first layer depends on the

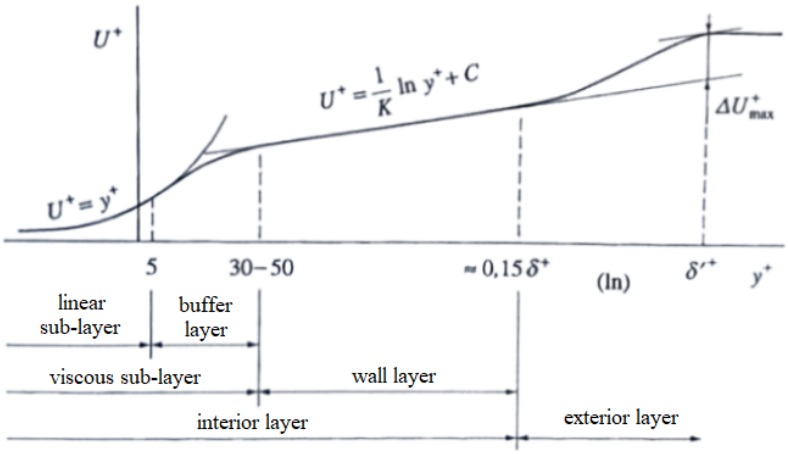

Figure 2.7: Velocity profile on a turbulent boundary layer. Adapted from Brederode (2018).

wall functions to be used: for standard wall functions, y^+ should be between 30 and 300, guaranteeing that the first cell layer contains the whole inner layer (Ansys Inc., 2013).

If separation is bound to occur or in the LRN regime, turbulence models which are valid in the viscosity-affected region should be employed. These require a much finer grid to properly resolve the viscous sub-layer (Figure 2.8), having a first grid cell with y^+ value up to 5, as proven by simulations done using the Spalart-Allmaras and $k - \omega$ models (Kalitzin, Medic, Iaccarino, & Durbin, 2005). When transition models are used, the first layer must be fine enough to capture the laminar and transitional boundary layers correctly, requiring a y^+ value lower than 1. Additionally, if laminar separation bubbles are present, special care should be given to the streamwise width of the cells, to properly represent the recirculating flow (Langtry et al., 2006; Menter et al., 2006).

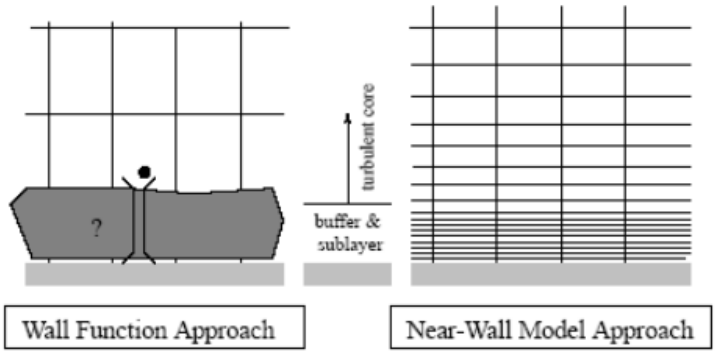

Figure 2.8: Near-wall treatments. Retrieved from Ansys Inc. (2013).

2.4.3 Discretization of Equations

Hirsch defines three methods for discretization of the space derivatives: the Finite Difference Method (FDM), the oldest and most traditional method, only applicable in structured grids; the Finite Element Method (FEM), widely used in structural analysis and also applicable in CFD with a few modifications (Hirsch, 2009); and the Finite Volume Method (FVM) which transforms the partial differential equations representing the governing laws of physics into discrete algebraic equations over finite volumes. FVM

can be applied to unstructured grids and is the most widely used method in CFD software (Moukalled et al., 2015). In the FVM, after the mesh is generated, a local control volume is associated with each mesh point and the integral conservation law is applied to it. Using the Gauss Divergence theorem transforms the control volume integrals into face fluxes which are further discretized according to the numerical schemes chosen (Moukalled et al., 2015).

The definition of the control volume in unstructured meshes has two variants: cell-centered control volumes (Figure 2.9a), with the nodes placed at the centroid of the control volumes, making the control volumes the same as the grid cells; and vertex-centered control volumes (Figure 2.9b) in which the flow variables are stored at the vertices of the grid cells and a ”new” control volume is created by linking the centroids of the grid cells or using the centroids of the grid cell faces. Although the cell-centered method is the most common (OpenFOAM, StarCCM+ and Fluent use this method), being second-order accurate and requiring less storage space since the control volumes and the grid cells are identical, non-conjunctional elements impact the accuracy of the results and non-orthogonality affects the robustness of the mesh. The vertex-centered method is used in CFX and accurately solves the face fluxes while having a lower order of accuracy. Moreover, control volumes near the grid boundaries have their centroid inside the boundary, thus complicating the discretization of the face fluxes with the walls in those cells and increasing the discretization error (Moukalled et al., 2015).

(a) Cell-Centered Control Volumes

(b) Vertex-Centered Control Volumes

Figure 2.9: Control volume construction in 2D unstructured meshes. Retrieved from Versteeg and Malalasekera (1995).

Numerical schemes are used to discretize both the temporal and spatial terms. Regarding the spatial discretization schemes, Fluent always uses second-order central-differences for computing the diffusion terms while convective terms are discretized using upwind schemes with the order of accuracy being defined by the user. While first-order upwind schemes are robust, the face value is assumed to be equal to the cell center value of the upstream cell, making it inaccurate at evaluating steep gradients. A second-order upwind scheme is more accurate since it takes into consideration the cell center value and the gradient of the upstream cell, nevertheless, this scheme may introduce undesirable non-physical oscillations. For a transient/unsteady simulation, temporal discretization is necessary, and implicit or explicit time integration is supported by Fluent with various orders of accuracy (Ansys Inc., 2013).

CFD methods can be classified into two categories according to the solver type, being density-based and pressure-based. Density-based methods were traditionally applied to transonic and supersonic

cases, while pressure-based solvers were initially restricted to low Mach numbers, yet improvements allowed their application to all flow regimes (Moukalled et al., 2015). Due to the flow regimes in which the UAV will operate, the pressure-based solver will be used throughout the presented work.

The pressure-based solver can solve the flow problem in either a segregated or coupled manner. Segregated or uncoupled algorithms have as their basis a Semi-Implicit Method for Pressure Linked Equations (SIMPLE) in which the solution is found iteratively by generating pressure and velocity fields that consecutively satisfy the momentum and continuity equations (Moukalled et al., 2015). By solving each equation separately and applying corrections to guarantee mass conservation, segregated methods converge faster and require less computational power. Fluent allows the user to choose the SIMPLE algorithm or other modifications that account for skewness and/or neighbor corrections. The coupled method solves the continuity and momentum equation together, being more robust and accurate than the segregated method while being computationally heavier. Compressible flow problems require this method to present accurate and reliable results (Ansys Inc., 2013).

Boundary conditions must be described for the boundary elements which have faces on the boundary of the domain. There are a variety of boundary conditions that can be applied and they depend on the physics of the problem: for a fluid flow simulation over a surface, a velocity inlet upstream and pressure outlet downstream are defined at the edges of the fluid domain, representing the far-field condition and undisturbed flow; wall conditions are set where the fluid domain is in contact with a solid surface and the no-slip condition is specified; and symmetry conditions can be applied in 3D simulation when the physical geometry of interest presents a mirror symmetry (Ansys Inc., 2013).

Chapter 3

Conceptual Design – Performance Considerations

The conceptual design is the initial design phase which encompasses considerations from different areas of the aeronautical spectrum and gives a general overview of the aircraft itself. As stated at the beginning of the dissertation, the conceptual design phase developed by the design team along with the methodology followed and the final solution which spurred the current thesis is published and can be consulted through reference (Alves et al., 2021).

Based on the design proposal and mission requirements, a main mission profile was defined in the conceptual phase, illustrated in Figure 3.1. The UAV would take-off vertically (1-2) and begin its transition to horizontal flight (2-3). After the VTOL system is turned off, the aircraft initiates its conventional climb phase (3-5), divided into two segments, and starts the cruise/loiter mission (5-8) upon reaching an altitude of 5000 ft. At the end of the cruise segment, the aircraft glides (8-9) and performs a landing circuit (9-10), after which the VTOL propulsion system is activated again to perform the vertical descent and landing (10-11). The vertical climb and descent phases are powered by batteries dedicated to these VTOL systems, while the forward flight segments are powered by the hydrogen fuel cell, with the aid of an additional battery to support the required power for climb and other peak power requirements. A secondary mission is also defined with take-off at a high altitude (6000 ft) and a cruise altitude of 7500 ft, with a smaller total flight time (Alves et al., 2021).

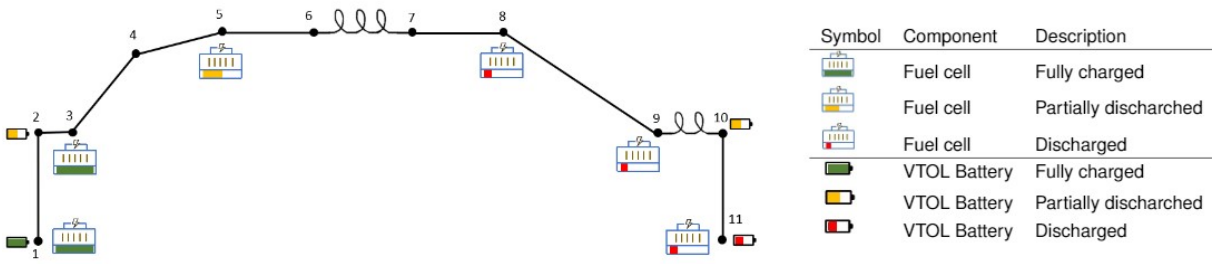

Figure 3.1: UAV mission profile. Adapted from Alves et al. (2021).

From a performance and aerodynamics point of view, flight mechanics equations were used in the conceptual phase where the aerodynamic parameters, C_{D_0} and K, are applied. These two parameters can be initially estimated based on similar aircraft (market study) or some semi-empirical formulations.

3.1 Initial Drag Estimation

For an initial estimation based on commercial and general aviation, Corke suggests a value for C_{D_0} ranging from 0.01 to 0.02 (Corke, 2003). From the market study conducted, information about the drag coefficient is not widely available on the technical sheets consulted as this information is too detailed and can be seen as classified. As such, the author based its estimates on a fixed-wing propeller UAVs database created by Coelho (2019) in his dissertation. An adaptation of Coelho's database was created – Table 3.1, narrowing the thirty-eight UAVs into those with a design similar to the one proposed in the initial design phase (Boom Mounted A-Tail and After Fuselage Mounted Engine) and with a MTOM (Maximum Take-Off Mass) of the same order of magnitude.

Table 3.1: Database of UAV with similar designs as the one projected. Adapted from Coelho (2019).

UAV	$MTOM[kg]$	$U_{cr}[m/s]$	$S_w[m^2]$	AR	C_{D_0}	C_{HT}
Aerosonde 4	15	25.72	0.567	14.75	0.014	1.23
Ogassa	36	25.72	1.06	16.64	0.022	1.02
PD-1	40	26.4	1.17	13.68	0.024	1.16
Penguin B	21.5	22	0.79	13.78	0.031	0.90

It is relevant to mention that none of the aircraft listed on the database have VTOL capabilities. Vertical flight motors and their respective propellers introduce additional drag and its contribution is relevant. Wind tunnel testing of a VTOL system, similar to the one idealized for the project, in forward flight conditions showed that the parasite drag from the vertical propellers is considerable and its relative position to the freestream has a big impact, increasing drag up to five times (for $U = 25m/s$) when the propeller is perpendicular to the airflow when compared with the optimal condition in which the propeller is parallel to the booms (Wang & Chan, 2017). These results demonstrated the importance of controlling the propeller's stopping position after its operation on the vertical flight segments.

From the values presented, the range proposed by Corke is too optimistic if applied to the design in question and even more when considering the additional drag stated above, as such C_{D_0} is considered to be 0.04 as an initial estimation.

The induced drag factor on the drag polar depends on the wing aspect ratio and the Oswald efficiency factor as stated in Equation (2.2). In an attempt to narrow the range of values given to the Oswald factor, Raymer (1992) suggests two empirical expressions for computing the Oswald efficiency factor: one of them should only be used for straight-wing aircraft and aspect ratios lower than 25, and the other for swept wings with a leading-edge sweep angle higher than 30°. Other authors such as McCormick, DATCOM and Jenkinson use additional parameters and diagrams to give better estimates, however, this process is time-consuming and some of the data is still unknown at this stage of the design process (Niţă

& Scholz, 2012). Howe's proposed equation - Equation (3.1), strikes a good balance between accuracy and input data required and takes into account the taper ratio of the wing – λ, sweep angle at 25% of the chord – $\varphi_{0.25c}$, the airfoil thickness to chord ratio – t/c, flight Mach number, and the number of engines over the wing – N_e. This approach delivers reliable results with deviations of 10% despite having the influence of the taper ratio decoupled with the sweep angle (Niţă & Scholz, 2012).

$$e = \frac{1}{(1+0.12(Ma)^2)\left(1+\frac{0.142+0.005\cdot[1+1.5\cdot(\lambda-0.6)^2]\cdot AR\cdot(10\cdot t/c)^{0.33}}{cos(\varphi_{0.25c})^2}+\frac{0.1\cdot(3\cdot N_e+1)}{(4+AR)^{0.8}}\right)} \tag{3.1}$$

At this stage, wing geometry parameters are yet to be defined. Nevertheless, at first glance, when using typical values for these variables, the Oswald efficiency values obtained using Equation (3.1) are in the range presented in subsection 2.1, as such, $e = 0.75$ is considered as an initial approximation.

3.2 Flight Speed Adjustments

As discussed in the conceptual phase of the project, the design point had little margin for error (Alves et al., 2021), with the possibility that poor initial estimations or small deviations could compromise the project since the power required for level flight cannot surpass the fuel cell's maximum power output, which for the fuel cell considered is 800 W. Hence, all the initial considerations were revised and a new iteration was done with more accuracy and inputs from the different specific areas.

From the performance point of view, the initial flight speeds considered for level flight were purely based on the range of values given on the mission proposal without much care if they were the most efficient ones. To lower the power demand during cruise, two solutions rose based on the Power (P) to Weight (W) ratio, computed using Equation (3.2), with η_{pr} being the propeller efficiency (Raymer, 1992).

$$\left(\frac{P}{W}\right)_{min} = \frac{1}{\eta_{pr}}\left[\frac{\rho U^3 C_{D_0}}{2\left(\frac{W}{S}\right)}+\frac{2K\left(\frac{W}{S}\right)}{\rho U}\right] \tag{3.2}$$

- Reduce flight speed: with the remaining parameters fixed, the higher the flight speed, the higher the power required (for the range of speeds in the design proposal). This evidence is supported by the power curve plot (Figure 3.2) in which the minimum flight speed of the design proposal (35 kts) is higher than the speed of minimum power for flying ($(C_L^{3/2}/C_D)_{max}$);
- Increase wing loading: for the range of speeds considered initially and with the remaining parameters set, the minimum power loading for level flight is achieved for higher wing loading values.

With these tendencies in mind, the objective would be to apply both solutions simultaneously and check if the final results were better than the initial ones. Reducing the flight speed is easily done since the initial values were closer to the upper bound of the flight speed interval given in the design proposal, nonetheless, for safety and operational purposes, the minimum flight speed should be at least 1.2 to 1.3 times higher than the stall one (Gundlach, 2012).

The maximum wing loading is set according to the constraints described in the design point of the conceptual design (Alves et al., 2021), most notably the stall speed and the maximum ceiling. The stall

condition, given by Equation (3.3), was initially the critical condition, so either the stall speed or the maximum lift coefficient - ($C_{L_{max}}$) must rise to increase the wing loading value. A substantial increase in the maximum lift coefficient can only be obtained using high-lift devices such as flaps (Sadrey, 2013), nevertheless, this solution would not change the wing loading for level flight conditions when the high lift devices are not in use. The strategy is then to increase the stall speed of the UAV.

The wing loading is not exclusively given by the stall condition: if the flight speed decreases, the critical condition for the wing loading might become the flight ceiling – Equation (3.4). To tackle this problem, the maximum ceiling condition is discarded, and after the analysis is done, one would check what the new maximum ceiling is and if it is feasible for the high altitude mission mentioned.

$$\left(\frac{W}{S}\right)_{stall} = \frac{1}{2}\rho U_s^2 C_{L_{max}} \qquad (3.3) \qquad \left(\frac{W}{S}\right)_{ceiling} = \frac{1}{2}\rho_{ceiling} U_{cr}^2 \sqrt{\frac{C_{D_0}}{K}} \qquad (3.4)$$

Figure 3.2 represents the power curve, given by Equation (3.2) when considering a stall speed of 28 kts. From the vertical lines, it is possible to check that the UAV cannot operate at its maximum aerodynamic efficiency flight speed – $(C_L/C_D)_{max}$. Therefore, there is no reason to consider different speeds for the cruise and the main mission segments. This graph has the same speed relationship when the stall speed is changed between 25 and 32 kts which is around the desired values.

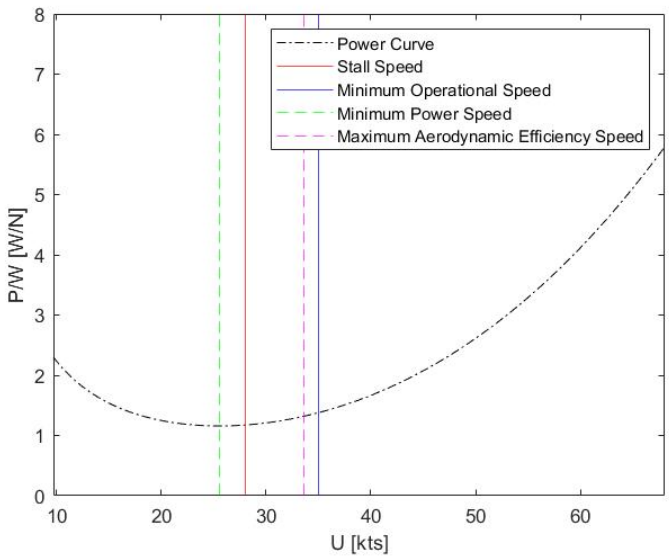

Figure 3.2: Power curve with important flight speeds.

Since the goal of this analysis was to decrease the power at level flight, an optimization study was conducted with the stall speed and cruise speed as design variables to minimize the power. The optimization problem is beyond the scope of the presented thesis and is described in detail in reference (Alves, 2021). From this study, the stall speed was set to 28 kts and the level flight to 38 kts, the latter being increased compared with the results obtained to give an extra margin for operation. With these changes, a reduction in the fuel cell power output to 670 W is achieved, well below its maximum. With the wing loading set by the stall speed constraint and the flight speed defined, the maximum ceiling is inferred to be 10000 ft, above the maximum altitude set for any of the two mission profiles.

Chapter 4

Preliminary Design

With the conceptual design finished, the preliminary design of the UAV is conducted, focused on the aerodynamics field. This design phase includes the wing and tail design as well as a more accurate estimation of the total UAV drag, to better predict the aircraft performance and serve as input for the propulsion system study. At the end of the preliminary design phase, the work developed in the structural and propulsion areas by the other members of the project is put together with the aerodynamic considerations, and an update on the UAV characteristics is done.

4.1 Wing Design

The wing should be designed in such a way that it can provide lift throughout all the flight regimes described in the mission profile while producing minimum drag. From the enhanced conceptual design phase with the motors already chosen, the wing surface area and its aspect ratio is set. The initial design phase parameters relevant for the aerodynamic study are summed up in Table 4.1.

Table 4.1: Aerodynamic related inputs from conceptual design. Adapted from Alves et al. (2021).

Parameter	Value
Wing Area	1.372 m^2
Aspect Ratio	11.66
MTOM	21.61 kg
Level Flight Speed	38 kts
Level flight Altitude	5000 ft

For the desired flight speed and altitude defined for level flight, and based on the results achieved in the initial phase (wingspan, wing area, and aspect ratio), one could calculate the expected Mach number and Reynolds number. At cruise, Mach number is 0.056, which is considered incompressible flow. Reynolds number requires a characteristic length to be computed, which for a wing corresponds to the mean chord $\overline{c}$.

4.1.1 Wing Planform

Considering the characteristics provided in subsection 2.2.2, the wing has different geometric parameters which influence its performance. With the double boom configuration chosen and bearing in mind the construction methods which are thought to be used, the wing can be divided into three panels: the middle one, which goes from one boom to the other having its midsection coincident with the aircraft symmetry plane, and the tip panels after the booms. For simplicity and structural rigidity, the mid panel has a constant chord and no sweep (straight-rectangular shape). The exact span location of the booms is still unknown and it is dependent on the tail geometry and its span. As an initial hypothesis, the rectangular central panel is initially assumed to have 0.75 m of semi-span y_B. If the booms are located further away from the symmetry plane than the assumed position, this distance has to be rethought and thus, the wing geometry redone.

To the tip panels, taper is applied to reduce the induced drag. Although the recommended taper ratio is around 0.4 to 0.45, as stated in subsection 2.2.2, for an initial geometry, taper ratio is set at 0.55 to avoid having a tip chord too small and prevent tip stall problems and structural difficulties (Sadrey, 2013). Leading edge sweep is set to 2° for aesthetic purposes, and neither dihedral nor twist are considered at this stage.

The total wingspan is easily obtained and it does not depend on the multi-panel configuration chosen. Basic geometric expressions to compute the root chord – c_r and the tip chord – c_t become more complex so that the different properties of each panel are thought out. Table 4.2 sums up the expressions used, which were adapted from Cook (2013) for a cranked wing (two panels along the semi span of the wing, each with its own taper; λ_i representing the taper ratio of the interior panel).

Table 4.2: First iteration wing dimensions.

Property	Formulation	Value [m]
Wingspan	$b = \sqrt{AR \cdot S}$	4.000
Root chord	$c_r = \frac{2 \cdot S}{2 \cdot y_B \cdot (1-\lambda) + b \cdot (\lambda + \lambda_i)}$	0.399
Tip chord	$c_t = c_r \cdot \lambda$	0.220
Mean chord	$\overline{c} = \frac{2}{3} c_r \frac{(\lambda_i^2 + \lambda_i \lambda + \lambda^2) + \left[\frac{y_B}{(b/2)-y_B}\right](1+\lambda_i+\lambda_i^2)}{(\lambda_i + \lambda) + \left[\frac{y_B}{(b/2)-y_B}\right](1+\lambda_i)}$	0.353

Figure 4.1 represents the initial geometry considered for the wing, with the leading edge being on the top part of the figure. With the mean aerodynamic chord computed and considering the Standard Atmosphere model with an offset of +20 °C (National Oceanic Atmospheric Administration, 1976), Reynolds is around 3.7×10^5 for cruise conditions.

Figure 4.1: Wing Baseline Geometry.

4.1.2 Airfoil Selection

The airfoil section is responsible for generating the optimal pressure distribution on the upper and lower wing surfaces to generate the required lift without producing excessive drag. The airfoil can be designed according to the needs or chosen from the available sources. Designing an airfoil is a complex and time-consuming process based on optimization techniques coupled with CFD aerodynamic software packages. Additionally, the airfoil design is a design project in itself, and it is just a step in the whole aircraft design process (Sadrey, 2013). For these reasons, the author opted for the second option: choosing an existing airfoil.

The University of Illinois at Urbana-Champaign (UIUC) Aerodynamics Research Laboratory produced a database (UIUC Department of Aerospace Engineering, 2020) with over 1600 airfoils to choose from among Clark, Eppler, Wortmann, Gottingen, Martin Hepperle, NACA, Selig, Selig-Ashok, Selig-Donovan, Selig-Giguere, and others.

To start the selection process, the lift coefficient at cruise must be computed. For level flight, lift is equal to the aircraft's weight, and C_L is given by Equation (4.1). Most aircraft use fossil fuel as their energy source and due to fuel consumption, they become lighter throughout the flight, reflected in a decrease of the cruise lift coefficient, therefore, an average value for C_L is usually assumed at this stage. Because the weight of hydrogen is negligible when compared to the total aircraft weight, the lift coefficient for cruise flight is assumed to be constant and equal to $C_{L_{design}} = 0.821$.

$$C_L = \frac{2W}{\rho_{cr} V_{cr}^2 S} \tag{4.1}$$

The value obtained for the cruise lift coefficient might seem high when compared with the typical ones for commercial aircraft, however, gliders and small UAVs tend to have high lift coefficients due to their relatively low cruise speed. Recalling the data from table 3.1, the previous statement is confirmed, as $C_{L_{cr}}$ for those UAV ranges between 0.78 and 1.12. In light of this, the airfoil choice was narrowed to airfoils with high lift-to-drag ratios or known to have good performance at low Reynolds numbers.

XFOIL tool from XFLR5 v6.48 was used to analyze the airfoils. A 2D direct analysis was performed for a Reynolds number of 3.7×10^5, Mach number equal to 0.056 and e^N with $N_{crit} = 9$ as the transition criteria. All airfoils are normalized using 250 panels and the study was done with the angle of attack (AoA represented by α) varying between -15°and 25°. This 2D analysis revealed that around 20 airfoils were suitable candidates, having a $C_{l_{max}}$ over 1.35, good C_l/C_d and $C_l^{3/2}/C_d$ values for the wing airfoil ideal lift coefficient – C_{l_i} and not an exaggerated C_{d_0}. The wing airfoil ideal lift coefficient is a 2D approximation of the 3D cruise lift coefficient obtained through Equation (4.2), in which the contribution to the generation of lift from all surfaces besides the wing is removed and the finite wing consideration when going from 3D to 2D is taken into account.

$$C_{l_i} = \frac{C_{L_{cr}}}{0.95 \cdot 0.9} \tag{4.2}$$

Since the wing initial geometry is already defined, 3D analysis can be conducted and their results can be used for the final choice. A fixed lift analysis was chosen, which requires 2D polars for a wide

range of Reynolds numbers. The wing was discretized into panels with a cosine distribution and the solution was obtained using the VLM considering ring vortices.

From the 20 airfoils tested in the 3D analysis, those who presented a $C_{L_{max}}$ under 1.3 were excluded since this was the value considered for the stall condition at the conceptual design phase. For the remaining, the decision criteria are based on the aerodynamic efficiency and the maximization of the endurance criteria for cruise, $C_L^{3/2}/C_D$. Table 4.3 and 4.4 list the top five airfoils, along with their 2D and 3D properties, respectively.

Table 4.3: 2D Airfoils results from XFOIL.

Airfoil	Clark Y	N-22	SD7062	SG6042	SG6043
$C_{l_{max}}$	1.42	1.55	1.62	1.51	1.66
$C_{l_\alpha}[/^\circ]$	0.0840	0.0906	0.0818	0.0744	0.0769
$\alpha_{0_l}[^\circ]$	-3.7	-5.9	-4.2	-4.5	-6.2
$\alpha_{stall}[^\circ]$	13.2	11.2	15.6	15.8	15.4
C_{d_0}	0.0119	0.0122	0.0127	0.0156	-
$C_{d_{min}}$	0.0074	0.0077	0.0088	0.0073	0.0079
$(t/c)_{max}[\%]$	11.71	12.39	14.00	10.00	10.02
$x_{(t/c)_{max}}[\%]$	28.42	27.62	27.03	34.43	32.13

Table 4.4: 3D Wing results from XFLR5, for each airfoil.

Airfoil	Clark Y	N-22	SD7062	SG6042	SG6043
$C_{L_{max}}$	1.35	1.48	1.58	1.46	1.62
$\alpha_{Stall}[^\circ]$	12.0	10.6	14.0	11.8	11.4
C_{D_0}	0.0078	0.0080	0.0086	0.0081	0.0121
For cruise conditions - $C_L = 0.821$					
$\alpha_{trim}[^\circ]$	5.86	3.60	5.20	4.37	2.13
C_D	0.0277	0.0282	0.0285	0.0263	0.0271
C_L/C_D	29.65	29.16	28.79	31.18	30.28
$C_L^{3/2}/C_D$	26.86	26.42	26.09	28.25	27.44

From the analysis results, the SG6042 airfoil was chosen (Figure 4.2), proving to have good aerodynamic efficiency at cruise while presenting a low base drag coefficient. Without incorporating the tail, the wing should be positioned with an incidence of 4.5° to provide the necessary lift at cruise conditions.

Figure 4.2: SG6042 airfoil. Adapted from Selig (1997).

4.2 Tail Design

After defining the wing initial design, the tail should be sized. The selected design for the tail is the twin-boom inverted V, supported by the literature background provided in subsection 2.2.3. The chosen layout does not have the traditional horizontal and vertical stabilizer as two different surfaces, therefore the sizing procedure is done to an equivalent horizontal and vertical tail area. Literature related to the design of an inverted V tail is scarce, consequently, the author assumes that the design steps and considerations that should be foreseen are similar to those of a single boom V-tail. For this tail layout, the dihedral angle (Γ) is the angle between the stabilizer and the horizontal plane – Equation (4.3). Additionally, the tail arm length (l_{HT}), which corresponds to the distance between the tail aerodynamic center and the wing aerodynamic center, is the same for both the equivalent vertical and horizontal tail (Gundlach, 2012).

$$\Gamma_{V-tail} = arctan\left(\frac{S_{VT}}{S_{HT}}\right) \tag{4.3}$$

The initial sizing of the equivalent horizontal tail is based on the horizontal tail volume coefficient (C_{HT}), which relates parameters of the horizontal tail with the wing (Sadrey, 2013).

$$C_{HT} = \frac{S_{HT} \cdot l_{HT}}{S \cdot \overline{c}_w} \tag{4.4}$$

Empirical values are usually used as an initial estimate for the tail volume coefficient, however, the literature gives no information on typical values for UAVs. The database from Coelho (Coelho, 2019) contains information about this coefficient, hence, it is considered as a reference. Analyzing the exhibited values, they tend to be above the ordinary ones generally used, as such, the horizontal tail coefficient is set to 0.8, lower than the ones presented.

The tail arm length, is another unknown at this point. This parameter influences the dimension of the booms and the tail area. Sadrey (Sadrey, 2013) proposes the calculation of the optimum tail arm to minimize the wet area and, consequently, drag. For this approach, the wet area of the booms should be given as a function of the tail arm length. Without the boom geometry defined, specifically the boom cross-section, this method becomes impracticable.

A simpler solution proposed by Corke (2003) is to give a reasonable value for the tail arm length and infer the tail surface area from it. To choose a proper value for the tail arm length, a ratio between this variable and the UAV total length was considered – $\left(\frac{l_T}{l_{total}}\right)$. From the database and analysis made by Coelho (2019), this ratio is between 0.4 and 0.6 for UAVs with an aft fuselage mounted engine (pusher configuration). Looking from a lateral perspective on a twin-boom aircraft, its total length can be divided into segments according to Equation (4.5):

$$l_{total} = l_{fuselage} - (0.75 \cdot \overline{c}_W + l_{TE\ to\ fus-end}) + l_T + 0.75 \cdot \overline{c}_T \tag{4.5}$$

An embryonic design of the main fuselage was conducted, considering all the components the main fuselage has to carry and their allocation. The details of this design are depicted in the structural analysis

oriented dissertation, yielding a total length for the main fuselage of $1.4\ m$ (Sá, 2021).

$(l_{TE\ to\ fus-end})$ is the distance between the trailing edge of the wing and the rear of the main fuselage. On a twin-boom configuration, the wing is located close to the rear of the main fuselage, therefore, its length is much smaller compared with the remainder of the fuselage. At this stage, the tail mean chord is yet to be determined, however, this value will be lower than the mean chord of the wing. With these two variables still unknown, they are ignored as a first approximation, and the tail arm is fixed at $1.5m$.

Applying Equation 4.4 gives an equivalent horizontal tail area of $0.258m^2$. Equation 4.3 defines the dihedral angle, which is set to 45°, similar to the UAVs presented in the database. This dihedral angle defines an equivalent vertical tail area equal to the horizontal one.

At first glance, the theoretical area for the complete tail is $S_T = \sqrt{S_{HT}^2 + S_{VT}^2}$ due to simple geometric analysis, making a V-tail area 70.7% of a conventional one. Nonetheless, according to Pursee and Campbell (1944); Stettmaier (1999), the tail has to be larger to have the same efficiency, as such this area reduction does not exist and, consequently, $S_T = S_{HT} + S_{VT}$.

From the market study conducted for this tail configuration, it was concluded that each tail half has an aspect ratio of 4 which is in agreement with the bibliography for conventional tails. Moreover, neither sweep nor taper are usually applied on inverted V tails. Considering this aspect ratio for each half, the tail has a projected aspect ratio of 5.66 when viewed from above, resulting in a projected semi-span of $0.716\ m$ and thus making the wing geometry initially considered feasible. Since each tail panel is rectangular, the tail chord is constant yielding $\bar{c}_T = 0.255\ m$.

The airfoil selection for the tail has different criteria than the wing. Concerning the tail, the airfoil should be symmetrical to either create positive or negative lift and have a low base drag (Sadrey, 2013). Because the tail airfoil should have a lower thickness to chord ratio than the wing, NACA 0008 is selected. At this stage, the lift force produced by the tail to trim the aircraft cannot be computed since the location of the CG is yet unknown.

4.3 Drag Build-Up

The total aircraft drag is the sum of each component contribution. Every component exposed to the airflow produces parasite drag, and the wing is the main generator of lift induced drag (Anderson, 2012).

4.3.1 Lift Producing Surfaces

Regarding the wing, both drag components can be calculated using empirical formulations. For the induced drag components, Howe's approximation for the Oswald efficiency factor – Equation (3.1) can be applied for the wing geometry defined, yielding $e = 0.7435$, which is very close to the initial estimate, making $C_{D_i} = 0.0247$ for cruise. With the tail having no incidence, no lift is expected to be produced and, therefore, no contribution to the induced drag coefficient.

For the parasite drag, Hoerner proposes using Equation (4.6) which makes an analogy with the flat

plate. S_{wet} represents the area of the component exposed to the airflow, Q the interference factor, C_f the flat plate average skin coefficient and FF the form factor. The interference factor accounts for the interaction between two surfaces which increases the boundary layer thickness near the interaction region, causing additional drag. The skin friction coefficient is highly dependent on the boundary layer structure, whether it is laminar or turbulent. Form Factor makes the flat plate correction to the actual geometry and takes into account the pressure drag caused by flow separation (Raymer, 1992).

$$C_{D_0} = \frac{S_{wet}}{S_{ref}} \cdot Q \cdot C_f \cdot FF \tag{4.6}$$

According to Roskam and Lan (2016), $Q_{wing} = 1$ for a high-wing, and $Q_{tail} = 1.08$ for a double boom tail configuration. Concerning the skin friction coefficient, it is influenced by the location of the transition from laminar to turbulent flow. The transition point depends on the angle of attack, which varies during flight. Raymer (1992) suggests assuming the transition to occur near the maximum thickness point of the airfoil. With the transition point defined, Equation (4.7) can be applied to give a better estimate of the skin friction coefficient. The partial skin friction coefficients in this formula are calculated using the wing characteristic Reynolds number times the percentage of laminar flow. For laminar flow, Blasius solution is applied and for turbulent flow, the author opts to choose Schlichting formulation for the skin-friction parameter. Since XFLR5 provides information on the transition location for the 3D wing, this information will be considered for a better estimate. At an incidence of $4.5°$, transition occurs at around 65% of the chord on the upper surface, much later than Raymer suggests. XFLR5 predicts fully laminar flow in the tail, with transition occurring very close to the trailing edge at high tail AoA, implying that 90% of the tail is always in the laminar regime.

$$C_f = C_{f(100\%Turb)} - (C_{f(\%PartialTurb)} \cdot \%Lam) + (C_{f(\%PartialLam)} \cdot \%Lam) \tag{4.7}$$

Several authors suggest different estimations for the form factor. Hoerner (1965) introduces a simple empirical expression – Equation (4.8) – as a function of the wing thickness-to-chord ratio, valid for incompressible flow.

$$FF = 1 + 2\,(t/c) + 60\,(t/c)^4 \tag{4.8}$$

Modeling the wing and the tail on OpenVSP and considering the empirical expression displayed above, yields $C_{D_{0\ wing}} = 0.00785$ and $C_{D_{0\ tail}} = 0.00265$. The results obtained in OpenVSP are similar to the ones obtained using XFLR5, with differences below 5%.

4.3.2 Fuselage and other Structures

Equation (4.6) is also valid for slender bodies, thus, it can be applied to the main central body and the tail booms. For these bodies, the $Q = 1$. Skin friction and the wet area are computed by dividing the surface into segments of constant length and considering each segment Reynolds number, which uses its position from the start of the fuselage as the characteristic length. Without information on the

transition location, the boundary layer is assumed fully turbulent as the worst-case scenario.

The form factor is given as a function of the fineness ratio, corresponding to the length to diameter ratio of the body. Following the same reference, Hoerner (1965) proposes Equation (4.9) to calculate the form factor of streamlined bodies.

$$FF = 1 + \frac{1.5}{(l/d)^{1.5}} + \frac{7}{(l/d)^3} \tag{4.9}$$

Similar to the lifting surfaces, the fuselage and the booms were added to the model on OpenVSP, resulting in a $C_{D_{0\ booms}} = 0.00181$ for both booms and $C_{D_{0\ body}} = 0.00336$.

The drag build-up must also account for other structures in contact with the external airflow, such as the landing gear (struts and wheels) and the daylight camera. The contribution of these components is estimated at the early stages by using the characteristic drag coefficient based on the component's shape and form, and its frontal surface area S_f – Equation (4.10). In $C_{d_{component}}$ the lower case subscript d does not stand for 2D coefficients, instead, it is related with the data gathered from the literature, which is the result of experimental testing. Because the experimental results do not distinguish between parasite and induced drag (Hoerner, 1965), the nomenclature used with these empirical coefficients does not include the subscript $_0$. This change is used in order to distinguish it from C_D which already accounts for the surface area of the component as seen on Equation (4.10).

$$C_{D_{component}} = C_{d_{component}} \frac{S_{f_{component}}}{S_{ref}} \tag{4.10}$$

The landing gear has a tricycle gear configuration in which the main gear is located after the CG, supporting most of the aircraft's weight. The nose gear is composed of a "double" wheel and a single strut, while the main gear has two wheels equidistant to the symmetry plane and an arc-shaped carbon fiber strut (Sadrey, 2013). At this stage of the design phase, the dimensions of the landing gear are still unknown and hard to get, as such, UAVs at CIAFA with a similar MTOM serve as a reference for both landing gear (strut and wheels): the nose gear is based on Alpha Extended 1 – Figure 4.3a – while the main gear is from a real manufactured piece designed for a 30 kg UAV – Figure 4.3b. For non fairing struts, $C_{d_{strut}} = 1$ while for wheels, $C_{d_{wheel}} = 0.3$ (Hoerner, 1965; Sadrey, 2013). With the frontal area measured, the nose gear strut and its "double" wheel yields $C_{D_{NoseGear}} = 0.00256$, and the main gear $C_{D_{MainGear}} = 0.00296$

The camera has a belly pan-tilt integration on the fuselage, making the optical camera sphere fully in contact with the airflow, therefore the external surface can be approximated as a sphere and its parasite drag contribution can be estimated by Equation (4.10) (Gundlach, 2012). Considering the TASE 150 model as reference, with a diameter of 0.112 m (UTC Aerospace Technology, 2015), and a $C_{d_{sphere}} = 0.41$ for a sphere under Reynolds number below 4×10^5, the camera drag coefficient yields $C_{D_{Camera}} = 0.00294$.

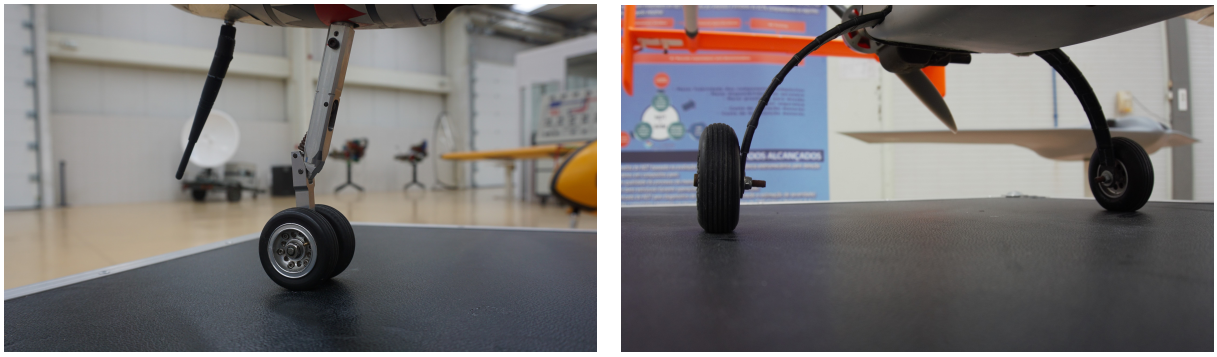

(a) Nose Gear (b) Main Gear

Figure 4.3: Nose and main gear of similar MTOM aircraft in CIAFA.

4.3.3 VTOL Propulsion System

As stated in section 3.1, the VTOL propulsion system has a big impact on the total aircraft drag at cruise. For the drag build-up process, only the components in contact with the freestream are important, namely the motor and the rotor. For the sake of clarity, the author uses the word ”rotor” to mention the propeller which provides vertical thrust, with the term ”propeller” used solely for the one which provides forward thrust, like on a conventional propeller-driven airplane.

Empirical expressions for the motor consider a blunt body and for the propeller an equivalent flat plate. These expressions failed to accurately predict the parasitic drag on a similar Lift+Cruise UAV design project, as such they should be used with care and validated with experimental data (Wang & Chan, 2017).

In a previous design project done by the AFA, Mendes (Mendes, 2021) conducted a wind tunnel experiment to obtain the drag of a P-60 motor by T-Motor with a 22x6.6 rotor attached to it, subjected to atmospheric conditions with a freestream flow velocity of 20 m/s. Table 4.5 summarizes the obtained results. It is important to note that the data is exclusively related to the motor and rotor since the scale bench was calibrated to not include the drag of the structure supporting the components. Furthermore, the rotor remained stationary during the whole experiment.

Table 4.5: wind tunnel data obtained by Mendes. Adapted from Mendes (2021).

	Single motor and rotor	Rear and forward motor and rotor
Drag with rotor parallel to boom	0.808 N	1.30 N
Drag with rotor perpendicular to boom	1.52 N	2.54 N

Looking at the results, the drag created by these components can almost double depending on the stopping position of the rotor, reinforcing the necessity and the advantage of creating a mechanism to stop the rotor when they are parallel to the boom if it does not create more drag than the worst-case scenario. Although the tested conditions are not the same as the cruise conditions of this project, neither are the components tested, they are very similar. Additionally, the experiment with both rear and forward VTOL systems installed has an increase by around 65% in the drag force when compared to each individual contribution, which is less than two sets separated, indicating that the wake of the front VTOL

system interacts with the rear components, reducing the drag produced by the latter.

Without additional data from wind tunnel tests with different components and freestream conditions, these results cannot be used and scale them to the project requirements. Nevertheless, the author can compare them with empirical expressions and subsequently apply these expressions to the project's conditions and components.

Recalling Equation (4.10), Hoerner defines the $C_{d_{motor}} = 1.2$ for cylindrical bodies without any fairing, which is the case of the motor. The frontal area corresponds to the length times the diameter of the motor (Hoerner, 1965).

Regarding the rotor, Hoerner (1965) considers $C_{d_{propeller}} = 0.1 + cos^2\beta_{0.7r}$, where $\beta_{0.7r}$ is the angle between the chord at 0.7 of the blade radius and the rotation plane. Since this expression is applied to stopped propellers providing forward thrust, $\beta_{0.7r} = 0°$ corresponds to the blades with their surface almost fully perpendicular to the incoming free stream, thus creating more drag as predicted by the previous expression. When the rotating plane is horizontal, which is the case for the rotor on a fully VTOL system at hover, $\beta_{0.7r} = 90°$ would have the same interaction between the blades and the freestream as the previous case. To keep the same definition for $\beta_{0.7r}$, the expression applied to rotors should be changed to $C_{d_{rotor}} = 0.1 + sin^2\beta_{0.7r}$. The surface area to be considered is cumbersome to compute due to the shape of the rotor blades, as such a simplification is used which multiplies the rotor diameter with the chord at 0.7 of the blade radius.

Using the geometry data from the motor and rotor from the supplier (T-Motor, 2021) of the components tested by Mendes (2021), and calculating the drag force using Equation (4.10) yields a $D_{Motor} = 0.6796N$ and $D_{Rotor} = 0.7852N$. When summing up these contributions and not considering any interference of these components with the structure, the drag produced by a single VTOL system set is $1.465N$. Compared to the case where a single rotor is perpendicular to the boom, the empirical expressions are off by less than 5% which validates the use of empirical expressions to get, at least, an order of magnitude of the parasitic drag produced by the VTOL system. The ideal stopping position of the rotors cannot be computed using the previously mentioned expressions since a conventional propeller never has the same relative position to the freestream as this position for the rotor. A flat plate analogy to the rotor at this position was discarded as it heavily underestimated the drag produced by this component.

(a) V605 KV210 VTOL motor

(b) V22x7.4R VTOL rotor

Figure 4.4: VTOL propulsion system components. Retrieved from T-Motor (2021).

For the V605 motor to be used (Figure 4.4a), T-Motor (2021) provides the dimensions of the motor in question, yielding a $C_{D_{Motor}} = 0.00217$. The rotor – Figure 4.4b – has a $16°$ for $\beta_{0.7r}$, resulting in $C_{d_{rotor}} = 0.17598$. With a chord of $41.2mm$ at 70% of the radius and knowing the rotor diameter, $C_{D_{Rotor}} = 0.00295$ when it is perpendicular to the freestream. A single VTOL set with the rotor perpendicular to the freestream presents $C_{D_{SingleVTOL}} = 0.00512$. To assess the drag of both front and rear VTOL sets and for both booms, the percentages obtained from the experimental data mentioned at the beginning of the subsection are applied, yielding a $C_{D_{perpendicularVTOL}} = 0.01690$ as the worst case scenario and approximately half as the best case scenario, with $C_{D_{parallelVTOL}} = 0.00845$.

4.4 Preliminary Characteristics of the UAV

With the preliminary phase finished, the author's aerodynamics considerations are put together with the remaining areas covered by the design team and the UAV general characteristics are updated. Since a lot of thought was put into the initial conceptual phase and a conservative approach was taken when faced with uncertainties, there were no noteworthy changes after the preliminary design phase, which validates the concept created. In each respective area, Sá (2021) developed the UAV V-n diagram, conducted an in-depth weight analysis with all the components to be used, calculating the CG, as well as estimates for each structural element, taking into account the the properties of the materials to be used in a future construction phase. Additionally, an initial wing structure was thought out for the wing described in section 4.1. Regarding the propulsion systems, P. Silva (2021) justified the choice of the V605 motor with the 22x7.4 T-Motor rotor to be used in the VTOL system based on the supplier's data as well as the forward motor with possible propellers to be applied.

4.4.1 Static Stability Analysis

With the CG location defined and an update to the total weight of the UAV, XFLR5 is used to conduct a simple longitudinal static stability analysis. Because of the increased MTOM, $C_{L_{cruise}} = 0.827$ and the wing incidence must be increased to $4.9°$.

With the wing and tail implemented in XFLR5, the analysis showed that the moment around the CG is small at cruise conditions, easily nullified by a small upward deflection of both ruddervators. The static margin provided by XFLR5 is around 50% , which is considered excessive even for low-maneuvrable aircraft. This effect is due to having a "heavy tail" design and a high initial tail volume coefficient. Nevertheless, the value considered was slightly lower than the ones provided in Table 3.1. While a stability analysis is not the primary focus of the current dissertation, it is important to guarantee that the designed aircraft is stable and not too rigid and hard to maneuver.

In an attempt to understand the incongruities between the results obtained and the similar UAVs over which the project is based, Ogassa and Penguin-B from Table 3.1 were modeled in XFLR5 with the information available (UAV Factory, 2021; UAVision, 2020, 2021). The results showed that for a similar modeling approach as the one used for the tail design, the static margin of these UAVs was also over

50%. Since these UAVs are real-world and operable aircraft, the author considers that following the trends and properties of these UAVs outweighs the results obtained from the low fidelity software (regarding the static margin) and no reduction to the tail arm nor to the tail size is considered. Additionally, a higher static margin than usual allows more flexibility for the location of the CG, and since the static margin is a percentage of the wing's mean chord, this CG location range is translated into just a few centimeters.

Another basic concern related to the tail and longitudinal control surface is the ability to trim the aircraft in cruise conditions and in more aggressive attitudes such as stall. The ruddervators occupy around 60% of each half-tail span, and the hinge is located at 80% of the tail chord. At stall conditions, trim is achieved by deflecting both ruddervators upwards by $8°$.

4.4.2 Performance Update

From the drag build-up procedure in section 4.3, the UAV yields a parasitic drag coefficient between 0.03258 and 0.04103 depending on the stopping position of the rotors, which corroborates the good initial estimate of 0.04 given at the early stages of the design phase. Recalling the information featured in subsection 4.3.1 regarding the induced drag component, $e = 0.7435$ when considering the wing structure defined.

With the previous two parameters computed and assuming a drag polar in the form of Equation (2.2), the thrust – T and power required for cruise and climb are given by Equation (4.11) and Equation (4.12), in which RoC represents the rate of climb of the aircraft (Raymer, 1992). The obtained values are summarized in Table 4.6. It is important to note that the power required during cruise, which includes the required shaft power, efficiency of the forward motor and ESC (Electronic Speed Controller), η_{motor} and η_{ESC}, and power consumption by the payload and primary systems (P_{PPS} = 80 W), is still below the 800 W fuel cell maximum output which does not jeopardize the entire project. Additionally, the propulsion system study done by Silva verified that the forward motor and propeller chosen can output the required thrust for the conventional climb phase at an acceptable range of RPM (rotations per minute) and below the motor's 100% throttle (P. Silva, 2021).

$$T = \frac{RoC\ W}{U} + \frac{\rho U^2 S C_{D_0}}{2} + \frac{2KW^2}{\rho U^2 S} \qquad (4.11)$$

$$P = \frac{TU}{\eta_{pr}} \qquad (4.12)$$

From the conceptual design phase, it was determined that around 70% of the total hydrogen in the tank is available to be used during cruise – $(m_{H2\ cr}/m_{H2\ tot})$, with the remaining being consumed during climb (11.9%), descent and landing circuit (6.2%), battery recharge (6.8%), and a small percentage kept as reserve (5%). Additionally, for the flight speeds defined for the VTOL segments, climb, descent and landing circuit phase, they sum up to a total of 50 min of flight time, with the cruise segment varying according to the hydrogen mass available and power requirement. The cruise flight time, in hours, is obtain through Equation 4.13 in which η_{FC} is the fuel cell efficiency at cruise (Raymer, 1992).

$$t_{cr} = \frac{\eta_{FC}}{\frac{P_{cr}}{\eta_{motor}\eta_{ESC}} + P_{PPS}} \cdot E^*_{H2} \cdot m_{H2\ tot} \cdot (m_{H2\ cr}/m_{H2\ tot}) \tag{4.13}$$

$$m_{H2\ tot} = 0.1485\ kg \qquad \eta_{motor} = 0.90 \qquad \eta_{ESC} = 0.95 \qquad (P.\ Silva,\ 2021)$$

$$\eta_{FC} = 0.52 \qquad E^*_{H2} = 33.3\ Wh/kg \qquad (IntelligentEnergy,\ 2021)$$

Updating the Oswald efficiency factor and the parasite drag coefficient into the design tool created in the conceptual phase resulted in an estimated total flight time of 3h25 min, above the minimum required in the design proposal. With the update on the UAV characteristics done, the preliminary design phase of the project is finished. Figure 4.5 displays a CAD model done in OpenVSP with the UAV designed at this stage of the design process.

Table 4.6: UAV general characteristics.

Weights		Wing		Tail	
MTOM	21.77 kg	Aspect Ratio	11.66	Total Area	0.516 m^2
Structural	6.11 kg	Area	1.372 m^2	Dihedral	45°
Propulsion	2.62 kg	Span	4 m	Arm	1.4 m
H2 System	4.48 kg	Taper at the Tip	0.55	Chord	0.255 m
Energy	2.91 kg	Mean Chord	0.353 m	Airfoil	NACA0008
CG Location	875 mm from nose	Airfoil	SG6042		
VTOL Prop System		**Forward Prop System**		**Performance**	
Motor	V605	Motor	AT5220	Stall Speed	28 kts
Rotor	T-Motor 22x7.4	Propeller	APC 20x10	Max ceiling	10000ft
P Hover	858.07 W	η_{pr}	0.65	Cruise Speed	38 kts
P max	3182.62 W	P cruise	513.6 W	Climb Speed	36 kts
RPM Hover	4734	P climb	1149 W	Climb Angle	6.2°
RPM max	7036	T cruise	17.08 N	Cruise Altitude	5000ft
		T climb	40.34 N	Flight time	3h25

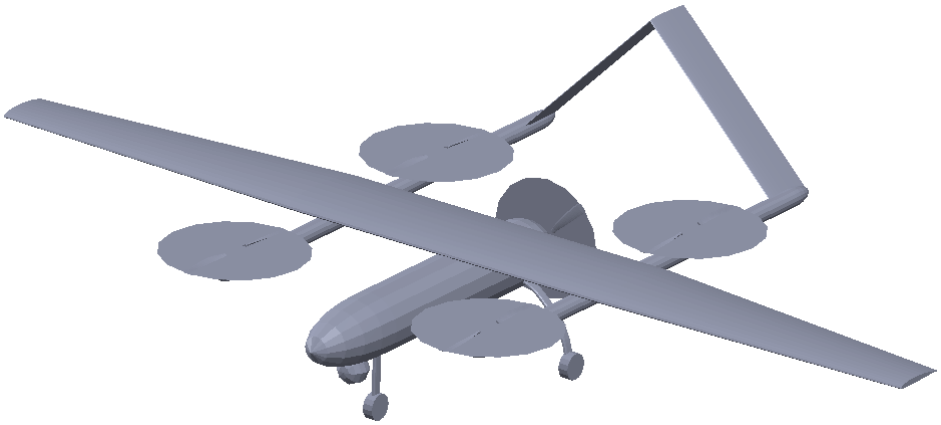

Figure 4.5: Preliminary CAD model of the UAV. Retrieved from Alves et al. (2021).

Chapter 5

CFD Validation

To validate the turbulence model to be used for the 3D wing and the aircraft, a 2D analysis was performed considering the airfoil chosen at the preliminary design phase – SG6042. Initially, a mesh convergence study is done and simulations applying the various turbulence models are run. Results from experimental data and the low-fidelity software are compared, together with considerations featured in the literature review.

5.1 Experimental Data and XFOIL Results

Together with its database, UIUC, along with Selig (1997), contains data related to the wind tunnel testing of the chosen airfoil at various Reynolds numbers, ranging from 1×10^5 to 5×10^5. The results for a $Re = 4 \times 10^5$ were used since its the closest regime to the author's case. To replicate the experimental results with the highest level of detail as possible, the simulation conditions for the low-fidelity software and for Fluent are the same as the testing one: the airfoil chord is 12 in – 0.3048 m, a freestream velocity of 19.41 m/s, air has Sea-level properties according to the Standard Atmosphere, and turbulent intensity is kept around 0.1%, important for simulations using Fluent as this is a required inlet condition. The conditions are specified on the experimental data in Selig (1997). The experimental data regarding the lift and drag coefficients was interpolated for integer AoA between -4° and 12° to be compared afterward with the software simulations.

For the low-fidelity software, XFOIL was employed. A 2D direct analysis was conducted for the test Reynolds Number, a Mach number equal to 0.057, and considering e^N as the transition criteria with $N_{crit} = 9$. The airfoil was discretized into 250 panels and tested for the same range of AoA as the experimental data.

5.2 Fluent Considerations

Ansys enables the user to create a Fluent project from scratch and divides it into consecutive steps. These steps are in agreement with the schematic presented in Figure 2.4, where a CAD model is created

together with the fluid domain, followed by the mesh generation, and culminating in the CFD simulation on Fluent where the model equations, boundary conditions, and solver properties are set. To avoid compatibility issues, the in-built Ansys CAD software - DesignModeler and automatic mesh generator were used.

The methodology to be used for CFD simulations is determined by several factors, including the application cases, flow regimes, and objects of study. Veríssimo (2016) features a set of Best Practice Guidelines for CFD applied to UAVs. In his study, he validated the methodology to be employed for UAVs in the LRN regime, which is the case of the presented dissertation. Although Veríssimo's guide was designed for Star-CCM+, most of the methodology can be replicated in Ansys Fluent and the Fluent User Manual (Ansys Inc., 2013) serves as confirmation and additional insight.

5.2.1 Physical Modeling and Grid Generation

Following the methodology stated before, a 2D CAD model was produced containing the airfoil and domain surrounding it. The SG6042 airfoil coordinates, retrieved from Selig (1997), were imported to the CAD software, however, the airfoil's sharp trailing edge was creating issues during the meshing process: the inflation at the trailing edge was being poorly generated, creating elements with unacceptable values for their orthogonal quality. To address this problem, the trailing edge was slightly cut and replaced with a straight vertical one with a thickness of less than 1 mm. The global control volume was built according to the airfoil chord length, creating a C-shape being at least 60 chords away from the airfoil in all directions.

The wind tunnel test conditions are replicated in the CFD simulation. For the freestream velocity considered, incompressible flow is assumed, which makes the constant density assumption valid, thus disregarding the use of the energy equation. The turbulence models to be considered are the ones stated in subsection 2.4.1 with transition criteria, if applicable.

To simulate various AoA in the CFD software, two possibilities can be considered: rotating the airfoil to the desired AoA or introducing a vertical component to the freestream velocity. The former option better simulates the real conditions in terms of freestream orientation, although it requires an update to the CAD model and consequently a new mesh generation. The latter requires changes in the direction of the velocity inlet and pressure outlet freestream and in the force direction to be read for computing the lift and drag coefficients. From the two options, the second one is preferred since no additional computational time is required in re-meshing and the changes in the simulation and report definitions are easily parameterized. One additional concern when choosing this AoA variation method is to also consider the top and bottom horizontal boundaries as velocity inlets.

Apart from the freestream intensity (velocity magnitude) and direction, the turbulence intensity and viscosity ratio need to be set. Turbulence intensity is set to 0.1%, the same as the wind tunnel, and viscosity ratio to 1 according to Veríssimo's Best Practices (Veríssimo, 2016) for both velocity inlet and pressure outlet. The no-slip condition is set to the airfoil surface and the fluid domain properties are defined according to the wind tunnel conditions in section 5.1.

For the mesh generation, the author considers three topics of relevance: general properties, local

refinements, and wall treatment. The considered mesh is unstructured with triangular cells with an inflation layer around the airfoil. The cell base size is set, limiting the maximum cell dimensions far away from the airfoil. A slow growth rate of 1.05 is applied and the smoothing is set to high to improve the quality of the elements at the cost of a slight increase in the mesh generation time (Ansys Inc., 2010).

To refine the region near the airfoil, a discrete number of divisions were set on the upper and lower surfaces of the airfoil. A bias type was applied to this edge sizing, making the regions near the leading edge and the trailing edge smaller than in the middle. To be concise in the mesh convergence study, only the number of divisions was changed, keeping the bias factor constant at 20 – ratio between the smallest edge division and the largest (Ansys Inc., 2010). Furthermore, a circular region centered on the trailing edge of the airfoil with a radius of 0.5 m (1.64 times bigger than the chord) was refined to capture the pressure gradients which are larger in the vicinity of the airfoil, as well as the major portion of the airfoil wake and separation if it occurs.

Special care is taken into consideration in the region near the airfoil where the boundary layer is developed. To capture the BL evolution with accuracy, a structured grid is applied, denominated as the inflation layer in Ansys Fluent.

The inflation layer thickness should be high enough to capture the whole BL, as such Prandtl's expression – Equation (5.1) for a fully turbulent boundary layer is applied to give an estimate of the maximum boundary layer thickness – δ and thus the total height of the inflation layer (Schlichting, 1979). Although the boundary layer is expected to have a considerable portion of laminar flow, applying Equation (5.1) assumes the highest thickness possible, guaranteeing that all the BL phenomena are captured.

$$\delta = 0.37 Re^{-0.2} \bar{c} \tag{5.1}$$

As stated in subsection 2.4.2, the first layer height of the inflation layer – y_1 – needs to be properly set depending on the turbulence model to be applied. Equation (5.2) defines y_1 according to the target y^+ and considers the friction velocity as a function of the friction coefficient, given by an empirical expression from Prandtl-Schlichting valid for Reynolds numbers below 10^9 (Schlichting, 1979).

$$y_1 = \frac{y^+_{target}\mu}{\rho u_\tau} \quad , \; with \quad u_\tau = \sqrt{\frac{1}{2} C_f U^2_\infty} \quad and \quad C_f = [2 \, \log_{10}(Re) - 0.65]^{-2.3} \tag{5.2}$$

To fully define the inflation layer in Ansys with the properties stated above, a first layer height control is used where the y_1 value, the total number of layers and the growth rate must be specified. The growth rate defines the thickness of the next layer relative to the previous one, and it is set to 1.2, the default value (Ansys Inc., 2010). The inflation layer height follows a geometric series where the first term and the growth ratio are set, with the number of layers inferred, as the sum of all the layers must be close to the total boundary layer thickness previously calculated.

Given the wind tunnel test conditions, the maximum thickness of the boundary layer is estimated to be $1 \times 10^{-2} \; m$. Since all the turbulence models applied are capable of modeling the viscous sublayer except the $k - \epsilon$ model, $y^+_{target} = 1$. However after some simulations, the leading edge of the airfoil was presenting values for y^+ around 2, therefore the first layer height was reduced by half from the value

obtained through Equation (5.2) and y_1 was set to $8 \times 10^{-6}\ m$; 30 layers were considered to capture the whole boundary layer. For the $k-\epsilon$ model, $y_1 = 8 \times 10^{-4}\ m$ for a $y^+_{target} = 50$ and 7 layers were defined.

Figure 5.1 shows the airfoil surrounding mesh where the circular region with a smaller refinement is visible, together with a detail of the 30 layer inflation adjacent to the airfoil surface, in which it is also possible to visualize the effect of the bias factor applied to the airfoil division.

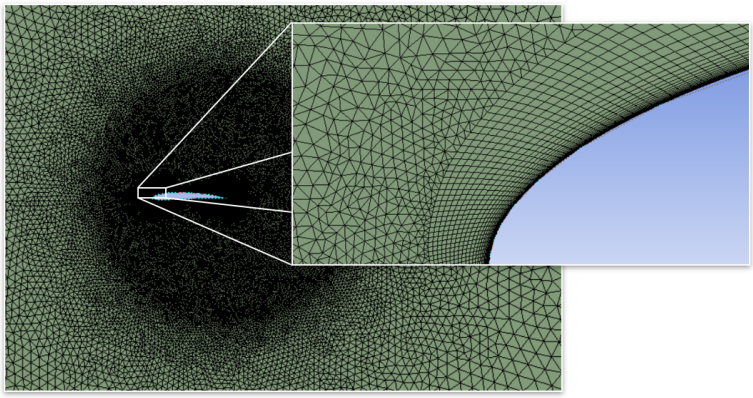

Figure 5.1: 2D Mesh with the detail on the inflation layer.

5.2.2 2D Mesh Convergence Study

With the local refinements considered in the mesh generation, a grid convergence study was conducted. A coarser mesh is generated first, and for subsequent grids, a percentage ratio is defined and applied to keep the base cell size, the local refinement near the airfoil, and the number of elements in the upper and lower surface concise across all grids generated, while the trailing edge divisions and the inflation layer were kept constant to guarantee that $y^+ < 1$ for the first layer. Four meshes were created, the coarser having 57k and the finer 213k elements. This study was performed for an AoA of 12° near stall conditions and considering the recommended turbulence model – the Transition SST, since this model is the most complex one and requires more computational effort.

The airfoil 2D lift and drag coefficient were the variables of interest for the mesh convergence study, and the results are plotted in Figure 5.2. The solution is said to be converged whenever the residuals drop by at least 3 decimal cases and no significant variations occur between iterations on the variables of interest. Both lift and drag coefficients vary less than 0.5% from the mesh with 92k elements to the one with 146k, thus making the 92k elements mesh the one to be used in future 2D analysis. Details of the mesh to be considered for future simulations are shown on Table 5.1.

Table 5.1: 2D 91k mesh parameters.

Parameter	Value
Base Cell Size	$3.75\ m$
Number of divisions of the upper/lower surface	200
Number of divisions of the trailing edge	7
Sphere of influence Cell Size	$7.5 \times 10^{-3}\ m$

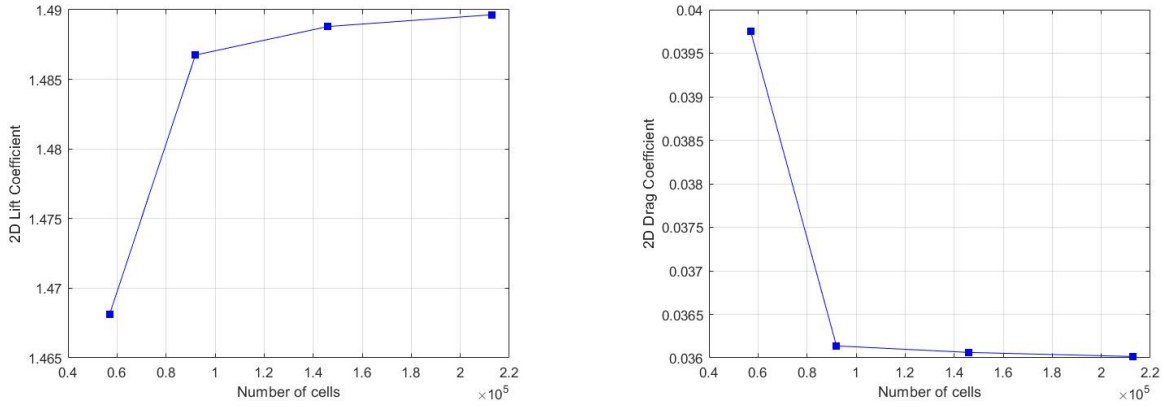

(a) C_l evolution

(b) C_d evolution

Figure 5.2: 2D Mesh convergence study.

For the mesh to be used with the turbulence models that require near-wall functions, the $k-\epsilon$ model, a similar grid convergence study was conducted. The conclusions are similar to the previous case, with the chosen mesh having 86k elements with the same refinements and properties listed in Table 5.1.

5.2.3 Turbulence Model Validation

The turbulence models considered for the 2D simulations are described in subsection 2.4.1. The $k-\epsilon$ Realizable model is used, which is a modification of the base model recommended for boundary layers under strong adverse pressure gradients, separation, and recirculation. For the SST model, Fluent incorporates a low Reynolds number correction which will be applied (Ansys Inc., 2013). Simulations for an AoA of 0° and 4° (Table 5.2) were run and compared to the experimental UIUC data and to XFOIL, as well as for the highest AoA with experimental data available – 12° (Table 5.3).

Table 5.2: Comparison between experimental, XFOIL and Fluent results for AoA of 0 and 4 degrees.

	AoA = 0°				AoA = 4°			
	Cl	Cd	% Cl	% Cd	Cl	Cd	% Cl	% Cd
Experimental	0.4923	0.0077			0.9122	0.0091		
XFOIL	0.5155	0.0073	4.73%	-5.16%	0.9397	0.0082	3.01%	-9.44%
SA	0.4938	0.0133	0.31%	74.07%	0.9180	0.0158	0.64%	74.21%
$k-\epsilon$ Realizable	0.4889	0.0153	-0.68%	99.38%	0.9091	0.0182	-0.33%	100.97%
SST Low Re	0.5018	0.0093	1.94%	21.97%	0.9220	0.0117	1.08%	29.18%
$k-kl-\omega$	0.5142	0.0075	4.46%	-1.81%	0.9618	0.0093	5.44%	3.03%
Transition SST	0.4883	0.0076	-0.82%	-0.77%	0.9326	0.0093	2.24%	2.67%

For these 2D simulations, a pressure-based segregated solver was considered, with the SIMPLE scheme. For the models without transition modeling (one and two-equation models), a steady, second-order spatial discretization numerical scheme resulted in a relatively quick convergence with all residuals becoming smaller than the 1×10^{-6} criteria defined. Nevertheless, for the Transition SST and $k-kl-\omega$ models, second-order schemes were resulting in a poor convergence for the continuity and k turbulence

Table 5.3: Comparison between experimental, XFOIL and Fluent results for AoA of 12 degrees.

	AoA = 12°			
	Cl	Cd	% Cl	% Cd
Experimental	1.4504	0.0341		
XFOIL	1.4500	0.0292	-0.03%	-14.47%
SA	1.6215	0.0316	11.79%	-7.43%
$k-\epsilon$ Realizable	1.5718	0.0402	8.37%	17.74%
SST Low Re	1.4854	0.0581	2.41%	70.32%
$k-kl-\omega$	1.6219	0.0397	11.82%	16.46%
Transition SST	1.4867	0.0361	2.50%	5.89%

equations, so, first-order upwind schemes were used for these equations. This modification managed to reduce the residuals to the criteria, while compromising the accuracy of the results, as the drag coefficient values were twice as high when compared with the experimental ones . This variation was expected to occur due to the low order schemes adopted as stated in 2.4.2. Resorting again to second-order schemes for all equations and using the previous solution as initial conditions, the lift and drag coefficient were presenting oscillations around a value much closer to the experimental one. A transient (unsteady) simulation was then run, which resulted in all equations converging.

The one-equation SA turbulence model over-predicts drag by up to 75% for 0° and 4° AoA. This method does not model transition, therefore it assumes turbulent flow right from the airfoil leading edge, contrary to what XFOIL and the transition models predict, which demonstrate that for these small angles of attack, a considerable portion of the upper surface is in the laminar regime, having a lower drag contribution than turbulent flow.

The $k-\epsilon$ Realizable presents a substantial discrepancy in the drag coefficient values, up to twice as much as the experimental ones for small angles of attack. This corroborates the necessity of using a model capable of accurately predicting the physics of the viscous sub-layer without resorting to wall functions.

The results of $k-\omega$ SST model were very similar to the SA, with the drag prediction significantly improving after the Low Reynolds correction was added to it, with errors dropping to around 30%, still significantly high. For an AoA of 12°, the drag coefficient exhibits a considerable discrepancy compared to the UIUC data. One reason might be due to the difficulty in providing accurate results when considerable separation occurs and no real transition prediction.

Transition models feature much closer to the experimental ones for the simulated AoA than the previous one and two-equation models. Both of them manage to capture the LSB which occurs at the upper surface of the airfoil, inducing the transition to turbulent flow; however, no noteworthy changes can be observed either in the location of the LSB nor in the length of it. The $k-kl-\omega$ model exhibits drag values higher than the Transition SST model and this tendency is more significant with higher AoA. Studies from Aftab, Rafie, Razak, and Ahmad (2016) on a NACA4415 at Low Reynolds support this trends, in which the $k-kl-\omega$ predicted the location of the LSB but not the turbulent reattachment; additionally, the $k-kl-\omega$ model presented convergence problems and required a higher computational effort than

the Transition SST.

By incorporating an accurate transition model and featuring the most concordant results with the experimental ones, this study validates the selection of the SST transition method as the go-to model for airfoil flow analysis under a LRN regime.

5.3 2D CFD Simulations

With the physical model set, the solution method resorts to a SIMPLE scheme using steady-state first order spacial numerical schemes initially for rapid convergence and to approximate the solution to the real one, followed by a transient simulation with second-order temporal and spacial schemes for more accurate results.

For a transient simulation using the pressure-based solver, a time-step must be defined. The time step should be carefully selected: if it is too small, the simulation takes an excessive amount of time to be solved, while a time step too large does not capture the small changes in the flow and does not converge in a couple of iterations. The time step should be defined to capture a single particle around 20 to 50 times in the region of interest, and convergence should be achieved in 20 to 30 iterations per time step. For the inlet velocity prescribed and the tested airfoil chord, a time step of $0.5 \times 10^{-3} s$ captures a particle around 30 times on the airfoil vicinity. For this time step, the solution converges in around 40 iterations, with all residuals below 10^{-6}.

Figure 5.3 plots the lift and drag polars for the available data from UIUC, XFOIL results for integer AoA inside the range of available experimental data, as well as the results from Fluent simulations only for even numbers of AoA, due to time constraints. XFOIL exhibits errors below 7% for the lift coefficient when compared to the experimental data, while the drag coefficient is always under-predicted by around 10%, reaching 15% for high AoA. These results validate the use of XFOIL as a quick and reliable software to compute the lift coefficient of an airfoil at low Reynolds and an order of magnitude for the drag coefficient.

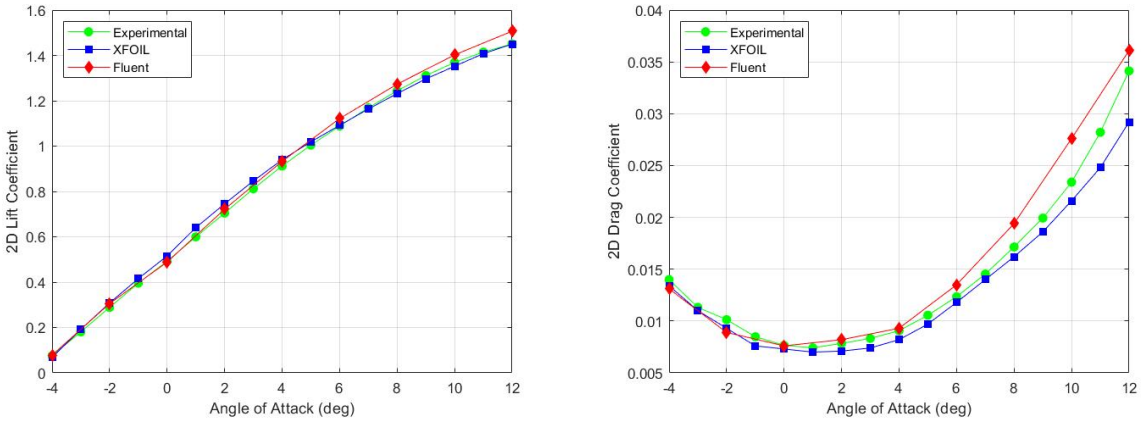

(a) Cl vs alpha curve

(b) Cd vs alpha curve

Figure 5.3: Aerodynamic polars for the SG6042 airfoil.

The lift coefficient data from the Fluent simulation using the Transition SST model is concordant with the experimental values, having discrepancies under 4% for the AoA simulated. For the drag coefficient, Fluent presents higher values than the experimental ones, with a tendency of increasing this discrepancy the higher the AoA is, up to 15%. This behavior is not concerning from a design standpoint, and it is more conservative than the values of low-fidelity software.

The intermittency factor included in the Transition SST model is used to turn on the production term of the turbulent kinetic energy downstream of the transition point. The model sets the intermittency to one on the freestream and to zero on the fluid region in contact with the airfoil (Menter et al., 2006). On the outer boundary layer, a small increase in the intermittency indicates the beginning of the LSB, while a unit value for the intermitency downstream, confirms that transition has occurred and the boundary layer is fully turbulent. As a result, this parameter is useful for predicting the location of the LSB in conjunction with the velocity contour plots.

While using $\gamma - Re_\theta$ transition model, a LSB was developed on the upper surface of the airfoil, being located closer to the trailing edge for low AoA and moving forward for increasing angles of attack. For negative AoA, a small bubble was also present near the leading edge of the airfoil at the lower surface, which is visible on Figure 5.4. The turbulent kinetic energy after the LSB becomes considerable (larger than one), confirming the presence of transition at these locations (Figure 5.5).

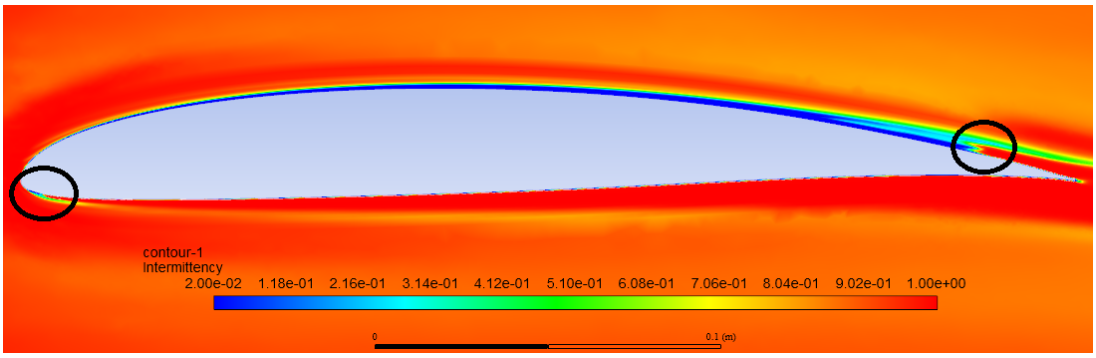

Figure 5.4: Intermittency factor for an AoA of -4°. Black circles indicate the location of the LSB.

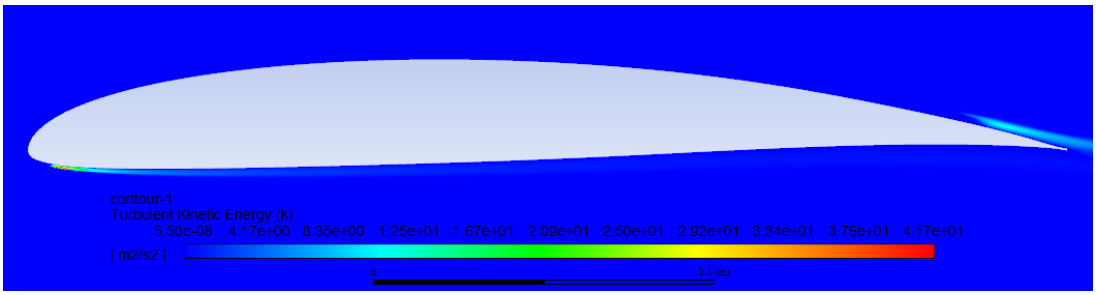

Figure 5.5: Turbulent kinetic energy for an AoA of -4°.

XFOIL is adapted to be used in the LRN regime where the LSB phenomenon is common. Without data regarding the fluid surrounding the airfoil, the LSB location can be inferred through the wall shear stress distribution along the airfoil surface, since XFOIL gives a negative value for the wall shear stress over regions with reverse flow tangent to the airfoil (McArthur, 2007). Figure 5.6 plots the skin friction

coefficient along the airfoil and confirms that XFOIL predicts the presence of the LSB in the same region as Fluent, both for the upper and lower bubbles, at an AoA of -4°. In Fluent, the skin-friction coefficient was always positive, so, at the reverse flow region, it was converted to its symmetric value to be coherent with the XFOIL data.

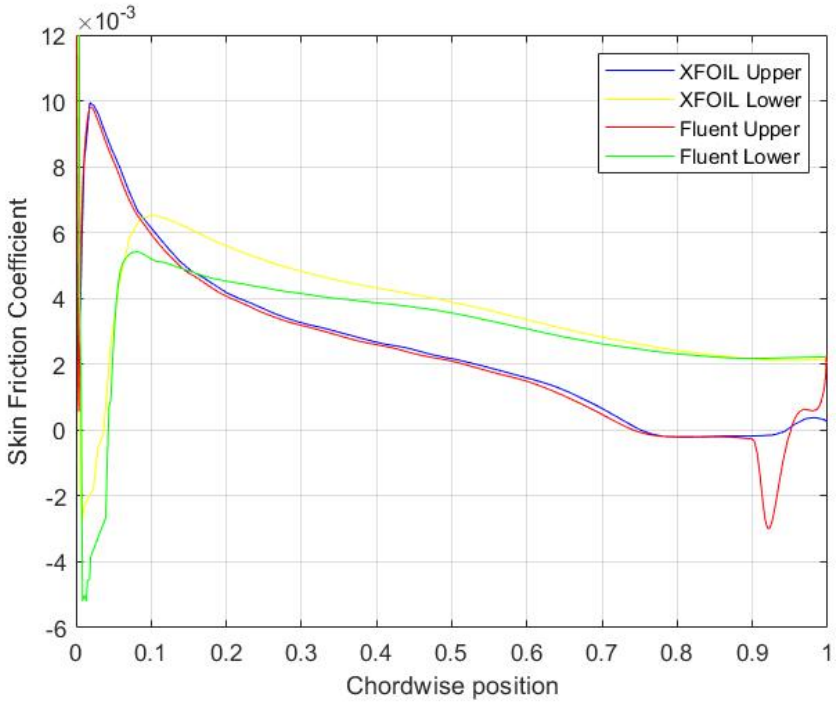

Figure 5.6: XFOIL – Skin friction coefficient distribution for an AoA of -4°.

Analyzing Figure 5.6, the skin friction coefficient along the upper surface is practically coincident until 90% of the chord, after which Fluent presents a sudden increase (absolute value) until around 95% chord. Looking at the velocity vector plot at this location, the reverse flow vortex is developed at this position, which has a higher adverse velocity gradient near the airfoil than the upstream ”dead air” region, as depicted in Figure 2.1. For the lower surface, both XFOIL and Fluent have the same behavior, with XFOIL predicting higher skin friction at the lower bubble near the leading edge while being lower than Fluent throughout the majority of the surface. The general trend is concordant with the typical skin friction plots, having a lower value in the laminar region, increasing at the transition, and having a small decay over the turbulent region.

At an AoA of 6°, separation starts to occur, confirmed by the presence of a blue region of null velocity over the upper surface of the airfoil at the trailing edge, bigger than the expected boundary layer total thickness. The separation region increases in size until 12°, the final AoA tested and comparable with UIUC data. At this attitude, the separation region occupies around 40% of the airfoil, however, according to XFOIL data, the lift coefficient increases up to 15°, at which the airfoil stalls. To validate these results, a Fluent analysis for 13, 14, 15, and 16° was conducted and, in fact, after 15° the lift coefficient starts decreasing. Figure 5.7 shows a velocity contour plot at an AoA of 15° where large separation is visible and vortex shedding is very active.

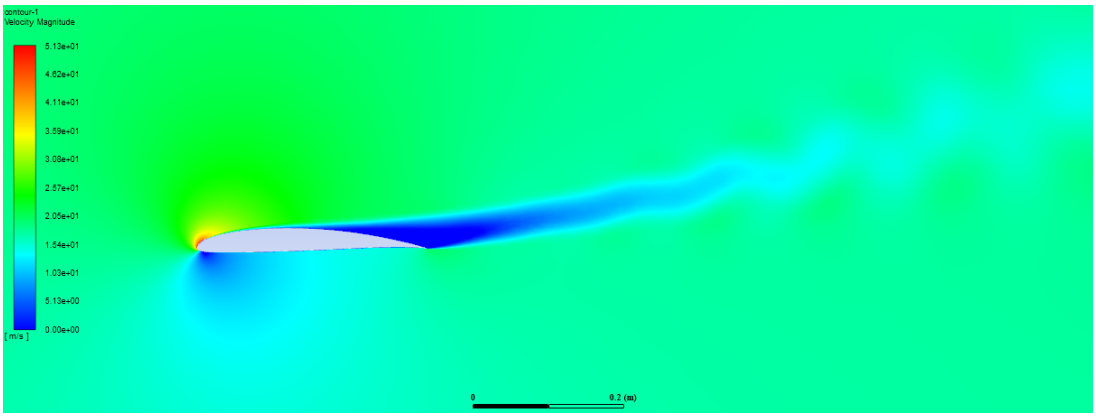

Figure 5.7: Velocity contour plot for an AoA of 15°.

The discrepancies between both software results and the experimental data can have multiple reasons. In XFOIL, a set of points of the airfoil is defined and line segments are created between them. To prevent sharp angles, at the region of bigger curvature (leading edge and trailing edge), more points are defined. Despite this improvement, the final airfoil shape is different from the real one and it can be one reason for the different outcomes. Additionally, the transition criteria e^N was applied with the default calibration, and no studies were performed by varying the N_{crit} parameter. Although giving this parameter the value of nine, the default for the wind tunnel conditions (Drela, 1989), small disturbances in the inlet conditions might change the indicated value for this variable.

Fluent uses the set of points imported and creates a spline curve from it, creating a smooth airfoil. Although using splines is better than using XFOIL since it does not create angles, the final shape might be slightly different from the real airfoil, thus, producing different results. Furthermore, the inlet conditions defined might be a little different from the wind tunnel conditions, namely some viscosity parameters of atmospheric conditions. Studies on different airfoils with variable turbulence intensities showed that increasing the freestream turbulence intensity resulted in earlier transition and reattachment, contributing to an overall decrease in LSB length (Istvan, Kurelek, & Yarusevych, 2018); resorting to CFD tools, the same conclusions were achieved by N. Silva (2014), corroborating the impact of the turbulence intensity at the inlet on the obtained results. The turbulence viscosity ratio was set according to the best practices provided, without any information of the experimental value; nevertheless; its influence is negligible, either in the results or at the location and size of the LSB, according to Veríssimo (2016). The grid convergence study was performed for the transition and turbulence model applied, for a specific angle of attack. Although the methodology used allowed using the same grid for all the spectrum of AoA studied by only changing the freestream orientation, the grid convergence should be done for every AoA simulated, a very time-consuming process. A similar study was done for an AoA of 0° with conclusions close to the ones described in subsection 5.2.2, which strengthens the robustness and accuracy of the considered grid for the 2D analysis conducted.

Chapter 6

Detailed Design – Aerodynamic Performance

With the turbulence and transition models validated in 2D, a full 3D analysis can be conducted to aerodynamically characterize the aircraft. Since XFLR5 is not recommended for a full plane analysis (with fuselage), the wing is modeled and simulated in Fluent and compared with XFLR5.

6.1 Analysis of 3D Wing

In the preliminary design phase, the wing geometry was defined according to the recommendations featured in the theoretical background and validated using the low-fidelity software XFLR5. At this stage, CFD methods are employed to corroborate the previous results and verify if the wing geometry is suitable and meets up with the project requirements.

6.1.1 Domain Characterization and Mesh Studies

A 3D model of the wing was created, similar to the 2D analysis previously presented. Since Fluent has a symmetry boundary condition option, only half of the wing is considered to greatly reduce the computational time of the simulations. The fluid domain consists of a semi-sphere upstream of the wing and a cylinder downstream, with the boundaries at least 60 chords away from the wing, which guarantees that over the span-wise direction, the fluid domain boundary is at least ten wingspans apart from the wing (Veríssimo, 2016). This creates a C shape on the symmetry boundary, similar to the airfoil simulation. A second control volume was created around the wing to capture the wake and possible vortex shedding up to five chords away from the trailing edge.

For the mesh generation, tetrahedral cells are chosen and the same principles considered before are applied to the 3D case: the base cell size is set and all the refinements done are a fraction of this base value, except the inflation layer, which is kept constant. Since the number of elements for 3D simulations is much bigger than in 2D cases, the same level of refinement is not possible to translate to the wing

since the computational time and effort would be impracticable. A growth rate of 1.25 is set for the main domain and 1.15 for the second control volume, closer to the wing, to better predict the phenomena in this region. The bias factor applied on the airfoil surface for the 2D case is not possible to replicate in 3D, as the automatic mesh generation software does not allow a progressive surface sizing in the chordwise direction. As a result, both the upper and lower surfaces were divided into 2 regions each: one from the leading edge to around 10% of the chord to apply a smaller surface cell size to better account for the high curvature of this wing region, and the remaining one, which is more smooth and does not require such a small cell size. The wing has a fifth surface corresponding to the finite trailing edge, which was created for the same reasons as explained in the 2D case.

Since the same turbulence and transition model are applied, $y^+_{target} < 1$ is a conditions for the models to be valid. To account for higher values of y^+ expected, 0.5 is considered the target for the calculation, yielding $y_1 = 1.01 \times 10^{-5}\ m$, a total of 30 layers with a growth rate of 1.2 to capture the whole boundary layer. The BL is predicted to have at most a thickness of around $1 \times 10^{-2}\ m$, according to Equation (5.1).

To select the most appropriate mesh, five meshes were created with the base cell size and the refinements varying in the same proportion. Based on the lift and drag coefficients and on the computational time, the most appropriate mesh is chosen for further simulations. Each mesh simulation was run using first-order and second-order spatial schemes for a steady case and also for a second-order transient temporal discretization.

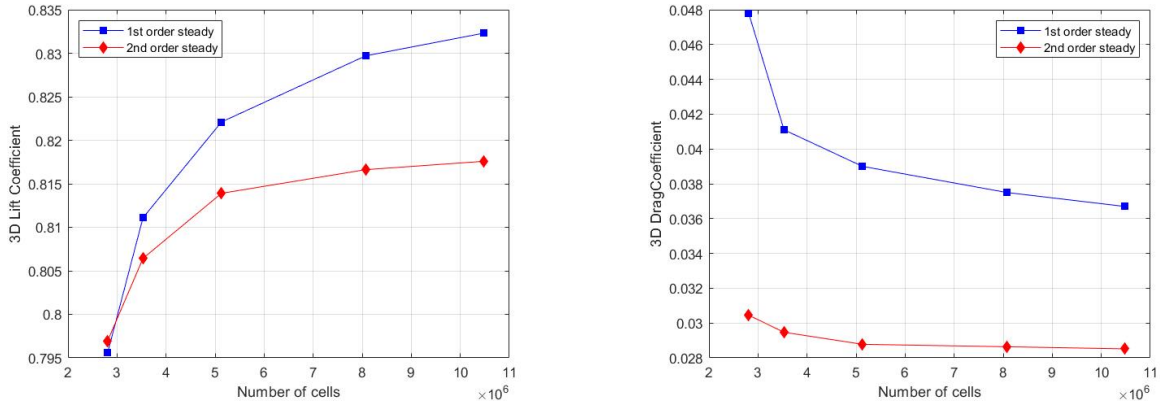

(a) C_l evolution (b) C_d evolution

Figure 6.1: 3D Wing mesh convergence study.

The plots in Figure 6.1 represent the evolution of C_L and C_D for the five meshes. Looking at the results obtained, the first order steady simulations exhibits a higher lift and drag coefficient for each of the five simulations run when compared to the second order, both steady and transient, even though all of them tend to converge as the number of elements increases. XFLR5 predicts $C_L = 0.8347$ and $C_D = 0.0270$ for the 4.5° AoA simulated in this study. Although first order simulations are much quicker than the remaining ones, they present a drag coefficient over 40% higher than XFLR5 even for the most fine mesh considered, discarding them from being used in further studies. The difference between the results obtained from second order steady and transient solutions is almost negligible, with the transient one taking over 6 times more time than the second order steady one. This analysis justifies the choice

of running second order steady simulations, however, if for high AoA, poor residual convergence occur or oscillations on C_L and C_D , a transient solution might be necessary.

Assuming the results of the most refined mesh as reference, the deviation of both lift and drag coefficients were computed to choose the most appropriate mesh. The ”intermediate” mesh, having 5.13M cells, has a deviation of less than 0.5% for C_L and 1% for C_D, featuring a good compromise between result accuracy and computational time, and is thus used for further analysis.

For 3D flow analysis, Fluent can transform a tetrahedral mesh into a polygonal one. A polygonal mesh can have up to three to five times fewer cells with the same level of refinement, however in the presence of inflation layers, the cell count reduction is not so pronounced (Ansys Inc., 2013). While the mesh has fewer cells in total, which would decrease the computational time, each cell has more faces and neighbors, requiring more gradients to be computed, thus having the opposite effect. Overall, after transforming the mesh to polygons, the minimum skewness has increased, which is a preliminary indicator of a better mesh quality.

A similar convergence study was performed using the five previous meshes converted to polyhedral elements. The results show the same tendency as the tetrahedral ones for an AoA of 4.5° with the ”intermediate” polygonal mesh having a good compromise between accuracy and processing time, nevertheless, for conditions near stall, the behavior is slightly different: an in-depth analysis was conducted comparing the original tetrahedral mesh to its polygonal transformation (3.52M cell polygon mesh), and to a polygonal mesh with a number of elements close to the original one. This was achieved by slightly refining the previous mesh, which gave origin to a 5.01M cell polygonal mesh. The general characteristics of each mesh are given in Table 6.1.

Table 6.1: Properties of the meshes.

Cell Geometry	Nr. of Cells	Nr. of Faces
Tetrahedral	5.13M	11.87M
Polyhedral	3.52M	13.53M
Polyhedral	5.01M	19.24M

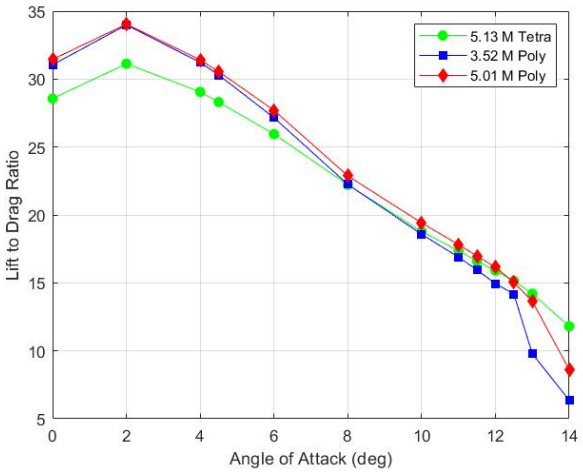

Figure 6.2: Lift to drag ratio at various AoA.

The lift-to-drag ratio obtained for various AoA by the three meshes in question is plotted in Figure 6.2. At low AoA, both polyhedral meshes exhibit similar results, corroborating the conclusions from the polyhedral convergence study that the 3.52M poly mesh was suitable for simulations at 4.5°. However, the polyhedral meshes present higher aerodynamic efficiency than the tetrahedral mesh up to 8°.

Analyzing the results near stall and at an AoA above 11°, the tendency stated before is inverted:

the 5.13M tetra mesh has a higher L/D ratio than both polyhedral meshes, and the 3.52M poly mesh exhibits a considerable difference from the 5.01M poly mesh, indicating that for high AoA, an increase in the mesh refinement has a substantial impact on the results obtained.

The characteristics of each mesh, displayed in Table 6.1, confirm the increase in the number of faces and the decrease in the number of cells compared to its tetrahedral counterpart (5.13M tetra to 3.52M poly). No noteworthy differences were encountered in the computational time between these two meshes, while the third one took more time. From all the analysis done, the 5.12M tetrahedral mesh will be used for the wing analysis since, for cruise conditions, this mesh is more conservative than the others, and without experimental data to confirm which one is more accurate, being conservative is the safest option. Furthermore, while the solution time is similar, the extra step of converting the mesh to polyhedral takes some time and no significant gains are obtained by doing it.

6.1.2 Wing Aerodynamic Analysis

With the mesh defined, a comparison of the lift and drag polars is done between XFLR5 and Fluent, illustrated in Figure 6.3. For low AoA, Fluent and XFLR5 provide similar outcomes, which justifies using the latter in the initial design stages. XFLR5 presents slightly higher lift and lower drag values, with the differences becoming more pronounced for higher AoA. As expected, XFLR5 does not provide results beyond stall, and even while approaching stall, special care should be taken (Dantsker & Vahora, 2018). After 6°, Fluent expresses a noticeable decrease in the lift coefficient, having a maximum value of 1.310 at 12.5°, a stall later than the 11.5 ° depicted by XFLR5. For the drag curve, XFLR5 having higher values than Fluent for the same angle of attack can be misleading: if the comparison is made between both stall conditions, Fluent has a higher drag coefficient than XFLR5 as the transition and turbulence model from Fluent is more accurate than the 2D viscosity extrapolation to 3D from XFLR5 (Menter et al., 2006; Peerlings, 2018).

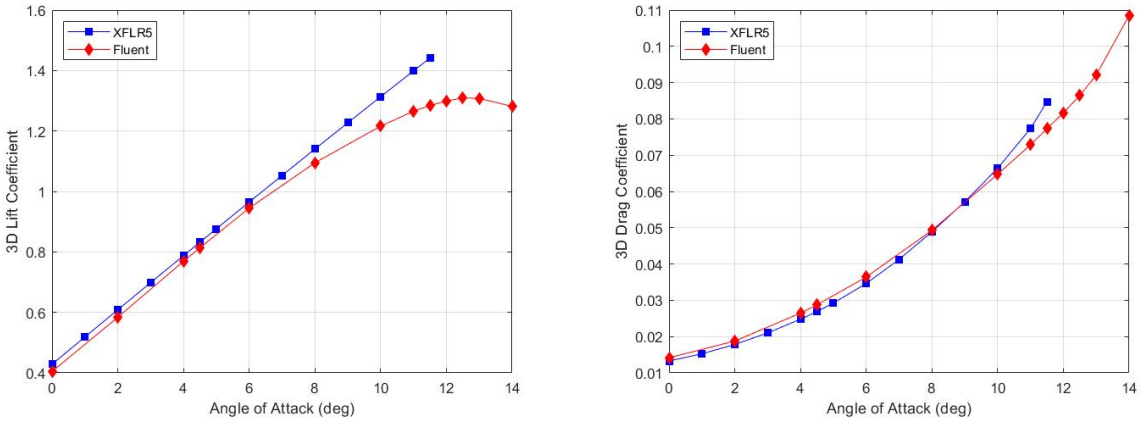

(a) C_l vs AoA evolution

(b) C_d vs AoA evolution

Figure 6.3: 3D Wing lift and drag coefficients

In the 2D analysis previously done, the laminar separation bubble was present and induced the transition from laminar to turbulent flow. Depending on the angle of attack, this bubble varies in its

location and thickness. To predict the location of the LSB on the 3D wing model, velocity contour plots with a negative value in the freestream direction were generated; this phenomenon occurs in two situations: in the presence of an adverse pressure gradient and in the recirculation inside the LSB. Additionally, from Figure 5.5, the turbulent kinetic energy has a sudden increase after transition and starts decaying after a short length, therefore it can also be useful to locate the transition region. Figure 6.4a depicts the reverse flow region in red and high turbulent kinetic energy regions in blue, indicating that the flow is laminar until around 70% of the chord and turbulent after the LSB located in that region. The pressure coefficient – C_p – of three sections of the wing, plotted in Figure 6.4b, supports these findings: all three sections have the same pressure coefficient behavior, and a sudden decrease in C_p is visible in the same region where the LSB is predicted.

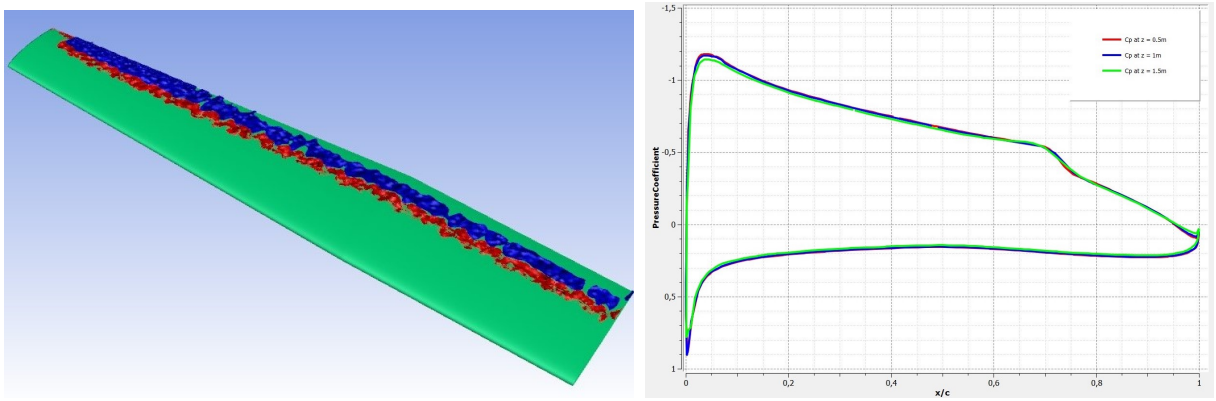

(a) Reverse flow region (red) and high turbulent kinetic energy regions (blue) for an AoA of 4.5°.

(b) Pressure coefficient plots of wing sections at z=0.5m, z=1m and z=1.5m.

Figure 6.4: 3D Wing lift and drag coefficients

As the angle of attack increases, the LSB moves to the leading edge and a higher portion of the wing upper surface becomes turbulent. As the wing attitude approaches stall conditions, separation starts to occur at the trailing edge. Figure 6.5 is similar to the previous case, for an AoA of 14°. Two distinct phenomena are visible: near the leading edge, the presence of the LSB similar to Figure 6.4a, and at the trailing edge, a reverse flow region and an increase in the turbulent kinetic energy caused by the separation of the flow from the upper surface. At some wing sections, only one continuous blue region is noticeable as the LSB bursts and separation occurs right from the leading edge. The velocity contour plots over wing sections at $0.5m$ and $1.5m$ in the spanwise direction are shown in Figure 6.6a and 6.6b, respectively. In the first one, although not clear, the existence of a blue region near the leading edge indicates the LSB, and turbulent flow is developed until separation around 75% of the chord. At $z = 1.5m$, the flow never reattaches after the LSB and separation occurs immediately. These burst phenomena are chaotic and, for the same angle of attack, the regions where they occur are random and change over time, resulting in oscillations in the lift and drag coefficients even after the solution has converged. As the angle of attack further increases, more regions on the upper surface have flow fully detached and the lift coefficient further decreases.

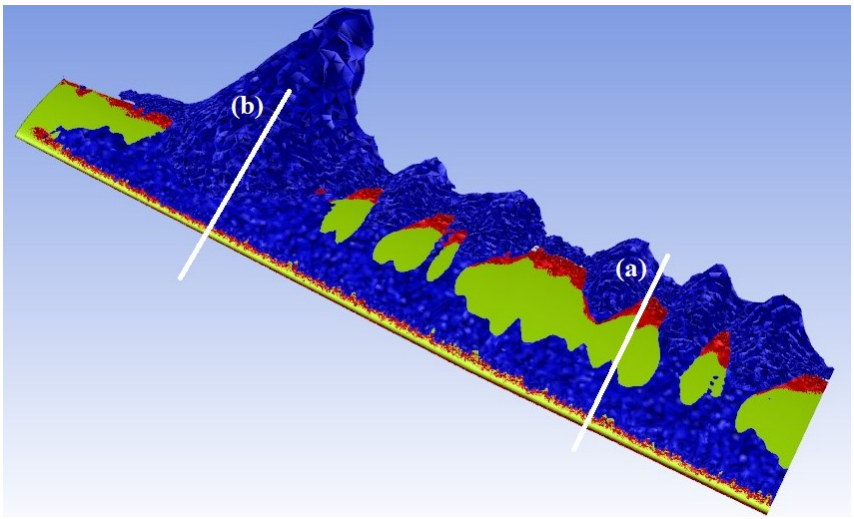

Figure 6.5: Reverse flow region (red) and high turbulent kinetic energy regions (blue) for an AoA of 14°.

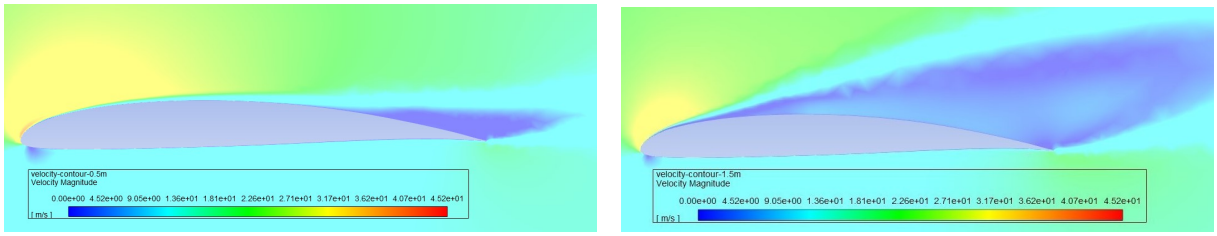

(a) z = 0.5m (b) z = 1.5m

Figure 6.6: Velocity contour plots at two different wing sections for an AoA of 14°.

6.1.3 Parametric Studies to Enhance Wing Performance

Geometric twist at the tip of the wing

With the wing design in the preliminary phase fully characterized, the author conducts some parametric studies in order to improve its aerodynamic characteristics. As stated in section 2.2.2, adding twist to a wing can delay stall conditions at the tip and approximate the lift distribution to the ideal elliptical one, thus reducing the induced drag component. In the preliminary phase, Sá (2021) idealized a wing structure for the outer wing panels that has a single spar located around 30% of the chord; this position is defined as the center of rotation to avoid twisting the spar. Moreover, on the interior wing panel (rectangular part), twist will not be applied to avoid further modifications to the wing-boom connection, and the twist variation on the outer panel will be linear.

The values provided in subsection 2.2.2 were retrieved from Sadrey (2013) and are relative to aircraft much heavier than the UAV designed. Without further information on the geometric twist angles of Class I UAVs, a simple and quick analysis using XFLR5 is conducted to check which is the most beneficial twist angle to be applied.

For twist angles smaller than 2°, both lift and drag exhibited little variance when compared to the original geometry. Angles steeper than 5° present a reduction in both the lift and drag coefficients. For this case, the wing AoA has to be higher to produce the same lift force. Comparing attitudes with the same lift coefficient, the drag force was higher for the twisted wing than in original geometry. The author

defines the incidence angle of the tip as being 3.5° lower than the incidence angle of the inner wing panel, to perform further studies using CFD tools.

Simulations for various angles of attack were performed and the results showed little to no difference in the aerodynamic polar up to the maximum lift coefficient of the baseline wing. Nevertheless, the AoA has to be between 0.75° and 1° higher on the twisted wing to match the C_L produced by the baseline model. Due to this, the angle of attack at which the twisted wing stalls is 13.5°, with its maximum lift coefficient being the same as the original wing. The major difference is in the wing portion, which begins to enter in stall first. In the baseline wing geometry, the outer panel of the wing was the one entering in stall first, a phenomenon not desired as this is where the control surfaces are located, which lose their effectiveness in stall conditions. Figure 6.7a represents the streamlines of the baseline geometry at an AoA of 14°, an attitude in the stall region which corroborates the conclusions derived from Figure 6.5. In the proposed wing geometry with twist, stall occurs initially at the root of the wing and propagates to the tip, as seen in Figure 6.7b, allowing the aircraft to recover and keep control over roll motion.

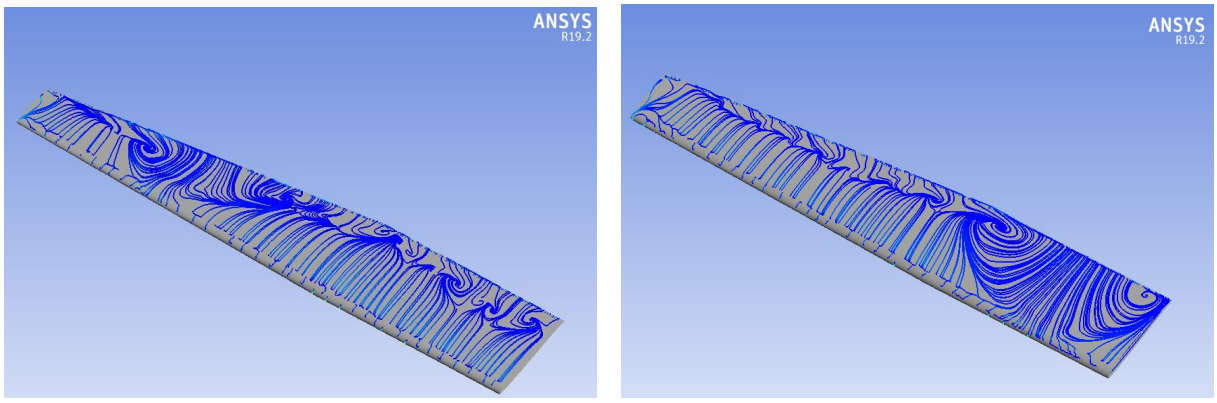

(a) Original wing at an AoA of 14°

(b) Wing with twist at an AoA of 15°

Figure 6.7: Streamlines over the upper surface of the wing at the beginning of the stall region.

Wingtip configurations

Another improvement that can be made to the wing is to modify its tip geometry and configuration to reduce the effects of wingtip vortices and, consequently, reduce the induced drag. Induced drag decreases as the aspect ratio of the wing increases, however, wingspan constraints or structural difficulties may impose a maximum aspect ratio (Raymer, 1992). To tackle this problem, choosing a wingtip configuration that reduces the strength of the vortices is beneficial and leads to an increase in the effective AR (Gudmundsson, 2014).

One option is to simply reshape the tip of the wing in such a way that these effects are diminished, reducing the induced drag. A Hoerner wingtip is a simple solution adopted by most of the UAVs in CIAFA. This configuration has a sharp finishing on the tip, obtained by performing a flat cut on the wing, as seen in Figure 6.8a. The leading edge has a round shape to prevent the upper surface from stalling at low angles of attack (Gudmundsson, 2014).

Applying the Hoerner tip on the baseline wing resulted in a decrease of just 1.5% on the drag coefficient, with the lift generation not being affected. While a reduction in the drag is always beneficial,

this reduction is quite small and may be misleading. Although the same mesh properties were used for this study, it is important to note that during the mesh convergence study, this grid had a deviation in the order of 1% when compared to the most refined one. The results may just reflect a small change in the grid and not actual changes in the wingtip vortices, as no remarkable differences were observed in the vorticity distribution nor in the wingtip vortex strength in the CFD post-processing plots and results.

Other wingtip configurations are more effective at reducing the induced drag. Two types are common in general aviation: raked tips, which are a prolongation of the wing on the same plane as the wing – Figure 6.8b, and winglets, which also extend the wing vertically (up, down, or a combination of both) – Figure 6.8c. Both of these configurations increase the effective wingspan of the aircraft and have a larger wet area due to the added structure. For these configurations to be viable, the gains in reducing the induced drag component need to outweigh the increase in the skin-friction component, and optimization studies on the geometry of each design must be thought out. The raked wingtip can vary in span length, taper, sweep, and dihedral, and the winglet can also have its toe angle vary.

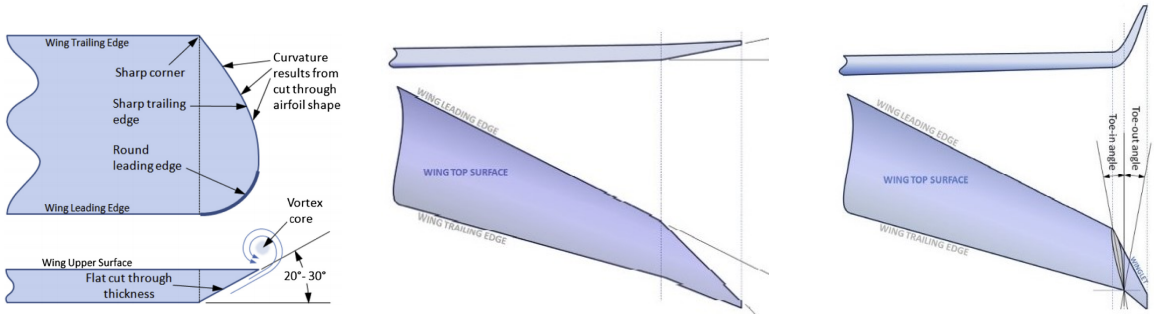

(a) Hoerner wingtip (b) Raked tip (c) Winglet

Figure 6.8: Examples of possible wingtip configurations. Retrieved from Gudmundsson (2014).

Preliminary studies done on XFLR5 showed a small gain (up to 4%) in the aerodynamic efficiency of the wing. Nevertheless, when trying to keep the wingspan fixed at 4 m, both of these options could not be applied, and even when the wing was slightly shortened to introduce these wingtip devices (while keeping the total wing area), these alterations performed worse than the original planform. If the wingspan constraint was violated and the wingtip devices study was carried out, the additional structure also comes with the drawback of increasing the MTOM of the UAV, and trade-off studies should be carried out to check the real effectiveness of the wingtip configuration.

While advantages were observed with these parametric studies, especially with the introduction of geometric twist, their influence on the remaining areas of the project is unknown and has not been studied, namely on the wing structure. As a result, the author will continue the detailed analysis with the design fixed on the preliminary phase, which is also the one considered by Sá (2021) and P. Silva (2021) in the detail design in the structural and propulsion areas, respectively.

6.2 VTOL System wind tunnel Testing

Due to the complexity of the rotors' geometry, calculating the parasitic drag produced by these components during cruise poses some challenges, as seen in the preliminary phase. A viable alternative is to perform wind tunnel tests to determine the impact of this sub-system on the total aircraft drag.

To proceed with the experiment, a physical assembly was created with the VTOL system mounted on a boom, as illustrated in Figure 6.9. The distance between the front and rear rotors is $1.19\ m$, and because both systems are the same, the center of vertical thrust is the midpoint between the rotors and coincides with the CG of the aircraft. To connect the motors to the booms, a support was created in Solidworks and 3D-printed, and the Electronic Speed Controller (ESC) of each motor was attached under their support. To nullify the torque from the rotors, diagonally opposite rotors rotate in the same direction (Khan, 2014). As a result, the rotors used in the assembly are symmetrically equal: the front rotor rotates clockwise while the rear one rotates counterclockwise, as visible in Figure 6.9 by looking at the leading edge of each rotor. On the other boom, the front and rear rotors swap positions.

Figure 6.9: Boom with VTOL system to be tested in the wind tunnel.

The test conditions should be as similar as possible to the operation ones, as such, cruise velocity is replicated in the wind tunnel. The atmospheric conditions (static pressure, relative humidity, and temperature) are given by a precise in-room climate measurement device, while a pitot tube located near the testing area outputs the dynamic pressure – q. Applying the perfect gas law - Equation (6.1), dynamic pressure equation – Equation (6.2) and Sutherland's law – Equation (6.3) gives the air density, freestream velocity, and dynamic viscosity, respectively. Table 6.2 sums up the conditions for the tests conducted. To remove the influence of the boom and the balance arm, the drag of these components without the VTOL system was obtained for the same freestream conditions, and the data presented throughout this section is already subtracted by the results from this control test.

$$p = \rho R T \quad , \; with \quad R = 287 \; J/kgK \tag{6.1}$$

$$q = \frac{1}{2}\rho U^2 \tag{6.2}$$

$$\mu = \mu_{ref} \left(\frac{T}{T_{ref}} \right)^{3/2} \frac{T_{ref} + S_\mu}{T + S_\mu} \quad , \; with \quad \mu_{ref} = 1.718 \times 10^{-5} \; kg/(ms) \; , \; T_{ref} = 273.15 \; K \; , \; S_\mu = 110.4 \; K \tag{6.3}$$

Table 6.2: Wind tunnel testing conditions.

Data				Calculations		
Climate Sensor	Temperature	23.9	$°C$	Density	1.181	kg/m^3
	Static Pressure	1006.7	kPa	Velocity	19.69	m/s
Pitot Tube	Dynamic Pressure	229	Pa	Dynamic Viscosity	1.832E-05	$Pa.s$

As the vertical climb phase end and some horizontal velocity is achieved, the rotors will stop rotating in an arbitrary position and their stopping position is independent from each other, for this reason, the tests were executed for a combination of possible stopping positions for the rotor. For the sake of clarity, the angle of the rotor ϕ is measured relative to the spanwise direction (rotor perpendicular to the freestream) and positive angles in the clockwise direction. Increments of 45° were applied, which translates into four different angles tested for each rotor (for a two-blade propeller, after 180° the position is the same), resulting in a total of sixteen different configurations evaluated, enough data to understand the general trend of the results. Figure 6.10 illustrates the positions considered for the front rotor. Although the rear rotor rotates in the opposite direction, its position definition is the same as the front rotor, following the birds-eye view from Figure 6.10.

(a) $\phi = -\pi/4 \; rad$ (b) $\phi = 0 \; rad$ (c) $\phi = \pi/4 \; rad$ (d) $\phi = \pi/2 \; rad$

Figure 6.10: Stopping positions considered for the front rotor.

Each test ran for around 30 seconds, and data regarding the force and moments around the three axis was obtained. The data provided by the balance and the testing software already outputs the mean value and the standard deviation for the test duration, thus easing the data processing step. Figure 6.11 depicts the mean drag values obtained for each combination of rotor position, along with a first-order two-variable polynomial-trigonometric curve fitting equation. The curve-fitting equation expression is given by Equation (6.4), in which z corresponds to the drag force and ϕ_1 and ϕ_2, the front and rear rotor position angle, respectively. Annex A provides in greater detail the results obtained in a table with the

mean values, along with the standard deviation, together with the values obtained in the vertical direction – lift generation. Additionally, the formulation of the curve-fitting equation is also described in Annex A.

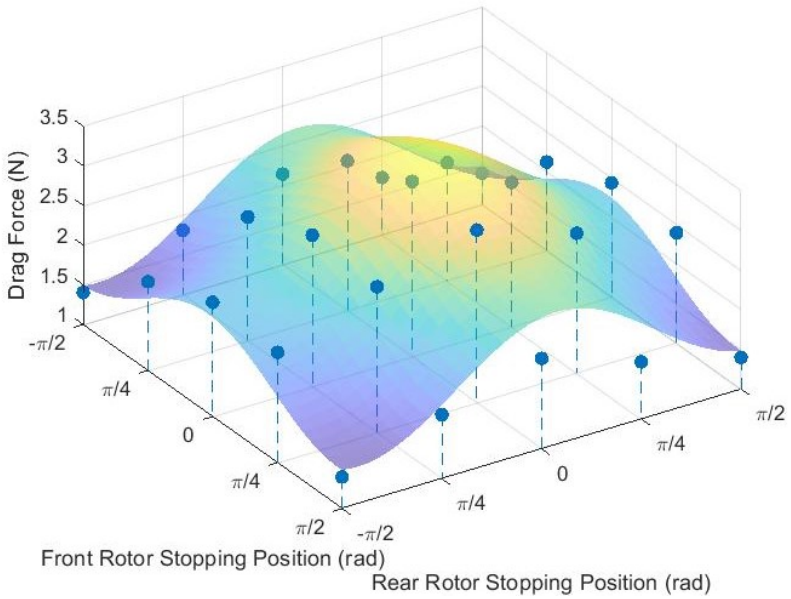

Figure 6.11: Mean values of the drag force obtained in each test, with the curve-fitting equation.

$$z = a + c_1 cos(2\phi_1 + f_1) + d_1 sin(2\phi_1 + g_1) + c_2 cos(2\phi_2 + f_2) + d_2 sin(2\phi_2 + g_2) \tag{6.4}$$

$$a = 2.453 \quad c_1 = 0.2373 \quad c_2 = -0.7637 \quad d_1 = 0.615 \quad d_2 = -0.6392$$
$$f_1 = 3.57 \quad f_2 = 1.962 \quad g_1 = 1.801 \quad g_2 = -0.4765$$

The curve-fitting equation from Equation 6.4 has a $R^2 = 0.91138$, having a good correlation with the experimental data, following the trends of the drag values obtained and providing a reasonable estimation for the drag produced by these components. Because the number of data collected is small, a second order curve-fitting provided a perfect correlation, nevertheless, the graph and values presented for intermediate, not tested angles ($\phi = \pm\ \pi/3\ rad$,$\phi = \pm\ (2\pi)/3\ rad$, for example) were not physically correct. Furthermore, the standard deviation values, while not significantly high, indicate that some uncertainty occurs in the data gathered, which gives more margin for slight changes in the real drag values and might benefit the curve-fitting equation.

Analyzing the results obtained, it confirms that, for the spectrum of positions tested, the combination which provides the least drag is when the rotors are aligned with the booms – $\phi = \pi/2\ rad$, while the worst case corresponds to $\phi = 0\ rad$, with the rotor spanwise direction perpendicular to the freestream, having a drag force over 230% when compared to the previous case.

The results obtained also confirm the conclusions stated by Mendes (2021): the front rotor has a greater impact on the drag produced than the rear one. This can be deduced by comparing the results from Table A.1 when the front rotor is at $0\ rad$ and the rear at $\pi/2\ rad$, with the opposite case: the first case produces a higher drag than the second. One explanation for this phenomenon is that the rear

VTOL set is located in the wake produced by the front set, reducing the drag produced by the former.

Another inquisitive phenomenon that occurred is that the drag is higher whenever the leading edge of the rotor is ahead of the motor ($\pi/4\ rad$ for the front and $-\pi/4\ rad$ for the rear) than when it is behind. When decomposing the drag into viscous and induced components, the viscous part should remain relatively similar for both cases as they have the same surface in contact with the airflow, therefore it is the induced component which varies. Analyzing the force in the vertical direction, presented in Table A.3, it follows the same tendency as the drag force, corroborating the hypothesis stated before.

Although the test conditions were defined to resemble the cruise conditions, it is impossible to fully replicate them in the wind tunnel, and thus, the drag forces measured should be transformed into their coefficient form. Considering the wind tunnel density and freestream velocity, the drag coefficient of the full VTOL system (4 motors and 4 rotors) varies between 0.00891 and 0.0204, with the reference area being the wing. When comparing these results with the ones computed in the preliminary design phase (subsection 4.3.3), the lower bound is slightly lower by less than 5% while the upper bound is significantly higher by 20%. These variations come as no surprise since empirical estimations for propellers were applied and the T-Motor 22x7.4 rotors were specially designed for vertical flight operations, which makes their geometry different from a standard propeller and their characteristics at 70% of its radius might not accurately represent the rotor properties; for example, incidence angle of the rotor at 40% of its radius is higher than the $\beta_{0.7r}$ used, as well as the chord at this location, if the properties at this location were used in the preliminary phase, the drag at $\phi = 0\ rad$ would have increase and thus approximate the results to the experimental ones Furthermore, one hypothesis for the higher discrepancy in the upper bound can be related to the lift production at this position, which, consequently, causes an induced drag, not predicted by the drag formulation considered in the preliminary phase.

6.3 Complete Aircraft Analysis

To define the aerodynamic properties of the UAV, a CAD model of the full aircraft (only the right half since the symmetry boundary condition is applied) was created to serve as the basis for Fluent simulations. While the preliminary design indicated that the wing would produce the required lift for cruise at an angle of $4.5°$, it is expected that this angle will have to be higher when performing the simulations in Fluent for two reasons: Figure 6.3a demonstrated that, for a 3D wing model, Fluent features a lower lift coefficient than XFLR5 for all AoA; when the tail was added to XFLR5, a slight reduction in C_L occurred, a tendency which is prone to be more severe if more components are added to Fluent. As a result, the wing is set with an incidence of $5.5°$ for the initial UAV CAD model.

Due to the complexity of some components and the connections between them, some simplifications had to be made. In the mesh generation process, small angles between two surfaces pose some problems due to interference between the inflation layers of these surfaces. At these locations, a smoother transition was achieved by creating a chamfer of fillet on the problematic edges. Figure 6.12a displays the CAD model created in Ansys DesignModeler.

The front gear from Figure 4.3a has small holes, a gap for the spring that acts as a shock-absorber,

and a finite distance between the wheels and the gear strut. Modeling this geometry with all these details requires excessive refinements in the mesh generation, increasing the number of elements and the computational time without gaining noticeable accuracy in the final result (Veríssimo, 2016). The decision is to simply model the strut and add the wheels attached to it, without any gaps in between. The same approach was taken for the main landing gear.

The domain where the inlet and outlet boundary conditions are applied is similar to the one used in section 6.1, forming a C-shape at the symmetry plane with the boundaries over 60 chords away from the wing of the UAV. Additionally, a block is created, containing the entire aircraft in order to apply a smaller refinement to the fluid zone closer to the UAV during the meshing process. Both the domain and this refinement block can be seen in Figure 6.12b.

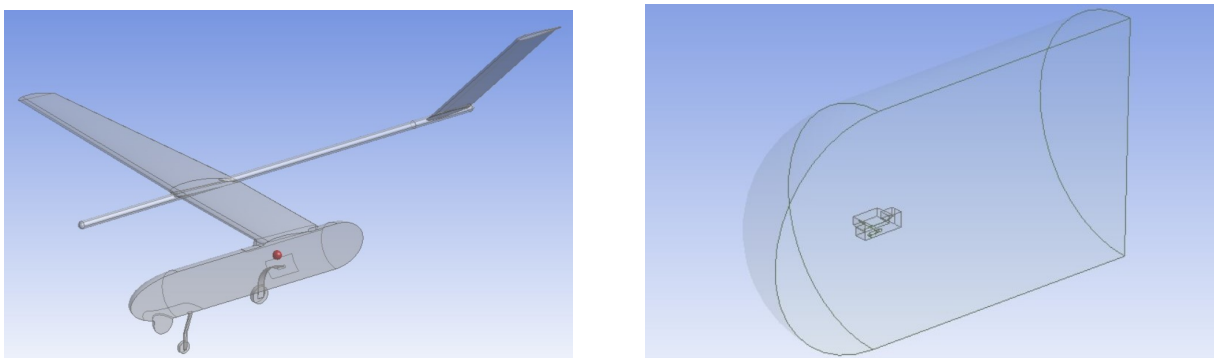

(a) CAD model of half of the UAV

(b) C-shape domain and refinement region near the UAV

Figure 6.12: CAD model of the UAV and the domain considered for Fluent.

The considerations taken for the 3D wing mesh generation process are used for the full aircraft: at the trailing edge of the wing and tail, a smaller region is created to apply a higher refinement and better capture the high curvature of the surface, as well as over the trailing edges. Furthermore, at the fuselage and booms, the surfaces around the connections with other components have a smaller refinement than the remainder of the component surface to control the stitching of the mesh between components and create a smoother transition between parts with high discrepancies in the surface cell sizes. Some of these regions are visible in Figure 6.12a like on the fuselage near the landing gear and camera, and at the back of the boom.

The base cell size to be used on each surface was chosen according to the general dimensions of each component in order to divide each one into a similar number of partitions, with the exception of the wing and tail, which have a smaller cell size to better estimate the production of lift by these parts. To define the inflation layer properties, Equation (5.1) and (5.2) are applied. Each component has its own characteristic length, as such, the inflation layer, first layer, and total height are not constant for the entire aircraft. Table 6.3 indicates the parameters to be applied for the inflation layer to each component. The growth rate of the inflation layer is kept at 1.2, similar to the previous simulations, and $y^+_{target} = 0.5$ to have a safety margin in order to guarantee that after the mesh is generated, this value is always smaller than the unit.

With a baseline mesh defined, a grid independence study was performed. A coarser grid was cre-

Table 6.3: Inflation layer properties for each component.

Component	Characteristic Length (m)	y_1 (m)	δ (m)	Nr. of layers
Wing	0.353	1.02×10^{-5}	1.01×10^{-2}	30
Tail	0.255	9.99×10^{-6}	7.68×10^{-3}	28
Fuselage	1.400	2.93×10^{-5}	3.04×10^{-2}	30
Booms	2.341	3.34×10^{-5}	4.58×10^{-2}	31
Camera	0.112	9.43×10^{-6}	4.02×10^{-3}	25
Front Landing Gear Strut	0.015	8.16×10^{-6}	8.06×10^{-4}	17
Front Landing Gear Wheels	0.060	9.01×10^{-6}	2.44×10^{-3}	22
Rear Landing Gear Strut	0.035	8.67×10^{-6}	1.59×10^{-3}	20
Rear Landing Gear Wheels	0.089	9.27×10^{-6}	3.35×10^{-3}	24

ated, as well as four finer grids. Figure 6.13 shows the lift and drag coefficient obtained for each mesh. It is important to note that the meshes created have their base cell sizes and surface sizes as a fixed percentage of the baseline mesh. Due to mesh stitching errors and non-conformities that happened in the mesh generation process, this percentage does not follow any pattern since some desired cell refinements could not be performed. Nevertheless, both aerodynamic coefficients tend to converge as the number of cells in each mesh increases. The computational time required to obtain a solution was also a decisive factor for the mesh selection: Table 6.4 indicates an approximation of the required time to obtain a converged solution, with the time exponentially increasing as the mesh elements become smaller. For reference, the hardware used to perform the CFD simulations had a 6-core 2.20 GHz CPU and a 16 GB RAM. The most refined mesh took around three full days to generate results, and due to time constraints and computer processing limitations, no finer meshes were possible to be generated and solved. A compromise between accuracy and computational effort was made, with the author choosing the fourth mesh to be used in further studies, having a total of 15.02M cells, requiring around one day to be solved. In terms of accuracy, in comparison with the finer mesh, it has a lower C_L value with a difference of under 0.25% and a higher C_D with a discrepancy of under 2%. Although the computational time might be seen as relatively high, this was the 'lightest' mesh that had an error low enough to be acceptable.

The selected mesh yields $C_L = 0.8076$ and $C_D = 0.05175$. These results showed that at 0° of AoA with a wing incidence of 5.5°, the UAV does not produce the required lift for cruise, as a result, the wing incidence is set to 5.75° providing $C_L = 0.8214$ while having a $C_D = 0.05441$. Table 6.5 compares the results from this analysis with the drag build up done on the preliminary phase. The first line of the table is related solely to the CFD results from the UAV model without the VTOL system incorporated, the other two lines add the drag coefficient from the wind tunnel tests to the previous CFD result; the drag coefficient values related to the preliminary phase were computed using Equation (2.2) using the values obtained at the end of chapter 4, with K constant and C_{D_0} varying according to each case.

Analyzing solely the UAV without the VTOL set reveals that the preliminary drag estimation is smaller by around 10% compared to the CFD results. Although the empirical expressions used in the drag build-up phase were carefully chosen according to the shape of the components analyzed, most of the

Table 6.4: Properties of the UAV meshes.

Nr. of Cells	Solver Time (h)
5.23 M	5.5
7.05 M	7.5
10.28 M	12.5
15.02 M	23
16.84 M	30.5
22.63 M	72

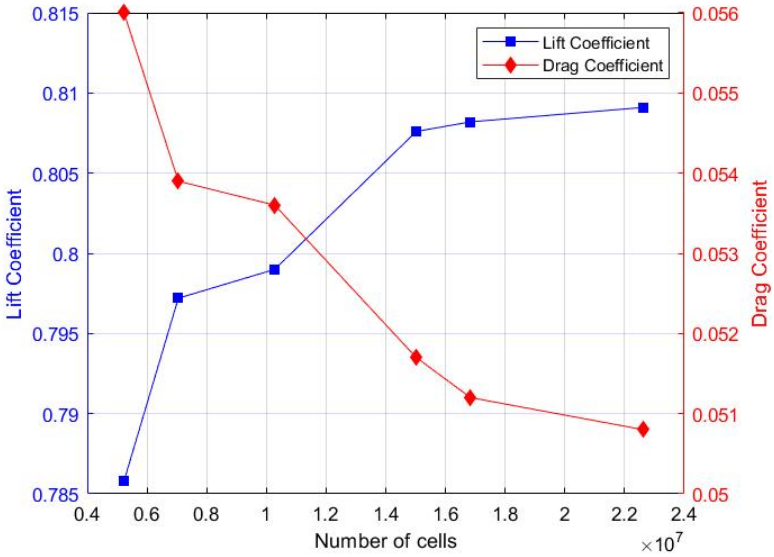

Figure 6.13: UAV Mesh convergence study.

Table 6.5: Lift and drag coefficients from Fluent for the UAV plus wind tunnel data for the VTOL system.

	CFD + Tunnel results (case A)		Preliminary results	C_D Difference (%)
	C_L	C_D	C_D	
UAV - No VTOL	0.8214	0.05441	0.04891	-10.12%
UAV - VTOL Parallel	0.8214	0.06332	0.06006	-5.16%
UAV - VTOL Perpendicular	0.8292	0.07481	0.06627	-11.41%

coefficients mentioned in the literature were obtained from experimental data of components used in general aviation, those being larger scale components subjected to higher flow speeds (Hoerner, 1965). Additionally, the preliminary drag build-up fails to account for the interference drag, which occurs due to the physical connections between structures and boundary layer and flow interference. When adding the VTOL system, the drag predictions follow the same tendency as presented in section 4.3.3, as expected.

6.3.1 VTOL System Integration

Without a CAD model of the rotors or additional information provided by the supplier, adding these components to the UAV model poses some difficulties. Silva created a CAD model of the T-Motor 22x7.4 rotor by molding the rotor in wax, after the creation of a negative mold in plaster. The details of the rotor CAD construction are depicted in his dissertation (P. Silva, 2021). This rotor CAD model was used, and the motors were approximated as cylinders with the dimensions from T-Motor (2021); a smooth connection between the motors and the booms was also generated. Regarding the mesh, a fine refinement was made on the rotor blades to capture its high curvature and an inflation layer was created. Following the methodology for the inflation layer settings, the rotor characteristic length changes according to the rotor position relative to the freestream. Since only the maximum and minimum drag positions will be considered for the full UAV simulation, the characteristic length of the rotors corresponds to their chord at 70% radius and their diameter, respectively.

With the integration of the VTOL system into the CAD model, the converged mesh reached around 19.4M cells, taking around 42 to 48 hours to solve. The results of the simulation are displayed in Table 6.6 with the CFD UAV model having a wing incidence of 5.75° and 0° AoA. For the preliminary results presented, the consideration stated in the previous table is valid: for the C_L obtained in Fluent, Equation 2.2 outputs the C_D value.

Table 6.6: Lift and drag coefficients regarding the full aircraft simulated in Fluent.

	CFD results (case B)		Preliminary results	C_D Difference (%)
	C_L	C_D	C_D	
UAV - VTOL Parallel	0.8112	0.06241	0.05944	-4.76%
UAV - VTOL Perpendicular	0.8169	0.07390	0.06553	-11.32%

Although the results from the CFD simulation fail to achieve the required lift for cruise ($C_{L_{cr}} = 0.8269$), a small AoA is considered for cruise conditions, which avoids changing the wing incidence once again and remaking the whole CAD model and mesh. Further analysis confirms this small angle is at most 0.15°, to obtain the required lift for cruise with little change to the drag coefficient (around 1 to 1.5% higher drag due to an increase in the induced component for both cases). Once again, the CFD model exhibits a higher drag coefficient than what the preliminary studies indicated. These results were expected since the full UAV model simulated in Fluent is able to account for the interference drag. Additionally, the drag difference is larger when the rotors are perpendicular, confirming once again the lack of reliability in the empirical expressions used for the rotors in the preliminary phase.

A comparison between these results and the ones obtained using the UAV in Fluent (without VTOL system) plus wind tunnel data brings some interesting conclusions. For simplicity the first case will be denominated case A (UAV model without VTOL in CFD + wind tunnel data for VTOL) and the latter case B (complete aircraft in CFD). For the same wing incidence and angle of attack, case B presents a lower lift coefficient. This can be explained by the fact that a portion of the wing is under the influence of the front rotors' wake (Figure 6.16), disturbing the airflow reaching the leading edge of the wing and reducing the local lift production in that region (visible in Figure 6.14 with a reduction in the pressure difference on the region above the boom and behind the front rotor). While this influence was expected to be larger whenever the rotors were perpendicular to the airflow, the wind tunnel tests showed that the rotors also produced lift when they are at this position, thus balancing the wing's lift losses.

Although the drag coefficient is not directly comparable since the lift coefficient is marginally different, this difference is so small that some nuances can be deduced. Overall, C_D is slightly higher in case A. One hypothesis for this behavior might be related to the fact that the VTOL system on the wind tunnel assembly was located at the end of the boom, while in the CAD model, the boom goes beyond each motor, ending in a dome ahead of the front rotor, and at the back, the boom extends up to the tail location. This change reduces the wet area of the motor and the supports on the CAD model, thus reducing the skin-friction drag component. Moreover, in the wind tunnel assembly, the front support had a flat area perpendicular to the freestream, which is the least aerodynamic shape possible and increases the pressure drag downstream of this structure (Hoerner, 1965). Furthermore, if a small increase in the

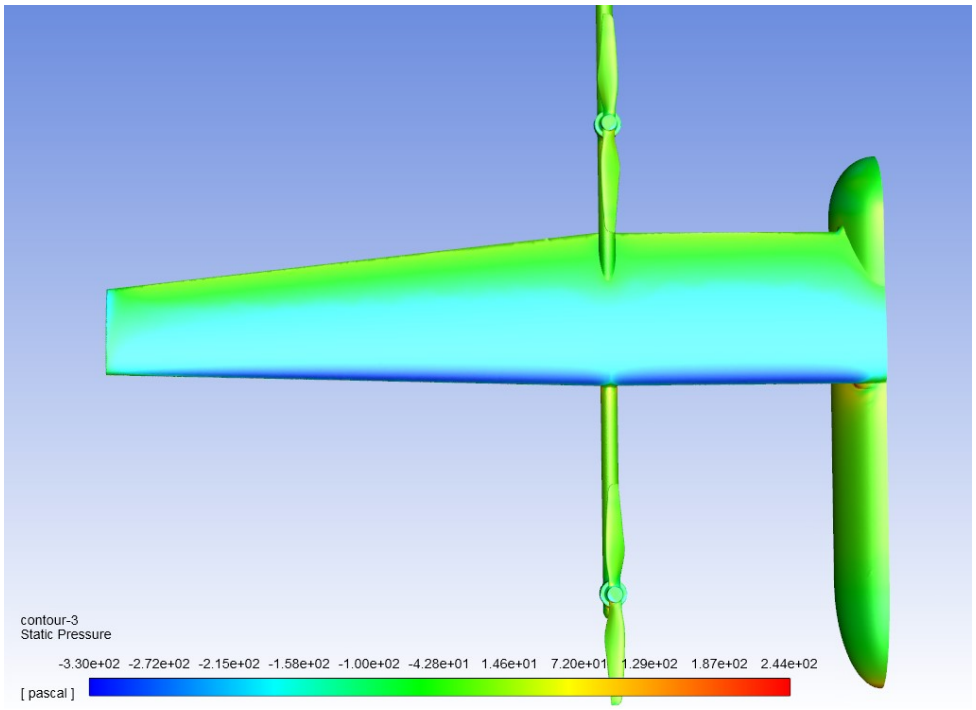

Figure 6.14: Pressure distribution over the wing at an AoA of 0°.

AoA is considered for case B to match the lift coefficient of both cases, C_D will also increase, narrowing the gap between the two cases.

Non-slender components have a big impact on the total drag, as seen in Figure 6.15 which is a velocity plot of the flow at the symmetry plane. The optical camera's and the front landing gear strut's wake significantly contribute to the form drag component. Moreover, in the same picture, it is visible that, on the rear of the fuselage, some detachment and vortex shedding are occurring; in reality, this phenomena would not occur, at least in these proportions, since the propeller located at this position would provide an active suction of the flow and prevent the BL from detaching due to the curvature of the fuselage rear. Figure 6.16 is a velocity contour plot, similar to Figure 6.15, for a plane parallel to the symmetry plane, located at the booms and rotor. In this figure, the wake produced by the front rotor is visible and extends over the wing and up to the rear rotor, confirming the hypothesis stated before.

To study the behavior of the aircraft at different attitudes, simulations using the full UAV CAD model were performed for different AoA to obtain the drag polar. In this study, only the case in which the rotors are parallel to the booms is considered.

The evolution of UAV lift and pitch moment coefficient with angle of attack is depicted in Figure 6.17a. The lift curve slope exhibits the typical linear behavior up to an AoA of 4° and reaches a maximum value of 1.31 at 7°, after which, stall is bound to occur. This $C_{L_{max}}$ is smaller than the 1.35 value predicted in the conceptual phase, which affects the wing loading constraint at stall. To have the same wing loading as initial thought and considering this updated value for $C_{L_{max}}$, stall speed needs to increase from 28 kts to 28.4 kts, according to Equation (3.3). This poses no noteworthy changes since the increment in the stall speed is small and there is still enough margin for the flight speeds defined in the mission profile. The moment coefficient around the CG, confirms that the UAV is naturally stable by having a

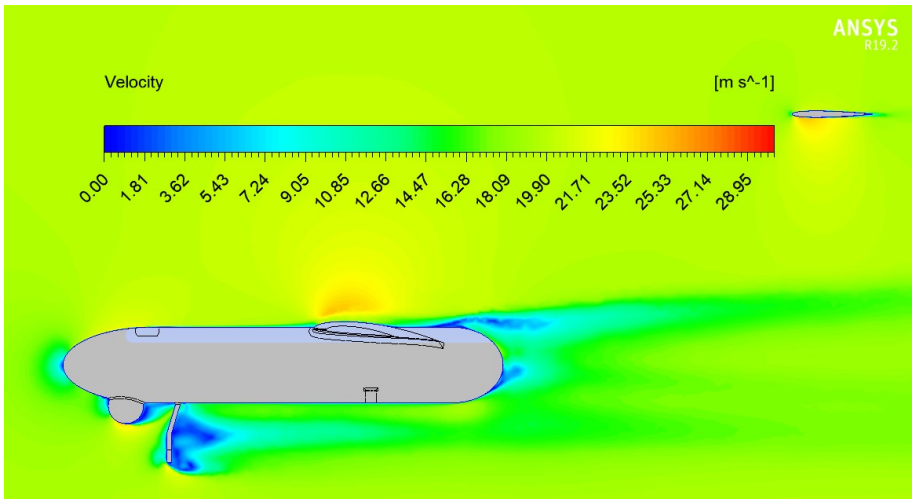

Figure 6.15: Velocity contour plot at the symmetry plane z=0m.

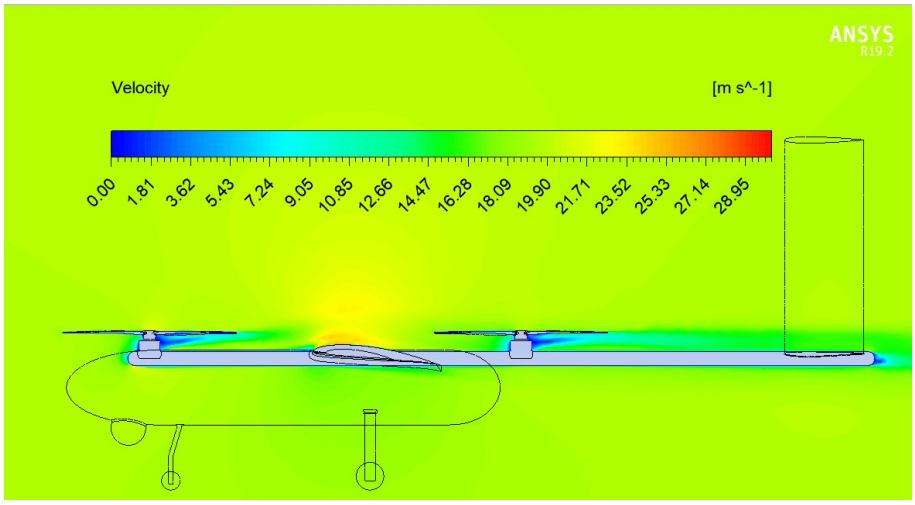

Figure 6.16: Velocity contour plot at the booms z=0.72m.

negative value for C_{M_α}. The angle of attack at which the moment coefficient is null is slightly higher than the one required for cruise, yet, this difference is so small that a null moment coefficient at cruise can be achieved with a slight deflection of both ruddervators upward, as stated in subsection 4.4.1.

The data retrieved to construct the drag polar, represented in Figure 6.17, is the same as the one in the previous figure, in which each scatter mark stands for a different AoA, ranging from -6° to 7.5°. It is important to note that the minimum drag value can not be seen on the polar since this value occurs at an angle of attack smaller than the lowest AoA simulated in CFD. This is due to the fact that the wing incidence was set to 5.75°, meaning that on cruise, the wing is effectively operating at an angle of around 6° and based on the XFLR5 results, the wing minimum drag was obtained at an angle below -3° which would correspond to an AoA near -9°. The drag polar has the typical parabola shape up to C_L values of 1.2, with the drag significantly increasing after this point. The maximum lift coefficient corresponds to the beginning of the stall region, after which the lift coefficient decreases and drag increases. The physical phenomena related to stall can be seen in Figure 6.6, in which regions of separated flow dominate the upper wing surface, increasing the form drag produced by the wing.

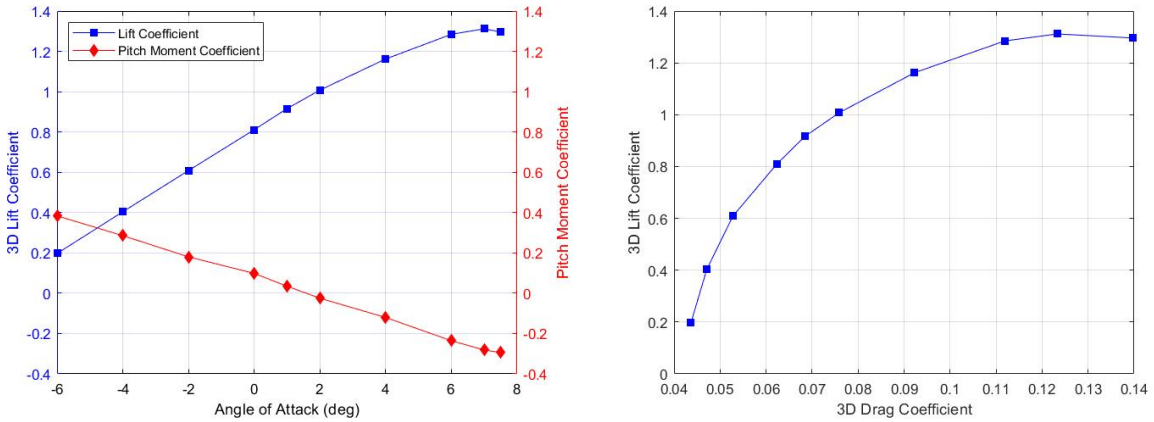

(a) CL alpha and CM alpha curves

(b) Drag polar

Figure 6.17: Aerodynamic graphs for the UAV with rotors parallel to booms.

Table 6.7 sums up the conclusions taken from the aerodynamic analysis of the UAV designed with this data being extracted from the graphs in Figure 6.17, which is related to the best case (rotors parallel to freestream). Correcting the value of Table 6.6 to match the cruise lift coefficient, $C_{D_{cruise}} = 0.07445$ for the perpendicular case.

Table 6.7: Aerodynamic properties of the UAV.

$C_{L_{max}}$	1.31
AoA for $C_{L_{max}}$	7°
Cruise lift coefficient	0.8269
Cruise AoA	0.15°
Cruise drag coefficient	0.06321
Maximum L/D	13.39
AoA of maximum L/D	1°
Maximum $L^{3/2}/D$	13.58
AoA of maximum $L^{3/2}/D$	4°

Table 6.8: Performance update of the UAV.

Stall Speed	28.40 kts
Thrust required for cruise	16.32 – 19.22 N
Fuel cell output required for cruise[1]	654.0 – 756.0 W
Thrust required for climb	39.21 - 41.94 N
Power output required for climb[1][2]	1387 – 1471 W
Total flight time	3h05 – 3h25

Table 6.8 uses the results from the final CFD simulations to update the flight performance data calculated at the end of the preliminary phase. For the thrust, power, and endurance, both the lower and upper bounds are shown to exhibit the impact of the rotors' stopping position. These results reinforce, once again, the necessity of thinking about a stopping mechanism for the rotor in the least drag position, as this may increase the endurance of the UAV by up to 20 minutes (10% more flight time).

[1] This value includes motor required power, motor and ESC efficiencies and avionics and camera power consumption
[2] 800 W come from the fuel cell and the remaining from batteries attached to the fuel cell

Chapter 7

Conclusions

7.1 Achievements

At the beginning of this document, the objectives of the project in which this thesis takes part were defined, consisting of the design of a small UAV powered by a fuel cell and capable of performing VTOL, with the author focusing its study on aerodynamics and flight performance. This objective was fulfilled by following a step-by-step approach from the conceptual phase up to the detailed design.

In the initial phase, the author's contributions to aerodynamic parameters like the Oswald efficiency factor and the parasite drag coefficient allowed the project members to come up with a viable solution for the design process. Since the output of the detailed phases of all the project members was in agreement with the initial design, the conceptual design can be considered a success as it guided the project on the right track.

The previous two parameters were target of an exhaustive analysis in the preliminary phase, with the Oswald efficiency factor taking into account the wing geometry defined at this stage, and the parasite drag the influence of each aircraft component in contact with the airflow. These studies demonstrated that most of the aircraft's drag at cruise is due to the parasite component, with the VTOL propulsion system contributing to this component by around 25 to 40% of the total parasite drag, depending on the rotor's stopping position after the vertical take-off segment.

Before starting the detailed design using CFD tools, the turbulence model and mesh general properties were validated by comparing the results of 2D simulations of the wing's airfoil with experimental data. The SST $k-\omega$ turbulence model, in conjunction with the $\gamma - Re_\theta$, was found to be the most appropriate for the case, accurately predicting the location of the laminar separation bubble and transition, as well as the separation phenomena at high angles of attack.

When conducting CFD simulation of the 3D wing model, the results were similar to XFLR5 for AoA lower than 6° with a reduction in lift and an increase in drag for attitudes above these angles. These simulations allowed the author to understand the post-stall behavior of the wing, which fomented the application of twist to the wing. This modification managed to slightly reduce the drag produced by the wing at high AoA and changed the stall behavior by making the root stall before the tips, as pretended.

Regarding the VTOL system, the preliminary drag estimates of these components present discrepancies of up to 20% when compared to the wind tunnel data gathered. These differences might be related to the rotor geometry being different from typical propellers and the properties at 70% radius, not accurately reflecting the geometry of the rotor. For the UAV without this system modeled, CFD simulations resulted in a drag coefficient 10% higher in contrast with the drag build-up, as CFD tools are able to account for the interference drag.

The entire aircraft modeling and subsequent mesh generation posed some challenges due to the UAV complexity and intricate geometries, which resulted in failed grids or grids of poor quality. Some simplifications and smooth transitions between components had to be made to obtain results in a timely manner. Additionally, the hardware used to run Fluent was not the most optimal which highly influenced the time it took to obtain results and limited their accuracy and precision, as finer meshes were unfeasible to generate and solve. Nevertheless, the results, obtained in Fluent, are similar to the previous case, which also confirms the impact of the rotor's stopping position: when the UAV has all rotors perpendicular to the freestream, it produces 15% more drag in total than when all rotors are parallel to the freestream. This impacts the total flight time of the UAV by reducing it from 3h25 to 3h05.

The main objective of the present dissertation has been achieved, with the baseline aircraft aerodynamic properties being computed with high-fidelity tools. The presence of a VTOL system in a conventional configuration is unusual, and the current work makes an important and valuable contribution in understanding the interference of this system in the cruise flight segment for small UAVs.

7.2 Future Work

The present dissertation featured the aerodynamic characterization of the baseline solution achieved after the preliminary phase. While simple studies regarding modifications to the wing were conducted with promising outcomes, due to temporal and computational limitations, their impact on the total aircraft could not be assessed. Applying wingtip devices may reduce the induced drag component, however, this addition must be balanced with the increase in the skin-friction drag and additional weight. The author suggests using a dedicated optimization tool to improve the aerodynamic efficiency of the wing and study its impact on the whole aircraft.

Although a preliminary longitudinal static stability analysis was performed, it should be extended to incorporate lateral stability with the definition of the aileron characteristics, together with the dynamic stability for both motions. CFD simulations could be run to obtain the stability derivatives of the UAV.

During the course of the dissertation, it became evident how much the rotor stopping position impacts the drag at cruise conditions. A stopping mechanism ought to be thought to block the rotor in a position where it is aligned with the boom. A mechanical device such as a rod or a rotating arm, which would act only after the operation of the VTOL system ceased, may be a solution, nevertheless, its drag and weight impact must be assessed, as well as its effectiveness.

The aerodynamic characterization of the UAV was performed using CFD tools, with its definitions validated from the 2D analysis performed. Nevertheless, wind tunnel testing of a scale model would

allow a comparison between the computational and experimental data.

Regarding the state of the project, a coupling between the aerodynamics studies and the remaining areas of the project (P. Silva, 2021; Sá, 2021) should be conceived to end up with a UAV design ready for a prototype to be manufactured and tested. Other areas that were not studied by the project team, such as flight control, should also be explored. Additionally, the multidisciplinary optimization studies resulted in a second generation concept with improved endurance and slight changes in the UAV characteristics (Alves, 2021), and these properties ought to be confirmed using high-fidelity software.

Bibliography

Aftab, S., Rafie, A., Razak, N., & Ahmad, K. (2016, 04). Turbulence model selection for low reynolds number flows. *PloS one*, *11*. doi: 10.1371/journal.pone.0153755

Airbus. (2020a). *How hydrogen could be a game-changer for future aircraft.* Retrieved April 28, 2021, from https://www.airbus.com/newsroom/stories/Is-this-the-next-clean-energy-to-power-aviation.html

Airbus. (2020b). *Hydrogen in aviation: how close is it?* Retrieved April 28, 2021, from https://www.airbus.com/newsroom/stories/hydrogen-aviation-understanding-challenges-to-widespread-adoption.html

Alves, B. (2021). *Multidisciplinary optimisation of an unmanned aerial vehicle with a fuel cell powered energy system* (Unpublished master's thesis). Academia da Força Aérea.

Alves, B., Coelho, V., Silva, P., Marta, A., Afonso, F., Sá, P., ... Caetano, J. (2021, July). Design of a hydrogen powered small electric fixed-wing uav with vtol capability. In A. C. Marta & A. Suleman (Eds.), *International conference on multidisciplinary design optimization of aerospace systems* (p. 290-304). Lisbon, Portugal: Aerobest 2021. (ISBN: 978-989-99424-8-6)

Anderson, J. D. (2010). *Fundamentals of aerodynamics* (5th ed.). McGraw-Hill. Hardcover.

Anderson, J. D. (2012). *Introduction to flight*. McGraw-Hill.

Ansys Inc. (2010, 11). Ansys meshing user's guide, release 13.0 [Computer software manual].

Ansys Inc. (2013, 11). Ansys fluent user's guide, release 15.0 [Computer software manual].

Ansys Inc. (2021). *Ansys fluids computational fluid dynamics (cfd) simulation.* Retrieved June 18, 2021, from https://www.ansys.com/products/fluids

Austin, R. (2010). *Unmanned aircraft systems: Uavs design, development and deployment*. John Wiley and Sons.

BBC. (2021). *Afghanistan: Us says drone strike killed is-k planner.* Retrieved September 07, 2021, from https://www.bbc.com/news/world-asia-58364743

Boukoberine, M. N., Zhou, Z., & Benbouzid, M. (2019). A critical review on unmanned aerial vehicles power supply and energy management: Solutions, strategies, and prospects. *Applied Energy*, *255*, 113823. doi: 10.1016/j.apenergy.2019.113823

Brederode, V. (2018). *Aerodinâmica incompressível: Fundamentos* (2nd ed.). IST Press.

Coelho, D. (2019). *Conceptualization and application of unmanned aerial vehicles design methodology* (Master's thesis, Instituto Superior Técnico). Retrieved from https://fenix.tecnico.ulisboa

.pt/downloadFile/1407770020546924/IST_MSc_Thesis_78423.pdf

Cook, M. V. (2013). *Flight dynamic principles: A linear systems approach to aircraft stability and control* (3rd ed.). Elsevier.

Corke, T. C. (2003). *Design of aircraft*. New Jersey: Pearson Education, Inc.

Dantsker, O., & Vahora, M. (2018, 01). Comparison of aerodynamic characterization methods for design of unmanned aerial vehicles. *2018 AIAA Aerospace Sciences Meeting*. doi: 10.2514/6.2018-0272

Defense Turkey. (2017). *Bna tiltrotor uav is flight ready.* Retrieved September 12, 2021, from https://www.defenceturkey.com/en/content/bna-tiltrotor-uav-is-flight-ready-4146

Deperrois, A. (2009). Xflr5 - analysis of foils and wings operating at low reynolds numbers [Computer software manual].

Drela, M. (1989). An analysis and design system for low reynolds number airfoils. In *Conference on low reynolds number airfoil aerodynamics.*

Drela, M., & Youngren, H. (2001). Xfoil 6.9 user primer [Computer software manual].

Eubank, R., & Speckman, P. L. (1990). Curve fitting by polynomial-trigonometric regression. *Biometrika*, *77*, 1-9. doi: 10.1093/biomet/77.1.1

Fathi, M. K. (2019). *Wild area aerial protective inspector, proposal for 2018-2019 undergraduate individual aircraft linear infrastructure inspection uas* (Tech. Rep.). Tehran, Iran: Sharif University of Technology.

Federal Aviation Administration. (2016). *Pilot's handbook of aeronautical knowledge*. Aviation Supplies & Academics, Inc.

Força Aérea. (2021). *Força Aérea - Missão.* Retrieved March 26, 2021, from https://www.emfa.pt/p-709-mission

Gadalla, M., & Zafar, S. (2016). Analysis of a hydrogen fuel cell-pv power system for small uav. *International Journal of Hydrogen Energy*, *41*(15), 6422–6432. doi: 10.1016/j.ijhydene.2016.02.129

Group, T. E. (2014). *Falcon-v fixed wing vtol (vertical take off and landing) uav (unmanned aerial vehicle) aircraft.* Retrieved March 11, 2021, from http://www.top-enggroup.com/product.htm

Gudmundsson, S. (2014). *General aviation aircraft design: Applied methods and procedures*. Butterworth-Heinemann.

Gundlach, J. (2012). *Designing unmanned aircraft systems: A comprehensive approach*. American Institute of Aeronautics and Astronautics, Inc.

Hirsch, C. (2009). *Numerical computation of internal and external flows: Fundamentals of computational fluid dynamics* (2^{nd} ed.). Elsevier.

Hoerner, S. F. (1965). *Fluid-dynamic drag*. Hoerner fluid dynamics.

Houghton, E., Carpenter, P., Collicott, S. H., & Valentine, D. T. (2013). *Aerodynamics for engineering students* (6^{th} ed.). Elseview.

Howe, D. (2000). *Aircraft conceptual design synthesis*. Professional Engineering.

Ideal Simulations. (2020). *Cfd computational domain.* Retrieved July 04, 2021, from https://www.idealsimulations.com/resources/cfd-computational-domain/#

Intelligent Energy. (2021). *Our uav products.* Charnwood Building, Holywell Park, Ashby Road. Re-

trieved from https://www.intelligent-energy.com/our-products/uavs/

Istvan, M. S., Kurelek, J. W., & Yarusevych, S. (2018). Turbulence intensity effects on laminar separation bubbles formed over an airfoil. *AIAA Journal*, *56*(4), 1335-1347. doi: 10.2514/1.J056453

Joint Air Power Competence Centre - NATO. (2010, 1). *Strategic concept of employment for unmanned aircraft systems in NATO.*

Kadyk, T., Winnefeld, C., Hanke-Rauschenbach, R., & Krewer, U. (2018). Analysis and design of fuel cell systems for aviation. *Energies*, *11*(2), 375. doi: 10.3390/en11020375

Kalitzin, G., Medic, G., Iaccarino, G., & Durbin, P. (2005). Near-wall behavior of rans turbulence models and implications for wall functions. *Journal of Computational Physics*, *204*(1), 265-291. doi: 10 .1016/j.jcp.2004.10.018

Khan, M. (2014). Quadcopter flight dynamics. *International journal of scientific & technology research*, *3*(8), 130–135.

Langtry, R., Menter, F., Likki, S., Suzen, Y., Huang, P., & Völker, S. (2006, 07). A correlation-based transition model using local variables—part ii: Test cases and industrial applications. *ASME J. Turbomach*, *128*. doi: 10.1115/1.2184353

Launder, B., & Spalding, D. (1974). The numerical computation of turbulent flows. *Computer Methods in Applied Mechanics and Engineering*, *3*(2), 269-289. doi: 10.1016/0045-7825(74)90029-2

Li, B., Zhou, W., Sun, J., Wen, C.-Y., & Chen, C.-K. (2018). Development of model predictive controller for a tail-sitter vtol uav in hover flight. *Sensors*, *18*(9), 2859. doi: 10.3390/s18092859

Lowry, J. T. (1999). *Performance of light aircraft*. American Institute of Aeronautics and Astronautics, Inc.

Mathworks. (2004, 10). Curve fitting toolbox for use with matlab [Computer software manual].

McArthur, J. (2007). *Aerodynamics of wings at low reynolds numbers* (Doctoral dissertation, University of Southern California). Retrieved from https://www.kimerius.com/app/download/5784130381/Aerodynamics+of+wings+at+low+Reynolds+numbers.pdf

Mendes, P. (2021). *Design of a fixed-wing tilt-rotor quadcopter class i mini unmanned aircraft - propulsion system design and prototype manufacturings* (Unpublished master's thesis). Academia da Força Aérea.

Menter, F. (1994). Two-equation eddy-viscosity turbulence models for engineering applications. *AIAA Journal*, *32*, 1598-1605. doi: 10.2514/3.12149

Menter, F., Langtry, R., Likki, S., Suzen, Y., Huang, P., & Völker, S. (2006, 07). A correlation-based transition model using local variables—part i: Model formulation. *ASME J. Turbomach*, *128*. doi: 10.1115/1.2184352

Morgado, J., Santos, A., & Caetano, J. (2017). Portuguese air force research, development and innovation centre (CIDIFA): Rd&i in the area of autonomous unmanned aerial systems. *Instituto da Defesa Nacional*.

Moukalled, F., Mangani, L., & Darwish, M. (2015). *The finite volume method in computational fluid dynamics: An advanced introduction with openfoam and matlab* (1^{st} ed.). Springer Publishing Company, Incorporated.

Mrusek, B. (2021). Vertical takeoff and landing (vtol) small unmanned aircraft systems (suas). *Trends in Technical & Scientific Research*, *5*(1). doi: 1019081/TTSR.2021.05.555651

Mueller, T. J., & DeLaurier, J. D. (2003). Aerodynamics of small vehicles. *Annual Review of Fluid Mechanics*, *35*(1), 89-111. doi: 10.1146/annurev.fluid.35.101101.161102

NASA Open Source Agreement. (2021). *Openvsp.* Retrieved May 21, 2021, from `http://openvsp.org/wiki/doku.php`

National Oceanic Atmospheric Administration. (1976). *U.s. standard atmosphere* (Tech. Rep.). Washington D.C., USA: NASA.

Ng, W., & Datta, A. (2019). Hydrogen fuel cells and batteries for electric-vertical takeoff and landing aircraft. *Journal of Aircraft*, *56*(5), 1765–1782. doi: 10.2514/1.C035218

Niţă, M., & Scholz, D. (2012). Estimating the Oswald Factor from Basic Aircraft Geometrical Parameters. In *German aerospace congress 2012*.

OpenCFD Ltd. (2021). *Openfoam.* Retrieved June 18, 2021, from `https://www.openfoam.com/`

Park, S., Bae, J., Kim, Y., & Kim, S. (2013). Fault tolerant flight control system for the tilt-rotor uav. *Journal of the Franklin Institute*, *350*(9), 2535–2559. doi: 10.1016/j.jfranklin.2013.01.014

Peerlings, B. (2018). *A review of aerodynamic flow models, solution methods and solvers – and their applicability to aircraft conceptual design* (Tech. Rep.). Delft, Netherlands: Delft University of Technology.

Prisacariu, V. (2017). The history and the evolution of uavs from the beginning till the 70 s. In *Journal of defense resources management.* Air Force Academy, Brasov, Romania.

Pursee, P. E., & Campbell, J. P. (1944). *Experimental verification of a simplified vee tail theory and analysis of available data on complete models with vee tails* (Tech. Rep. No. 823). UNT Libraries Government Documents Department: NACA.

Raymer, D. P. (1992). *Aircraft design: A conceptual approach*. American Institute of Aeronautics and Astronautics, Inc.

Roskam, J., & Lan, C.-T. E. (2016). *Airplane aerodynamics and performance*. Design, Analysis and Research Corporation.

Sadrey, M. H. (2013). *Aircraft design - a systems engineering approach*. John Wiley & Sons, Ltd.

Schlichting, H. (1979). *Boundary-layer theory* (7th ed ed.). McGraw-Hill.

Selig, M. (1997). *Summary of low speed airfoil data vol. 3*. SoarTech Publications.

Serrano, A. R. (2018). Design methodology for hybrid (vtol+ fixed wing) unmanned aerial vehicles. *Aeronautics and Aerospace Open Access Journal*, *2*(3), 165–176. doi: 10.15406/aaoaj.2018.02.00047

Siemens. (2021). *Simcenter star-ccm+.* Retrieved June 18, 2021, from `https://www.plm.automation.siemens.com/global/en/products/simcenter/STAR-CCM.html`

Silva, N. (2014). *Parametric design, aerodynamic analysis and parametric optimization of a solar uav* (Master's thesis, Instituto Superior Técnico). Retrieved from `https://fenix.tecnico.ulisboa.pt/downloadFile/395146454348/Thesis.pdf`

Silva, P. (2021). *Projeto detalhado do sistema propulsivo para um veículo aéreo não tripulado com uma*

célula de combustível de hidrogénio (Unpublished master's thesis). Academia da Força Aérea.

Sinha, P. (2013, 12). Multivariate polynomial regression in data mining: Methodology, problems and solutions. *International Journal of Scientific and Engineering Research*, *4*.

Spalart, P., & Allmaras, S. (1992). A one-equation turbulence model for aerodynamic flows. *AIAA*, *439*. doi: 10.2514/6.1992-439

Stettmaier, H. (1999, November). *V-tails for aeromodels.*

Swafford, T. (1983). Analytical approximation of two-dimensional separated turbulent boundary-layer velocity profiles. *AIAA Journal*, *21*, 923-926. doi: 10.2514/3.8177

Sá, P. (2021). *Projeto detalhado estrutural de veículo aéreo não tripulado com uma célula de combustível de hidrogénio* (Unpublished master's thesis). Academia da Força Aérea.

T-Motor. (2021). *T-motor website.* Retrieved June 11, 2021, from `https://store-en.tmotor.com/`

UAV Factory. (2021). *Penguin B UAV.* Retrieved April 30, 2021, from `https://uavfactory.com/en/penguin-b-uav`

UAVision. (2020). *OGS42VN aircraft flight manual.* (Unpublished confidential document)

UAVision. (2021). *Ogassa ogs42v.* Retrieved May 04, 2021, from `https://www.uavision.com/ogassa-ogs42v`

UIUC Department of Aerospace Engineering. (2020). *UIUC Airfoil Coordinates Database.* Retrieved April 14, 2021, from `https://m-selig.ae.illinois.edu/ads/coord_database.html`

United Nations Climate Change. (2018). *Contribution of the global aviation sector to achieving paris agreement climate objectives.* Retrieved October 03, 2021, from `https://unfccc.int/sites/default/files/resource/156_CAN%20ICSA%20Aviation%20TD%20submission.pdf`

U.S. Department of Energy. (2021). *Alternative fuels data center - hydrogen basics.* Retrieved November 04, 2021, from `https://afdc.energy.gov/fuels/hydrogen_basics.html`

US Naval Research Laboratory. (2018, April). The hybrid tiger: A long endurance solar/fuel cell/soaring unmanned aerial vehicle. In *Doe annual merit review, inter-agency session.*

UTC Aerospace Technology. (2015, March). *Cloud cap technology TASE150 - datasheet.*

Versteeg, H. K., & Malalasekera, W. (1995). *An introduction to computational fluid dynamics - the finite volume method.* Addison-Wesley-Longman.

Veríssimo, R. (2016). *Best practice guidelines in cfd external aerodynamics: Applied to unmanned aerial vehicles at cruise conditions* (Unpublished master's thesis). Academia da Força Aérea.

Walters, D. K., & Cokljat, D. (2008, 10). A Three-Equation Eddy-Viscosity Model for Reynolds-Averaged Navier–Stokes Simulations of Transitional Flow. *Journal of Fluids Engineering*, *130*(12). doi: 10.1115/1.2979230

Wang, A., & Chan, T. (2017, 11). Estimation of drag for a quadplane hybrid unmanned aerial vehicle. In *2017 aiaa student conference region vii-au.*

Wilcox, D. (2006). *Turbulence modeling for cfd*. DCW Industries.

Wu, M., Han, Z., Nie, H., Song, W., Clainche, S. L., & Ferrer, E. (2019). A transition prediction method for flow over airfoils based on high-order dynamic mode decomposition. *Chinese Journal of Aeronautics*, *32*(11), 2408-2421. doi: 10.1016/j.cja.2019.03.020

Appendix A

Drag from Wind Tunnel testing of the VTOL Propulsion System

The balance software outputs the mean value of the forces and moments and the standard deviation from a set of values obtained during the the test session. Table A.1 displays the mean force in the freestream direction produced by the VTOL system which was obtained by subtracting the values from the control test with only the boom and the balance, to the ones with the full assembly, and Table A.2 contains the standard deviation calculated by square rooting the sum of the squares of the standard deviations from the control and each test case.

Table A.1: Drag mean values

Mean Value (N)		Rear Rotor Angle (rad)			
		$-\pi/4$	0	$\pi/4$	$\pi/2$
Front	$-\pi/4$	2.56	2.89	2.49	2.12
Rotor	0	2.91	3.21	2.82	2.44
Angle	$\pi/4$	2.84	3.18	2.76	2.39
(rad)	$\pi/2$	1.81	2.14	1.72	1.4

Table A.2: Standard deviation values

Standard Deviation (N)		Rear Rotor Angle (rad)			
		$-\pi/4$	0	$\pi/4$	$\pi/2$
Front	$-\pi/4$	0.142	0.127	0.135	0.142
Rotor	0	0.120	0.150	0.120	0.127
Angle	$\pi/4$	0.135	0.142	0.135	0.127
(rad)	$\pi/2$	0.158	0.150	0.120	0.135

The force values in the vertical direction (positive values indicate generation of lift) are displayed in Table A.3 and A.4 From the combinations tested, the one which presented the lowest value was the one with both rotors at $\pi/2\ rad$. Since the weight of the tested components remained the same throughout the experiment, higher values than this case can only mean that there was a higher lift generation. As a result, this case was assumed to be the reference by having zero lift while all the remaining cases had a positive lift generation.

Table A.3: Lift mean values

Mean Value (N)		Rear Rotor Angle (rad)			
		$-\pi/4$	0	$\pi/4$	$\pi/2$
Front	$-\pi/4$	1.97	2.06	0.98	0.85
Rotor	0	2.07	2.00	0.86	0.92
Angle	$\pi/4$	2.88	3.3	1.87	1.85
(rad)	$\pi/2$	1.19	1.31	0.17	0.00

Table A.4: Lift standard deviation values

Standard Deviation (N)		Rear Rotor Angle (rad)			
		$-\pi/4$	0	$\pi/4$	$\pi/2$
Front	$-\pi/4$	0.184	0.198	0.166	0.161
Rotor	0	0.161	0.191	0.166	0.172
Angle	$\pi/4$	0.184	0.178	0.166	0.166
(rad)	$\pi/2$	0.184	0.191	0.166	0.184

Whenever the data does not present a simple linear regression, a polynomial regression can be applied for single variable or multi variable cases (Sinha, 2013). For the problem in question, the stopping position of the front rotor is independent from the rear one, and each one has a different impact on the total drag produced. A second order multiple polynomial regression can be expressed as:

$$y = \beta_0 + \beta_1 x_1 + \beta_2 x_2 + \beta_{11} x_1^2 + \beta_{22} x_2^2 + \beta_{12} x_1 x_2 + \epsilon \tag{A.1}$$

,with β_1, β_2 the linear effect parameters, β_{11}, β_{22} the quadratic effect parameters, β_{12} the interaction effect parameters and ϵ the error component relative to the higher order terms (Sinha, 2013).

With both independent variables being angles and producing results with a period of π as the rotors have two blades, it comes to mind using a trigonometric function to express the drag as a function of both rotor angles. A single variable polynomial-trigonometric regression is given by:

$$y = b_0 + \sum_{j=1}^{d} b_j x^j + \sum_{j=1}^{\lambda} [c_j cos(jx) + s_j sin(jx)] \tag{A.2}$$

, where the b_j, c_j and s_j are obtained by regression on the y data (Eubank & Speckman, 1990). Since the period of the function is known, this regression can be slightly altered and updated to give better estimates by introducing an horizontal offset to the trigonometric terms.

Due to the low number of data gathered, a second or higher order regression produces unrealistic results as the drag predictions for untested cases are not physically reliable: for instance, it is expected the drag to always increase while going from 0 to $\pi/2\ rad$, however a second order trigonometric function completely adapts to all points considered, with all data being a local minimum/maximums, which is unrealistic for drag when $\phi = \pm\pi/4\ rad$. As a result a first order multi-variable polynomial-trigonometric function is employed.

With all the considerations done, the final general expression for the curve-fitting expression to be applied is in the form:

$$z = a + b_1 2\phi_1 + b_2 2\phi_2 + c_1 cos(2\phi_1 + f_1) + d_1 sin(2\phi_1 + g_1) + c_2 cos(2\phi_2 + f_2) + d_2 sin(2\phi_2 + g_2) \tag{A.3}$$

, with all the constant to be computed based on the z data. To get the regression for the drag values, the MATLAB curve-fitting toolbox was used and the coefficients were obtained (Mathworks, 2004). The terms b_1 and b_2 were in the order of 10^{-7} which is negligible when compared to the remaining constants, therefore, they were removed from the curve-fitting expression without compromising the final result since the R^2 remained the same. The final expression is then retrieved and expressed in Equation (6.4).